Three-Dimensional Nonlinear Dynamic Time History Analysis of Seismic Site and Structure Response

Mitrović, Saša

UNIVERSITY OF RIJEKA
FACULTY OF CIVIL ENGINEERING

Saša Mitrović

THREE-DIMENSIONAL NONLINEAR DYNAMIC TIME HISTORY ANALYSIS OF SEISMIC SITE AND STRUCTURE RESPONSE

DOCTORAL THESIS

Rijeka, 2015.

UNIVERSITY OF RIJEKA
FACULTY OF CIVIL ENGINEERING

Saša Mitrović

THREE-DIMENSIONAL NONLINEAR DYNAMIC TIME HISTORY ANALYSIS OF SEISMIC SITE AND STRUCTURE RESPONSE

DOCTORAL THESIS

Supervisor: prof. dr. sc. Joško Ožbolt
Co-supervisor: doc. dr. sc. Vanja Travaš

Rijeka, 2015.

Mentor: prof. dr. sc. Joško Ožbolt
Komentor: doc. dr. sc. Vanja Travaš

Doktorski rad obranjen je 23. lipnja 2015. na Građevinskom fakultetu u Rijeci pred povjerenstvom u sastavu:

1. prof. dr. sc. Mehmed Čaušević, Sveučilište u Rijeci, Građevinski fakultet, predsjednik povjerenstva

2. prof. dr. sc. Joško Ožbolt, Sveučilište u Rijeci, Građevinski fakultet, član

3. prof. dr. sc. Damir Lazarević, Sveučilište u Zagrebu, Građevinski fakultet, član

Abstract

In the present thesis a three-dimensional finite element model for non-linear dynamic analysis of (1) seismic site and structure response and (2) soil-structure interaction with contact discontinuity is proposed and discussed. Accordingly, two numerical studies are presented, each consisting of a series of analyses of a coupled structure - foundation - soil system.

In the first study a series of numerical examples are presented which include modelling of a reinforced concrete frame with a portion of the ground consisting of various horizontal layers resting on rigid bedrock. The influence of the ground layer configurations on the structure response due to seismic loads is investigated and discussed.

In the second study the influence of various parameters governing the structure response, with emphasis on sliding and rocking of the structure, are investigated by assuming discontinuity in the soil - foundation interface.

The spatial discretisation is performed by a combination of linear tetrahedral (ground) and hexahedral (structure) finite elements. The time integration is carried out by explicit integration using the leap-frog method. Total Lagrange formulation is adopted to account for large rotations and large displacements (geometrical non-linearity). To account for cracking and damage of the concrete, the frame structure is modelled by the microplane model (material non-linearity). Damage and cracking phenomena are modelled within the concept of smeared cracks. Plasticity model is used for the modelling the reinforcement and the ground adopting the Von Mises and Drucker–Prager yield criteria, respectively. The usual continuum assumption when treating the soil–foundation interface is replaced with a contact discontinuity approach in order to be able to capture foundation sliding and/or uplifting and rocking (contact non-linearity). Coulomb frictional model is adopted in the contact resolution.

The proposed finite element code demonstrate the possibilities of advanced numerical approaches in simulation of complex engineering problems. Comparative analysis shows the importance of the local site conditions and influence of material non-linearity in seismic structural design. With the implemented microplane model, which is aimed to be used for fracture and damage analysis of concrete, it is possible do assess the sustained structural damage. Furthermore, for extreme scenarios with highly geometrically non-linear behaviour, as sliding and rocking, the proposed model of foundation - soil interface is more adequate than usual continuum approach with spring - dashpot elements and at the same time maintains a reasonable computational efficiency.

Keywords: finite elements; microplane model; contact mechanics; time history analysis; soil-structure interaction; site-effects; seismic performance assessment

Sažetak

U ovoj dizertaciji predložen je i analiziran numerički prostorni model s konačnim elementima za nelinearnu dinamičku analizu (1) odziva lokalnog tla i konstrukcije i (2) interakciju tla i konstrukcije s kontaktnim diskontinuitetom. Sukladno tome, predstavljene su dvije numeričke studije od kojih se svaka sastoji od niza proračuna sklopa konstrukcija - temelj - tlo.

U sklopu prve studije prikazan je niz numeričkih primjera koji uključuju modeliranje armirano betonskog okvira s temeljnim tlom koje se sastoji od različitih horizontalnih slojeva položenih na krutu osnovnu stijenu. Istražen je utjecaj konfiguracije slojeva tla na odziv konstrukcije uslijed potresnog djelovanja.

U sklopu druge studije istražen je utjecaj raznih parametara na odziv konstrukcije, poglavito na klizanje i *rocking*, pretpostavljajući diskontinuitet na kontaktu tla i temelja.

Prostorna diskretizacija izvršena je tetraedarskim (tlo) i heksaedarskim konačnim elementima (konstrukcija). Integracija jednadžbe gibanja provedena je eksplicitno metodom *leap-frog*. *Total Lagrange* formulacija je primijenjena kako bi se uzeli u obzir veliki pomaci i rotacije (geometrijska nelinearnost). Pukotine i oštećenja u betonu konstrukcije modelirane su mikroravninskim modelom unutar koncepta razmazanih pukotina (materijalna nelinearnost). Teorija plastičnosti primijenjena je za modeliranje armature i temeljnog tla koristeći Von Mises i Drucker-Prager kriterij tečenja. Uobičajeni pristup modeliranja kao kontinuuma zamijenjen je kontaktnim diskontinuumom kako bi se moglo opisati klizanje temelja i/ili odizanje i *rocking* (kontaktna nelinearnost). Pri rezoluciji kontakta korišten je Coulomb-ov model trenja.

Predloženi računalni kod s konačnim elementima pokazuje mogućnosti naprednih numeričkih pristupa u simulaciji složenih inženjerskih problema. Komparativna analiza pokazuje važnost lokalnih uvjeta tla i materijalne nelinearnosti u proračunu konstrukcija na potresna djelovanja. S implementiranim mikroravnimskim modelom, koji je razvijen s ciljem opisivanja pojava pukotina i oštećenja u betonu, moguće je ocijeniti posljedična strukturna oštećenja. Povrh toga, kad je važna geometrijska nelinearnost, kao što je u slučaju pojave klizanja i *rocking*-a, predloženi model veze sklopa temelj - tlo primjereniji je od klasičnog modela s oprugama.

Ključne riječi: konačni elementi; mikroravninski model; mehanika kontakta; analiza odziva zapisima u vremenu; interakcija tla i konstrukcije; utjecaj lokalnih uvjeta; procjena seizmičkih performansi

Acknowledgements

I would like to express my sincere gratitude to my supervisor, Prof. Joško Ožbolt, for his guidance, expertise, and patience throughout my research. Very special thanks to Prof. Mehmed Čaušević for his invaluable guidance and remarkable support throughout my graduate and postgraduate studies. I would also like to thank Prof. Damir Lazarević for our pleasant conversations on the research topics and for willing to participate in my final defence committee. Special thanks to my co-supervisor Vanja Travaš for the support, for his patience in answering endless number of questions, but foremost for being a good friend.

I want to thank my colleagues at i.t.t d.o.o. and stabilnost d.o.o. for the given encouragement, motivation and support.

Finally, and above all, I would like to thank my parents, my wife and daughter for their utmost support.

Contents

List of Figures

List of Tables

Abbreviations

B.S.	**B**ase **S**hear
CLF	**C**ourant, **F**riedrichs and **L**ewy
CSM	**C**apacity **S**pectrum **M**ethod
FE	**F**inite **E**lements
FEM	**F**inite **E**elements **M**ethod
FEMA	**F**ederal **E**mergency **M**anagment **A**gency
GL	**G**reen **L**agrange strain tensor
GSI	**G**eological **S**trength **I**ndex
NSP	**N**on-linear **S**tatic **M**ethod
PGA	**P**eak **G**round **A**cceleration
PGD	**P**eak **G**round **D**isplacement
PGV	**P**eak **G**round **V**elocity
PK	**P**iola **K**irchhoff
PK2	second **P**iola **K**irchhoff stress tensor
RC	**R**einforced **C**oncrete
SDOF	**S**ingle **D**egree **O**f **F**reedom
SSI	**S**oil **S**tructure **I**nteraction
TL	**T**otal **L**agrange

Symbols

In the present Thesis the direct, matrix and full notations are preferred, whereas the indicial notation is used only when the expressions are too complicated in other notations or their representation is not feasible. As an example consider the dot product between vectors $\mathbf{a} = (a_1, a_2, a_3)$ and $\mathbf{b} = (b_1, b_2, b_3)$ written in four different notations:

$$\underbrace{a_i\, b_i}_{\text{indicial}} = \underbrace{\mathbf{a}.\,\mathbf{b}}_{\text{direct}} = \underbrace{\mathbf{a}^{\mathrm{T}}\mathbf{b}}_{\text{matrix}} = \underbrace{a_1 b_1 + a_2 b_2 + a_3 b_3}_{\text{full}}.$$

The following conventions are employed in the used notation regarding subscripts, superscripts and indices. The left superscript indicates in which configuration the quantity (body force, stress, strain, etc.) occurs while the left subscript indicates the configuration with respect to which the quantity is measured. For example the body force components at time $t + \Delta t$, measured in configuration 0, is: ${}^{t+\Delta t}_{0}f_i$, $i = 1, 2, 3$. In this case the right subscript denotes the individual component of the vector. A comma in the right subscript, on the other hand, denotes differentiation with respect to the coordinate following, for example:

$${}^{t+\Delta t}_{0}u_{i,j} = \frac{\partial\, {}^{t+\Delta t}u_i}{\partial\, {}^{0}x_j}.$$

The most frequent symbols are listed below.

Chapter 1

$\dot{u}$	particle velocity
v_s	shear wave velocity
ρ	material density

Chapter 2

$\mathbf{b}$	body (volume) forces
$\mathbf{B}$	strain-displacement matrix
$\mathbf{C}$	damping matrix

$\mathbf{D}$	stress-strain matrix
E	Young's modulus
$\mathbf{F}^{\text{int}}$	internal forces
$\mathbf{K}$	stiffness matrix
$\mathbf{J}$	Jacobian matrix
L_e	characteristic element length
$\mathbf{M}$	mass matrix
$\hat{\mathbf{M}}$	effective mass matrix
$\mathbf{N}$	shape functions matrix
$\mathbf{R}$	vector of externally applied forces
$\hat{\mathbf{R}}$	effective load vector
$\mathbf{t}$	traction forces
u_i	displacement component
$\mathbf{u}$	displacement vector
$\dot{\mathbf{u}}$	velocity vector
$\ddot{\mathbf{u}}$	acceleration vector
t	time
$\mathbf{v}$	velocity
V	volume
α	mass coefficient
β	stiffness coefficient
Δt	time interval
η_i	local coordinate
μ_i	local coordinate
ν	Poisson's ratio
ξ_i	local coordinate
ρ	material density
ω_{max}	largest element frequency
Ω	element domain

Chapter 3

${}^t_0\mathbf{B}_L$	linear strain-displacement matrix
$\mathbf{C}$	right Cauchy-Green deformation tensor
$\mathbf{e}_1, \mathbf{e}_2, \mathbf{e}_3$	material frame unit vectors
$\mathbf{E}_1, \mathbf{E}_2, \mathbf{E}_3$	spatial frame unit vectors
$\mathbf{F}$	deformation gradient
$\mathbf{G}$	displacement gradient
$h_{i,j}$	shape function derivatives
$\mathbf{I}$	identity matrix
J	Jacobian of deformation
$\mathbf{J}$	Jacobian matrix

l_{ij}	displacement gradient components
$\mathbf{P}$	first Piola-Kirchhoff stress tensor
$\mathbf{R}$	Rotation tensor
$\mathbf{S}$	Cauchy stress
${}^{t}_{0}\hat{\mathbf{S}}$	vector form of PK2
S_{ij}	second Piola-Kirchhoff stress tensor
$\mathbf{u}$	displacement vector
$\mathbf{U}$	displacement vector in the Eulerian description
$\mathbf{v}$	left stretch tensor
$\mathbf{U}$	right stretch tensor
V	volume
x_1, x_2, x_3	material frame axes
X_1, X_2, X_3	spatial frame axes
ε_{ij}	Green-Lagrange strain tensor
ρ	material density
$\hat{\sigma}$	back-rotated Cauchy stress

Chapter 4

$\mathbf{a}$	normal to the yield surface
$\mathbf{b}$	normal to the plastic potential surface
c	cohesion
$C_{D,0}$	microplane secant deviatoric modulus
$C_{M,0}, C_{K,0}$	microplane secant shear moduli
$C_{V,0}$	microplane secant volumetric modulus
$\mathbf{D}_e$	elastic stress-strain matrix
$\mathbf{D}_{ep}$	elasto-plastic stress-strain matrix
e_D	deviatoric part of the microplane normal strain component
e_K, e_M	shear strain microplane components
e_N	normal strain microplane component
e_V	volumetric part of the microplane normal strain component
$E_{D,0}$	initial (undamaged) microplane deviatoric modulus
$E_{M,0}, E_{K,0}$	initial (undamaged) microplane shear moduli
$E_{V,0}$	initial (undamaged) microplane volumetric modulus
f	yield criterion
f_{vm}	vom Mises yield criterion
f_{dp}	Drucker-Prager yield criterion
g	plastic potential
I_1	first stress invariant
J_2	second deviatoric stress invariant
k	material parameter
$\mathbf{k}$	unit normal vector

K_{ij}	projection tensor
$\mathbf{m}$	unit normal vector
M_{ij}	projection tensor
$\mathbf{n}$	unit normal vector
N_{ij}	projection tensor
R	radius
s_D	deviatoric microplane stress component
s_K, s_M	shear microplane stress component
s_N	normal microplane stress component
s_V	volumetric microplane stress component
α	material parameter
$\Delta\boldsymbol{\varepsilon}$	strain increment
$\Delta\boldsymbol{\sigma}_e$	elastic stress increment
$\dot{\boldsymbol{\varepsilon}}_p$	plastic strain rate
$\dot{\boldsymbol{\varepsilon}}_t$	total strain rate
$\dot{\boldsymbol{\lambda}}$	plastic strain-rate multiplier
σ	normal stress
$\dot{\boldsymbol{\sigma}}$	stress change
$\boldsymbol{\sigma}_0$	initial stress
$\boldsymbol{\sigma}_c$	uni-axial compression
$\boldsymbol{\sigma}_e$	trial elastic stress
$\boldsymbol{\sigma}_t$	uni-axial tension
τ	shear stress
ϕ	friction angle
ψ	discontinuity function
$\omega_{D,0}$	material integrity parameter related to the microplane deviatoric strain
$\omega_{M,0}, \omega_{K,0}$	material integrity parameter related to the microplane shear strain
$\omega_{V,0}$	material integrity parameter related to the microplane volumetric strain

Chapter 5

$\overline{\mathbf{a}_\alpha}, \overline{\mathbf{a}_\beta}$	target surface tangent vectors
$\mathbf{g}$	gap vector
$\mathbf{G}$	contact displacement constrain matrix
$\mathbf{n}$	normal unit vector
$\mathbf{t}_1, \mathbf{t}_2$	in-plane unit vectors
t_C	time of collision
$\mathbf{t}$	traction vector
$\mathbf{u}^C$	contact displacement vector
$\mathbf{u}^D$	displacement predictor vector
$\mathbf{v}$	velocity vector

$\boldsymbol{\lambda}$	Lagrange multiplier vector
λ_N	normal component of the contact force
λ_T	tangential component of the contact force
μ	friction coefficient
w_{cr}	critical crack opening
ξ_1, ξ_2	contractor node and target surface intersection coordinates

Chapter 7

$C_{m,i}$, $C_{t,i}$	lumped dashpot factors
d_{rel}	relative displacement
d_{tot}	total displacement
E_c	Young's modulus for concrete
E_{rm}	rock mass deformation modulus
E_s	Young's modulus for steel reinforcement
f_c	uni-axial compressive strength
f_t	uni-axial tensile strength
f_{yd}	steel yield strength
G_F	fracture energy
h_e	average element size
v_{NORMAL}, v_n	normal wave propagation velocity
v_{rel}	relative velocity
v_{SHEAR}, v_s	shear wave propagation velocity
$v_{s,30}$	average value of propagation velocity of S waves in the upper 30 m
ε_{cr}	critical strain
μ	friction coefficient
ρ_c	mass density of concrete
ρ_s	mass density of steel reinforcement
σ, τ	normal and shear stress on the boundary

To my wife and daughter for their love and patience

Chapter 1.

Introduction

1.1. Motivation and problem definition

The subject of this thesis is the development of a three-dimensional finite element model for non-linear dynamic analysis of seismic site and structure response with emphasis on soil-structure interaction (SSI). Specifically, two types of problems are studied and discussed:

1. numerical modelling of a reinforced concrete frame with a large portion of the ground consisting of various horizontal layers resting on rigid bedrock on which the input motion is applied, and
2. formulation of a more detailed SSI model in which the usual continuum assumption when treating the soil-foundation interface is replaced with contact discontinuity approach in order to be able to capture foundation sliding an/or uplifting (rocking).

Ground motions observed at a specific site generally depend on the type of the earthquake fault mechanism, the way seismic waves propagate from their source to the top of the bedrock and finally from the top of the bedrock to the surface. The rupture mechanism and the propagation of seismic waves through the earth's crust are difficult to model due to their complex nature and a large amount of uncertainty involved. The problem of ground response analysis then becomes one of the determining responses of the soil deposit to the motion of the bedrock immediately beneath it (Kramer, 2014). Soil deposits act as filters to seismic waves changing the frequency content of motion by attenuating amplitudes at certain frequencies and amplifying others. Amplification factors (the ratio between a ground motion intensity measure at the surface and the bedrock level) can be very high or even very small (de-amplification effect). Since soil conditions often vary

considerably over short distances, levels of ground shaking can vary significantly within a very small area. The site response mechanism is mainly governed by the principle of conservation of elastic energy, which requires a constant energy flux ($\rho v_s \dot{u}^2$) through ground from depth to the surface. Since the density ρ and shear wave velocity v generally decrease approaching the ground surface, the particle velocity $\dot{u}$ increases. Resonance effects in the soil column can additionally contribute to site amplification. On the other hand, de-amplification effects are generally caused by soil non-linear behaviour. All of this is the focus of the first problem discussed.

Ground motions that are not influenced by the presence of structures are referred to as free-field motions. When a structure founded on solid rock is subjected to an earthquake, the very high stiffness of the rock constraints the rock motion to be very close to the free field motion. Structures founded on rock are considered to be fixed-base structures and the computation of their response is relatively simple. On the other hand, the same structure would respond differently if founded on a soft soil deposit. Firstly, the inability of the foundation to conform to the deformations of the free-field motion would cause the motion of the base of the structure to deviate from the free-field motion. Secondly, the dynamic response of the structure itself would induce deformation of the supporting soil. This process, in which the response of the soil influences the motion of the structure and the response of the structure influences the response of the soil, is referred to as soil-structure interaction and is the main focus of the second problem.

In conclusion, one of the most important aspects of earthquake engineering is the evaluation of the effect of local site conditions on strong ground motions along with adequate treatment of SSI interaction. For many structures the SSI has little effect on the dynamic response. In other cases, however, its effect can be very important. Whether the neglect of its effects is conservative or non-conservative depends on the specific problem at hand and must be evaluated on a case by case basis. Design parameters may be obtained from building codes or may be developed on a site-specific analysis. For a typical site, parameters based on site-specific analyses are likely to be more accurate than code-based parameters and they are also likely to result in more economical design. This is especially important in design of structures of common interest, such as bridges, nuclear power plants and similar kind of structures.

1.2. State of the art

The influence of local site conditions on the intensity of ground shaking and earthquake damage has been known for many years. Already in the early 19th century was noted

that during an earthquake buildings situated on rock were much less affected by earthquakes than those whose foundation were on softer soils. Nevertheless, provisions that specifically accounted for local site effects did not appear in building codes until the 1970s. A series of well documented catastrophic earthquakes in the second half of the 20th century (Caracas, Venezuela, 1967; San Fernando, California, 1971; Mexico City, 198; Loma Prieta, San Francisco Bay, 1989) incited first serious scientific researches of these phenomena. Spectral accelerations recorded during these earthquakes in a relatively small area differed by a factor 10 or more. The greatest damage were caused by resonance effects which originated as a consequence of fundamental period of the structure matching the characteristic period of the site. How large is the influence of a particular site to the surface ground motions depends on the material properties, geometry, topography and characteristic of the input motion. Structural response is a direct consequence of the effects discussed above. In general, a complete structural response analysis should model the structure and the site together with an adequate interface but often the problem is split into two separate tasks.

There are many studies concerning site response assessment. Very often this complex phenomenon is accounted for in a probabilistic way by empirical methods based on observed data from previous earthquakes. A significant source of this data can be found in the KiK-net databases (NIED, 2013; Aoi et al., 2004) which consist of numerous sets of borehole and surface response records. The borehole data can be effectively used for prescribing in-depth (bedrock) motions generating the free-field (outcrop) motion as a result of specific site conditions. Many studies were conducted relaying on these (Héloïse et al., 2012; Montalva, 2010; Singupalli, 2008) and similar data (Semblat et al., 2000).

On the other hand, non-linear numerical approach of site response is always challenging and inevitably involves large models with considerable computational effort (Kontoe et al., 2008; Lopez-Caballero et al., 2007; Pergalani et al., 2006; Smerzini et al., 2011; Hashash and Park, 2002). Consequently, the problem is often reduced to two or even one dimension like in Hashash and Park (2001); Phillips and Hashash (2009); Park and Hashash (2004).

Numerical analysis of structural response alone, on the other hand, was widely studied and several procedures for non-linear static static analysis of structures have been implemented into the latest European and US seismic provisions. The N2 method (Fajfar, 2000; Kreslin and Fajfar, 2012) was implemented in European regulations (Eurocode 8, 2011) and the Capacity Spectrum Method (CSM) and the coefficient method, that is Non-linear Static Procedure (NSP), where introduced in US provisions (FEMA-273, 1997; FEMA-356, 2000; FEMA-440, 2005). A detailed discussion of this procedures can be found in Fajfar and Gašperšič (1996), Rozman and Fajfar (2009), Mitrović and

Čaušević (2009) and Caušević and Mitrović (2011). Although more easy and straight forward to implement, these procedures lack the rigorosity and versatility of the pure dynamical time-history analysis, which with the constant rise of computational power, becomes more and more approachable. Moreover, many studies (Gazetas and Mylonakis, 1998; Jeremić et al., 2009) indicate that use of free field motions as input for structural only models might not be appropriate which inevitable leads to the conclusion that the founding soil should be taken into account in a thorough seismic analysis of a structure.

Nevertheless, coupled analyses are rare because they require models large in size and complexity (needing great computational power) and consequently are usually conducted with various simplifications. An overview of the current approaches can be found in (Dolšek et al., 2009). Ideally, a complete soil structure analysis (SSI) should involve detailed coupled modelling of the structure, its foundation and the surrounding soil domain as a whole. In the simplest models the soil is represented by distributed tensionless linear spring-dashpot elements (Yim and Chopra, 1984; Houlsby et al., 2005) or by elastoplastic Winkler models (Harden et al., 2005, 2006; Gerolymos and Gazetas, 2006; Harden and Hutchinson, 2009). In more advanced models the soil is modelled as an elastic or inelastic continuum (Gazetas et al., 2007; Jahromi, 2009; Sextos and Taskari, 2009; Jeremić et al., 2009; Jeremić and Yang, 2002) with relatively simple structure models. Regardless of the modelling of the SSI, a full dynamic time history analysis is usually replaced by computationally more efficient quasi-dynamic approach like the pushover analysis (Sextos and Taskari, 2009; Panagiotidou et al., 2012). Uplifting of the structure's foundation with consequential rocking was studied in various forms using one of the mentioned approaches (Apostolou et al., 2007; Gajan and Kutter, 2009; Panagiotidou et al., 2012). Different base-isolations system were also studied in a similar way (Lu and Hsu, 2013; Mahmoud et al., 2012).

All studies agree on the importance of SSI for structure response analysis and acknowledge the need for even more detailed approaches. Since computer power is rapidly becoming more available and affordable, use of advanced models in assessing seismic performance of structures becomes more attractive. A viable path for a more advanced representation of the SSI problem is modelling both the structure and the supporting soil as an inelastic continuum and treating the interface as a strong discontinuity (contact non-linearity).

1.3. Aim an objectives of the thesis

The aim of this thesis is to investigate the objectivity of the current principles used in the design of structures for earthquake resistance and formulations of guidelines for their

improvement with the purpose of constructing more reliable and economic structures. It is also an intention to demonstrate the possibility of advanced numerical approaches in simulation of complex engineering problems such as soil-structure interaction in case of earthquake loading.

The primary objective of this thesis is the development and application of an original computer program for three-dimensional non-linear dynamic analysis of site and structure response with emphasis on SSI. The programme code was developed in Fortran program language with PGI Visual Fortran (PGI, 2010). Femap (Siemens, 2009) was used as a pre-processing tool and Para View (Kitware, 2012) as a post-processing tool. The research is based on two numerical studies which include analyses of site and structure response and a detailed representation of the soil-structure interaction, all with the aim to accomplish the following intentions:

- reveal the impact of different soil layer configurations on frequency content and amplitudes variations along a soil column from bedrock to the surface,
- compute site-specific spectra based on non-linear analysis and reveal the transformation of earthquake energy into other mechanical energies,
- assess the structural performance and perform damage analysis of a reinforced concrete on a specific site,
- investigate foundation sliding and rocking using the contact discontinuity approach,
- improve the existing numerical algorithms and define further directions of development of numerical models of soil structure interaction and site and structure response.

First numerical study

This study consists of a series of numerical analyses which include modelling of a reinforced concrete frame with a large portion of the ground consisting of various horizontal layers resting on rigid bedrock. The developed model does not need to assume the surface ground motion. Instead, the surface ground motion is a result of the motion of the bedrock influenced by the different ground layers above the bedrock and the structure itself. The three-dimensional analysis is necessary when soil conditions vary spatially, the input motion is not unidirectional and the response of a three-dimensional structure is of interest. It is assumed that the response of a site is predominantly caused by horizontal shear waves propagating vertically from the underlying bedrock. The bedrock is assumed to be rigid acting as a fixed end boundary. The input motion is applied at the bottom of the model (bedrock acting as a hypocentre) and the considered structure

is located directly above (in the epicentre). As opposed to many substructure methods (Jeremić et al., 2009; Lehmann, 2005; Spiliopoulos and Lykidis, 2006), this model is based on the direct method in which the upper structure, foundations and the bounded soil zone (so called near field) are modelled by the finite element method (FEM) using solid elements. To account for cracking and damage of the concrete, the frame structure is modelled by the microplane model. Damage and cracking phenomena are modelled within the concept of smeared cracks. Plasticity model is used for the modelling the reinforcement and the ground adopting the Von Mises and Drucker–Prager yield criteria, respectively. Non-linear soil behaviour becomes important for ground motions of higher intensity and, generally, it can be expected that non-linear modelling would decrease the demand on structure. The effect of the surrounding unbounded soil (so-called far-field) is approximated by imposing Lysmer and Kuhlemeyer transmitting boundary conditions along the near-field/far-field interface. The investigated examples encompass geometry and phenomena in the range of several orders of magnitude: starting from the ground (hundreds of meters), RC structure (m), steel reinforcement (cm) and, finally, cracking of concrete (mm). Therefore, considering the inevitable large-size models and all the incorporated non-linearities, a problem of computational efficiency merges naturally. Finally, the main objective of the study is to investigate the influence of the ground layer configurations on the site and structure response with appropriate damage analysis of the RC structure. Part of this study can be found in Mitrović et al. (2014).

Second numerical study

Typical seismic loads on structures with shallow foundation will usually induce significant non-linear actions in the soil-structure interface. These non-linearities are geometrical and material in nature. Geometrical non-linearities include sliding at the soil-foundation interface and foundation uplifting from the supporting soil whereas material non-linearity includes formation of bearing capacity failure surfaces, i.e. failure of soil. The structure response can be heavily influenced by these three non-linearities. Therefore, a detailed soil-structure interaction (SSI) model should explicitly account for the occurrence of one or more mentioned non-linearities. In this sense a three-dimensional finite element model for dynamic SSI analysis with contact discontinuity is proposed and discussed. This model is based on the direct method in which the upper structure, foundations and the bounded soil zone (so called near field) are modelled by the finite element method (FEM) using three-dimensional (3D) solid finite elements. The usual continuum assumption when treating the soil–foundation interface is replaced with a contact discontinuity approach in order to be able to capture foundation sliding and/or uplifting (rocking). Since the focus of this study is the SSI itself, rather that the influence of the site characteristics on the changes of the ground motion, only a small portion of the ground was modelled and the acceleration time history was applied on all nodes of the substructure

in the horizontal direction leaving the vertical component free. To examine the influence of a contact discontinuity between the soil and the structure a series of numerical analysis were performed by varying the ground motion intensity (by setting the PGA of the selected accelerogram) and for different coefficients of friction μ. To emphasis the contact discontinuity in the presented numerical examples the structure is founded on a flat ground surface. Namely, in this case almost all of the seismic energy will be transferred through the contact discontinuity by friction forces. A minor part of the energy will be transferred by normal forces, i.e. by ground elevation. The emphasis is on the physics of the soil – foundation system in the perspective of two important interconnected non-linear mechanisms: (1) foundation sliding and/or detachment from the soil with subsequent uplifting and (2) formation and accumulation of plastic deformations in the ground below the footing. The interaction of these mechanisms can eventually lead to collapse by dynamic instability (overturning) or collapse by soil failure. The objectives are: to provide insight in the influence of various parameters governing sliding and rocking of the structure and to give a visible and more realistic alternative to the classic representations of the SSI founded such as Winkler and continuum models.

The results of this research are a contribution in development of more economic structures with increased reliability for earthquake loadings and are a logical extension of published works in this important field of engineering.

1.4. Thesis outline

The thesis consists of eight individual chapters which are summarized as follows.

Chapter 1. Introduction
In this chapter the studied problems are introduced and the state of the art is overviewed. Next the aims and objectives are presented and finally the two numerical studies, which make the central part of the thesis, are described.

Chapter 2. Numerical framework
Finite element method was used to perform the discretisation of the governing differential equations in space and the finite difference method was used for the discretisation of time. The first part of the second chapter is dedicated to the spatial discretisation which is performed by three-dimensional solid elements: the linear tetrahedron and the tri-linear hexahedron. The second part of the chapter is dedicated to the two finite difference procedures used for time discterisation: the central difference method and the leap-frog method.

Chapter 3. Geometrical non-linearity

The discussed problems are defined in the framework of continuum mechanics. Furthermore, the very nature of the studied problems, especially the second one, requires a geometrically non-linear description. For this reason a brief overview of continuum mechanics and finite strain theory is given followed by an description of the total Lagrange formulation which allows modelling of large rotations and displacements.

Chapter 4. Material non-linearity

A fully non-linear analysis, as is suggested by the title of the Thesis, has to include non-linear descriptions of the materials. In the first numerical study the structure (reinforced concrete frame) and the ground (rock masses) are analysed with appropriated constitutive models: microplane for the concrete and plasticity for the reinforcement and the ground. In the second numerical study, where the emphasis is on the SSI, the ground is modelled the same way but the structure is treated as linear elastic. Accordingly, this chapter gives a theoretical overview of these models along with different computational aspects and the numerical implementation.

Chapter 5. Contact non-linearity

The second numerical study is focused on the SSI assuming a discontinuity in the soil-foundation interface which is based on the principles of contact mechanics. The first part of the chapter is dedicated to the global and local detection strategies and forming of contact elements. The second part is dedicated to the contact resolution which is based on forward incremental Lagrangian multipliers method and executed by Gauss-Seidel iteration strategy. Additionally, the adopted Coulomb frictional model is presented and discussed.

Chapter 6. Computer program structure and computational aspects

The primary objective of this thesis was the development of an original computer program code for three-dimensional non-linear dynamic analysis of site and structure response with emphasis on SSI. The program code was developed in Fortran language and this chapter presents its algorithmic structure. The implementation of all important concepts and procedures introduced in the previous four chapters is explained. Finally, different computational aspects, such as memory and time requirements are discussed.

Chapter 7. Numerical studies

This chapter presents in detail two numerical studies preformed by the dedicated program introduced in the previous chapter. The studies are the central part of the Thesis and include analyses of site and structure response with a detailed representation of the soil-structure interaction. Based on the parameter analyses performed a series of conclusions are drawn.

Chapter 8. Summary and conclusions

The last chapter includes a summary of the entire Thesis followed by conclusions and directions for future work. Conclusions are given separately for both numerical studies along with an overall critical appraisal.

Chapter 2.

Numerical framework

The presented numerical analyses are based on principles of continuum and contact mechanics and irreversible thermodynamics. The real physical domain of the studied problems with an infinite number of degrees of freedom is discretisied with an approximated domain with a finite number degrees of freedom. This discretisation is performed according to the *finite element method*. The adopted finite elements, the linear tetrahedron and the trilinear hexahedron, are introduced in Section 2.1. The time period in which the studied events occur, also has to be discretisied. The continuous time line is replaced by a set of points (finite number of time increments). At these discrete points the governing equations have to be satisfied. The time integration of the dynamic equilibrium equation is performed with the *finite difference method* which is introduced in Section 2.2.

2.1. Spatial discretisation

Spatial discretisation involves the subdivision of the physical domain Ω bounded by Γ into a finite number of sub-domains Ω_e, i.e. finite elements (Figure 2.1.). This discretisation is performed by linear tetrahedral and trilinear hexahedral elements (Zienkiewicz and Taylor, 2005, 2000; Belytschko et al., 2013; Bathe, 1996).

2.1.1. Linear tetrahedral elements

The linear tetrahedron element consists of four nodes, six corners and four faces. Figure 2.2.(a) shows a typical four-node tetrahedron. Its geometry is fully defined by giving the location of the four corner nodes with the respect to the local reference coordinate

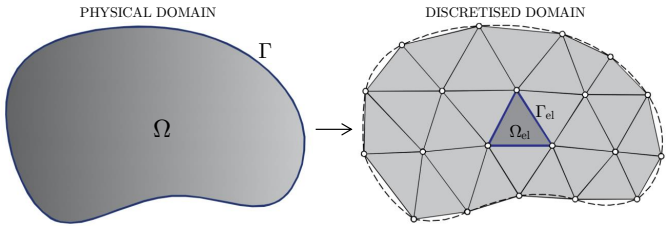

Figure 2.1.: Approximation of a real physical domain by finite number of sub-domains (finite elements).

system $(x,\ y,\ z)$:

$$x_i,\ y_i,\ z_i \quad (i = 1, 2, 3, 4). \tag{2.1.}$$

The numbering convention is given in Figure 2.2.(b) which assures that the volume will

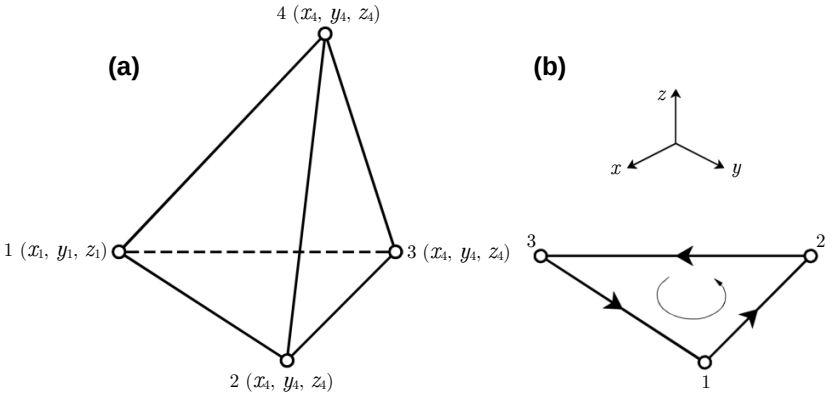

Figure 2.2.: (a) The linear tetrahedron element (4-node tetrahedron) and (b) node numbering convention - face 1-2-3 as seen from node 4.

be a positive when calculated in the following way:

$$V = \frac{1}{6}\det \begin{bmatrix} 1 & 1 & 1 & 1 \\ x_1 & x_2 & x_3 & x_4 \\ y_1 & y_2 & y_3 & y_4 \\ z_1 & z_2 & z_3 & z_4 \end{bmatrix}. \tag{2.2.}$$

To simplify the geometrical description of tetrahedral elements a set of local coordinates ζ_1, ζ_2, ζ_3, ζ_4 is introduced (see Figure 2.3.). The value of ζ_i is one at corner i, zero at the other three corners which make the opposite face, and varies linearly in between. The sum of the four coordinates is equal to one:

$$\zeta_1 + \zeta_2 + \zeta_3 + \zeta_4 = 1. \tag{2.3.}$$

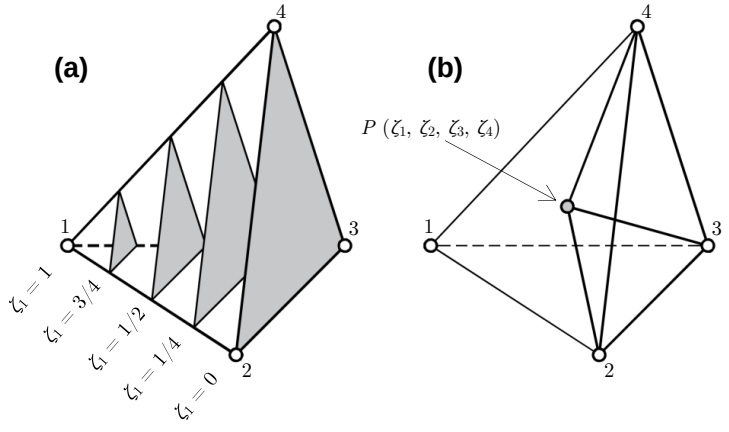

Figure 2.3.: Natural coordinates of the tetrahedron.

Any linear function $F(x, y, z)$, that has values $F_i (i = 1, 2, 3, 4)$ at the corners may be interpolated in terms of the tetrahedron coordinates as:

$$F(\zeta_1, \zeta_2, \zeta_3, \zeta_4) = F_1\zeta_1 + F_2\zeta_2 + F_3\zeta_3 + F_4\zeta_4 = F_i\zeta_i. \tag{2.4.}$$

The geometric definition of the tetrahedron element is then obtained by applying (2.4.) to x, y and z, and appending the sum of coordinates constraint (2.3.) which gives the the relationship between the global rectangular coordinates and natural coordinates:

$$\begin{bmatrix} 1 \\ x \\ y \\ z \end{bmatrix} = \begin{bmatrix} 1 & 1 & 1 & 1 \\ x_1 & x_2 & x_3 & x_4 \\ y_1 & y_2 & y_3 & y_4 \\ z_1 & z_2 & z_3 & z_4 \end{bmatrix} \begin{bmatrix} \zeta_1 \\ \zeta_2 \\ \zeta_3 \\ \zeta_4 \end{bmatrix}. \tag{2.5.}$$

The natural coordinates can be calculated from the given global rectangular coordinates by inverting the previous relation, wich will result in:

$$\zeta_i(x, y, z) = \frac{1}{6V}(\alpha_i + x\beta_i + y\gamma_i + z\delta_i) \quad \text{where} \quad i = 1, 2, 3, 4. \tag{2.6.}$$

The values of α_1, β_1, γ_1 and δ_1, can be calculated as shown in equation (2.7.). The other are obtained by cyclic permutations of the index i.

$$\alpha_1 = \begin{vmatrix} x_2 & y_2 & z_2 \\ x_3 & y_3 & z_3 \\ x_4 & y_4 & z_4 \end{vmatrix}; \quad \beta_1 = -\begin{vmatrix} 1 & y_2 & z_2 \\ 1 & y_3 & z_3 \\ 1 & y_4 & z_4 \end{vmatrix}; \quad \gamma_1 = -\begin{vmatrix} x_2 & 1 & z_2 \\ x_3 & 1 & z_3 \\ x_4 & 1 & z_4 \end{vmatrix}; \quad \delta_1 = -\begin{vmatrix} x_2 & y_2 & 1 \\ x_3 & y_3 & 1 \\ x_4 & y_4 & 1 \end{vmatrix} \tag{2.7.}$$

The displacement field over the tetrahedron element is defined by three components u_x, u_y, u_z which are linearly interpolated over the element from nodal values:

$$\begin{bmatrix} u_x \\ u_y \\ u_z \end{bmatrix} = \begin{bmatrix} u_{x1} & u_{x2} & u_{x3} & u_{x4} \\ u_{y1} & u_{y2} & u_{y3} & u_{y4} \\ u_{z1} & u_{z2} & u_{z3} & u_{z4} \end{bmatrix} \begin{bmatrix} \zeta_1 \\ \zeta_2 \\ \zeta_3 \\ \zeta_4 \end{bmatrix}. \tag{2.8.}$$

Combining this with the geometric definition (2.5.) gives the isoparametric definition of the 4-node tetrahedron element which simply means that the geometrical (coordinates) and mechanical (displacement) data are interpolated through the element domain with the same interpolation functions:

$$\begin{bmatrix} 1 \\ x \\ y \\ z \\ u_x \\ u_y \\ u_z \end{bmatrix} = \begin{bmatrix} 1 & 1 & 1 & 1 \\ x_1 & x_2 & x_3 & x_4 \\ y_1 & y_2 & y_3 & y_4 \\ z_1 & z_2 & z_3 & z_4 \\ u_{x1} & u_{x2} & u_{x3} & u_{x4} \\ u_{y1} & u_{y2} & u_{y3} & u_{y4} \\ u_{z1} & u_{z2} & u_{z3} & u_{z4} \end{bmatrix} \begin{bmatrix} \zeta_1 \\ \zeta_2 \\ \zeta_3 \\ \zeta_4 \end{bmatrix}. \tag{2.9.}$$

Every node of a tetrahedron element has three displacement components which gives twelve independent displacement components per element in total. The displacement vector can be written in the following way:

$$\mathbf{u}^{el} = \begin{bmatrix} u_{x1} & u_{y1} & u_{z1} & u_{x2} & u_{y2} & u_{z2} & u_{x3} & u_{y3} & u_{z3} & u_{x4} & u_{y4} & u_{z4} \end{bmatrix}^{\mathrm{T}}. \tag{2.10.}$$

The displacement field $\mathbf{u}$ can be related to the node displacement $\mathbf{u}^{el}$ by a 3×12 matrix of shape functions denoted as $\mathbf{N}$.

$$\mathbf{u} = \mathbf{N}\, \mathbf{u}^{el} \tag{2.11.}$$

For component-wise node displacement ordering, matrix $\mathbf{N}$ has the following form:

$$\mathbf{N} = \begin{bmatrix} N_1 & 0 & 0 & N_2 & 0 & 0 & N_3 & 0 & 0 & N_4 & 0 & 0 \\ 0 & N_1 & 0 & 0 & N_2 & 0 & 0 & N_3 & 0 & 0 & N_4 & 0 \\ 0 & 0 & N_1 & 0 & 0 & N_2 & 0 & 0 & N_3 & 0 & 0 & N_4 \end{bmatrix}, \tag{2.12.}$$

in which the functions $\mathbf{N}_i$ are given by:

$$\mathbf{N}(x, y, z) = \frac{1}{6V}(\alpha_i + x\beta_i + y\gamma_i + z\delta_i) \quad \text{where} \quad i = 1, 2, 3, 4. \tag{2.13.}$$

Equations (2.13.) and (2.6.) shows that the shape functions $\mathbf{N}_i$ are equal to the functions

ζ_i. Accordingly, the equation (2.9.) can be rewritten in the following form, restating the isoparametric property of the linear tetrahedron element:

$$\begin{bmatrix} 1 \\ x \\ y \\ z \\ u_x \\ u_y \\ u_z \end{bmatrix} = \begin{bmatrix} 1 & 1 & 1 & 1 \\ x_1 & x_2 & x_3 & x_4 \\ y_1 & y_2 & y_3 & y_4 \\ z_1 & z_2 & z_3 & z_4 \\ u_{x1} & u_{x2} & u_{x3} & u_{x4} \\ u_{y1} & u_{y2} & u_{y3} & u_{y4} \\ u_{z1} & u_{z2} & u_{z3} & u_{z4} \end{bmatrix} \begin{bmatrix} N_1 \\ N_2 \\ N_3 \\ N_4 \end{bmatrix}. \tag{2.14.}$$

From equations (2.5.) and (2.13.) can easily derived the following relations that connect partial derivatives of Cartesian and natural coordinates.

$$\frac{\partial x}{\partial \xi_i} = x_1, \quad \frac{\partial y}{\partial \xi_i} = y_1, \quad \frac{\partial z}{\partial \xi_i} = z_1, \qquad i = 1, 2, 3, 4 \tag{2.15.}$$

$$\frac{\partial \xi_i}{\partial x} = \frac{1}{6V}\beta_i, \quad \frac{\partial \xi_i}{\partial y} = \frac{1}{6V}\gamma_i, \quad \frac{\partial \xi_i}{\partial z} = \frac{1}{6V}\delta_i, \qquad i = 1, 2, 3, 4 \tag{2.16.}$$

Partial derivatives of a function $F(\xi_1, \xi_2, \xi_3, \xi_4)$ with respect to Cartesian coordinates follow from (2.16.) and the chain rule:

$$\begin{aligned} \frac{\partial F}{\partial x} &= \frac{\partial F}{\partial \xi_1}\frac{\partial \xi_i}{\partial x} = \frac{1}{6V}\left(\frac{\partial F}{\partial \xi_1}\beta_1 + \frac{\partial F}{\partial \xi_2}\beta_2 + \frac{\partial F}{\partial \xi_3}\beta_3 + \frac{\partial F}{\partial \xi_4}\beta_4\right) = \frac{\beta_i}{6V}\frac{\partial F}{\partial \xi_i} \\ \frac{\partial F}{\partial y} &= \frac{\partial F}{\partial \xi_1}\frac{\partial \xi_i}{\partial y} = \frac{1}{6V}\left(\frac{\partial F}{\partial \xi_1}\gamma_1 + \frac{\partial F}{\partial \xi_2}\gamma_2 + \frac{\partial F}{\partial \xi_3}\gamma_3 + \frac{\partial F}{\partial \xi_4}\gamma_4\right) = \frac{\gamma_i}{6V}\frac{\partial F}{\partial \xi_i}. \\ \frac{\partial F}{\partial z} &= \frac{\partial F}{\partial \xi_1}\frac{\partial \xi_i}{\partial z} = \frac{1}{6V}\left(\frac{\partial F}{\partial \xi_1}\delta_1 + \frac{\partial F}{\partial \xi_2}\delta_2 + \frac{\partial F}{\partial \xi_3}\delta_3 + \frac{\partial F}{\partial \xi_4}\delta_4\right) = \frac{\delta_i}{6V}\frac{\partial F}{\partial \xi_i} \end{aligned} \tag{2.17.}$$

In (2.17.) summation convention over $i = 1, 2, 3, 4$ applies to the indexed expressions.

2.1.2. Trilinear hexahedral elements

The trilinear hexahedron element, also known in literature as *brick*, is topologically equivalent to a cube. It has eight corners, twelve edges or sides, and six faces. Figure (2.4.) shows a eight-node hexahedron in the global coordinate system (x, y, z) together with the axes of the natural coordinates (ξ, η, μ).

The natural coordinates (ξ, η, μ) vary from -1 on one face to $+1$ on the opposite face, taking the zero value on the median face. The values of the natural coordinates of the corners are given in Table (2.1.). The local numbering rule of the nodes is shown in Figure (2.4.). First, a starting face and a starting node on that face has to be chosen

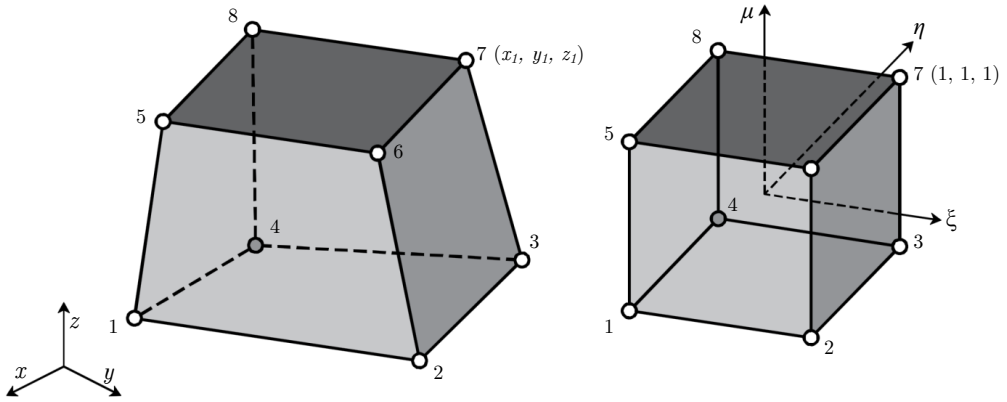

Figure 2.4.: The eight-node hexahedron in the Cartesian coordinate system and in the natural coordinate system in which becomes a cube.

Table 2.1.: Values of the natural coordinates at the corner of a hexahedral element

node	ξ	η	μ
1	-1	-1	-1
2	$+1$	-1	-1
3	-1	$+1$	-1
5	-1	-1	$+1$
6	$+1$	-1	$+1$
7	$+1$	$+1$	$+1$
8	-1	$+1$	$+1$

and is given number 1. The other three nodes on the starting face are numbered 2, 3 and 4 in a anticlockwise manner while looking the starting face from the opposite one. The nodes on the opposite face are then numbered 5, 6, 7, 8 and are directly opposite to 1, 2, 3, 4. This rule guarantees a positive volume, or more precisely, a positive Jacobian determinant at every point.

The hexahedral element is defined by the equation (2.18.), analogue to (2.14.) for the tetrahedral element:

$$\begin{bmatrix} 1 \\ x \\ y \\ z \\ u_x \\ u_y \\ u_z \end{bmatrix} = \begin{bmatrix} 1 & 1 & 1 & 1 & 1 & 1 & 1 & 1 \\ x_1 & x_2 & x_3 & x_4 & x_5 & x_6 & x_7 & x_8 \\ y_1 & y_2 & y_3 & y_4 & y_5 & y_6 & y_7 & y_8 \\ z_1 & z_2 & z_3 & z_4 & z_5 & z_6 & z_7 & z_8 \\ u_{x1} & u_{x2} & u_{x3} & u_{x4} & u_{x5} & u_{x6} & u_{x7} & u_{x7} \\ u_{y1} & u_{y2} & u_{y3} & u_{y4} & u_{y5} & u_{y6} & u_{y7} & u_{y8} \\ u_{z1} & u_{z2} & u_{z3} & u_{z4} & u_{z5} & u_{z6} & u_{z7} & u_{z8} \end{bmatrix} \begin{bmatrix} N_1 \\ N_2 \\ N_3 \\ N_4 \\ N_5 \\ N_6 \\ N_7 \\ N_8 \end{bmatrix}. \tag{2.18.}$$

The shape functions N are:

$$\begin{aligned} N_1 &= \tfrac{1}{8}(1-\xi)(1-\eta)(1-\mu), & N_2 &= \tfrac{1}{8}(1+\xi)(1-\eta)(1-\mu), \\ N_3 &= \tfrac{1}{8}(1+\xi)(1+\eta)(1-\mu), & N_4 &= \tfrac{1}{8}(1-\xi)(1+\eta)(1-\mu), \\ N_5 &= \tfrac{1}{8}(1-\xi)(1-\eta)(1+\mu), & N_6 &= \tfrac{1}{8}(1+\xi)(1-\eta)(1+\mu), \\ N_7 &= \tfrac{1}{8}(1+\xi)(1+\eta)(1+\mu), & N_8 &= \tfrac{1}{8}(1-\xi)(1+\eta)(1+\mu). \end{aligned} \tag{2.19.}$$

The equations 2.19. can be summarized as:

$$N_i = \tfrac{1}{8}(1+\xi\xi_i)(1+\eta\eta_i)(1+\mu\mu_i) \tag{2.20.}$$

where ξ_i, η_i and μ_i denote the coordinates of the i^{th} node as is shown in table (2.1.). The derivates of the shape functions are then given by the usual chain rule formulas:

$$\begin{aligned} \frac{\partial N_i}{\partial x} &= \frac{\partial N_i}{\partial \xi}\frac{\partial \xi}{\partial x} + \frac{\partial N_i}{\partial \eta}\frac{\partial \eta}{\partial x} + \frac{\partial N_i}{\partial \mu}\frac{\partial \mu}{\partial x}, \\ \frac{\partial N_i}{\partial y} &= \frac{\partial N_i}{\partial \xi}\frac{\partial \xi}{\partial y} + \frac{\partial N_i}{\partial \eta}\frac{\partial \eta}{\partial y} + \frac{\partial N_i}{\partial \mu}\frac{\partial \mu}{\partial y}, \\ \frac{\partial N_i}{\partial z} &= \frac{\partial N_i}{\partial \xi}\frac{\partial \xi}{\partial z} + \frac{\partial N_i}{\partial \eta}\frac{\partial \eta}{\partial z} + \frac{\partial N_i}{\partial \mu}\frac{\partial \mu}{\partial z}. \end{aligned} \tag{2.21.}$$

In matrix form:

$$\begin{bmatrix} \frac{\partial N_i}{\partial x} \\ \frac{\partial N_i}{\partial y} \\ \frac{\partial N_i}{\partial z} \end{bmatrix} = \begin{bmatrix} \frac{\partial \xi}{\partial x} & \frac{\partial \eta}{\partial x} & \frac{\partial \mu}{\partial x} \\ \frac{\partial \xi}{\partial y} & \frac{\partial \eta}{\partial y} & \frac{\partial \mu}{\partial y} \\ \frac{\partial \xi}{\partial z} & \frac{\partial \eta}{\partial z} & \frac{\partial \mu}{\partial z} \end{bmatrix} \begin{bmatrix} \frac{\partial N_i}{\partial \xi} \\ \frac{\partial N_i}{\partial \eta} \\ \frac{\partial N_i}{\partial \mu} \end{bmatrix}. \tag{2.22.}$$

The 3×3 matrix in (2.22.) is the inverse of the *Jacobian matrix* $\mathbf{J}^{-1}$ of (x, y, z) with respect to (ξ, η, μ). The Jacobian matrix $\mathbf{J}$, or simply the Jacobian, is then:

$$\mathbf{J} = \frac{\partial(x,y,z)}{\partial(\xi,\eta,\mu)} = \begin{bmatrix} \frac{\partial x}{\partial \xi} & \frac{\partial y}{\partial \xi} & \frac{\partial z}{\partial \xi} \\ \frac{\partial x}{\partial \eta} & \frac{\partial y}{\partial \eta} & \frac{\partial z}{\partial \eta} \\ \frac{\partial x}{\partial \mu} & \frac{\partial y}{\partial \mu} & \frac{\partial z}{\partial \mu} \end{bmatrix}. \tag{2.23.}$$

The isoparametric definition of hexahedron element geometry can be restated as, see (2.18.):

$$x = x_i\, N_i, \quad y = y_i\, N_i, \quad z = z_i\, N_i \tag{2.24.}$$

where the summation convention is implied over $i = 1, 2, ..., 8$. The Jacobian matrix $\mathbf{J}$ can be constructed by differentiating these relations with respect to the natural coordinates:

$$\mathbf{J} = \begin{bmatrix} x_i \dfrac{\partial N_i}{\partial \xi} & y_i \dfrac{\partial N_i}{\partial \xi} & z_i \dfrac{\partial N_i}{\partial \xi} \\ x_i \dfrac{\partial N_i}{\partial \eta} & y_i \dfrac{\partial N_i}{\partial \eta} & z_i \dfrac{\partial N_i}{\partial \eta} \\ x_i \dfrac{\partial N_i}{\partial \mu} & y_i \dfrac{\partial N_i}{\partial \mu} & z_i \dfrac{\partial N_i}{\partial \mu} \end{bmatrix}. \tag{2.25.}$$

For a given point with coordinates (ξ, η, μ), using the relation (2.25.), the Jacobian can be easily computed.

2.2. Temporal discretisation

2.2.1. Dynamic equilibrium equation

The dynamic equilibrium equation governing the dynamic response of a system of finite elements is derived from the principle of virtual displacements and can be written in a matrix form as:

$$\mathbf{M}\,\ddot{\mathbf{u}}(t) \;+\; \mathbf{C}\,\dot{\mathbf{u}}(t) \;+\; \mathbf{K}\,\mathbf{u}(t) \;=\; \mathbf{R}(t), \tag{2.26.}$$

where $\mathbf{M}$, $\mathbf{C}$ and $\mathbf{K}$ are the mass, damping and stiffness matrices; $\mathbf{R}$ is the vector of externally applied loads; and $\mathbf{u}$, $\dot{\mathbf{u}}$, and $\ddot{\mathbf{u}}$ are the displacement, velocity, and acceleration vectors. The consistent mass matrix $\mathbf{M}$ and the stiffness matrix $\mathbf{K}$ can be obtain as:

$$\mathbf{M} = \int_{\Omega_{el}} \mathbf{N}^{\mathrm{T}} \rho\, \mathbf{N}\, \mathrm{d}\Omega_{el}, \qquad \mathbf{K} = \int_{\Omega_{el}} \mathbf{B}^{\mathrm{T}}\, \mathbf{D}\, \mathbf{B}\, \mathrm{d}\Omega_{el}, \tag{2.27.}$$

where $\mathbf{N}$ is the finite element interpolation function matrix; ρ is the material density; $\mathbf{B}$ is the strain-displacement matrix; and $\mathbf{D}$ is the stress-strain matrix. These integrals are taken over the element domain Ω, i.e. the element volume V. The damping matrix $\mathbf{C}$ is constructed as a linear combination of the mass and stiffness matrix with coefficients α and β:

$$\mathbf{C} = \alpha\mathbf{M} + \beta\mathbf{K}. \tag{2.28.}$$

The vector of externally applied forces consists of body (volume) forces $\mathbf{b}$ and surface (traction) forces $\mathbf{t}$:

$$\mathbf{R} = \int_{\Omega_{el}} \mathbf{N}^{\mathrm{T}}\, \mathbf{b}\, \mathrm{d}\Omega_{el} + \int_{\Gamma_{el}} \mathbf{N}^{\mathrm{T}}\, \mathbf{t}\, \mathrm{d}\Gamma_{el}. \tag{2.29.}$$

Additionally, the vector of externally applied forces may include node forces and initial stress effects.

2.2.2. Time integration

Mathematically, equation (2.26.) represents a system of linear differential equations of a second order and usually is solved by direct integration methods. The *direct* integration means that the equation (2.26.) is integrated using numerical *step-by-step* procedure without transforming the equation in a different form. Two basic ideas are behind the direct numerical integration. (1) Instead of trying to satisfy the equation (2.26.) at any time t, it does only at discrete time intervals Δt, usually equidistant one from the other. In other words, the inertia, damping and internal forces are calculated at the discrete time points. (2) The variation of displacement, velocities and accelerations within each time interval Δt is assumed. This assumption on the form of variation within each time interval determines the accuracy, stability, and cost of the procedure.

The equation (2.26.) can be regarded as a system of ordinary differential equations with constant coefficients, meaning that the accelerations, velocities, and displacement can be approximated by any finite difference expression. The solution at time $t + \Delta t$ is then based on using the equilibrium conditions at time t. For that reason these integration procedures are called *explicit time integrations methods*. In the presented model two finite difference expressions are used, commonly known as *central difference method* (Bathe, 1996) and *leap frog method* (Crisfield, 1991). Figure (2.5.) shows the time stepping procedure for both methods. It is assumed that the displacements, velocities, and acceleration vectors at time $t = 0$ (initial conditions) are known and that the time step Δt is constant. The displacement solution for time $t+\Delta t$ is obtained by considering

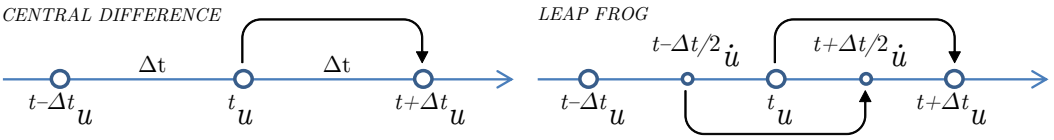

Figure 2.5.: Time stepping for the central difference method and for the leap-frog method.

the equation (2.26.) at time t, i.e.,

$$\mathbf{M}\ {}^{t}\ddot{\mathbf{u}} + \mathbf{C}\ {}^{t}\dot{\mathbf{u}} + \mathbf{K}\ {}^{t}\mathbf{u} = {}^{t}\mathbf{R}. \tag{2.30.}$$

In case of central difference method the accelerations and velocities are approximated in the following way which has an error in the order of $(\Delta t)^2$:

$$ {}^{t}\ddot{\mathbf{u}} = \frac{1}{\Delta t}({}^{t-\Delta t}\mathbf{u} - 2\,{}^{t}\mathbf{u} + {}^{t+\Delta t}\mathbf{u}) \tag{2.31.} $$

$$ {}^{t}\dot{\mathbf{u}} = \frac{1}{2\Delta t}({}^{t+\Delta t}\mathbf{u} - {}^{t-\Delta t}\mathbf{u}). \tag{2.32.} $$

Substituting the relations for ${}^{t}\ddot{\mathbf{u}}$ and ${}^{t}\dot{\mathbf{u}}$, equations (2.31.) and (2.32.) respectively, into (2.30.) leads to:

$$ \left(\tfrac{1}{\Delta t^2}\mathbf{M} + \tfrac{1}{2\Delta t}\mathbf{C}\right){}^{t+\Delta t}\mathbf{u} = {}^{t}\mathbf{R} - \left(\mathbf{K} - \tfrac{2}{\Delta t^2}\mathbf{M}\right){}^{t}\mathbf{u} - \left(\tfrac{1}{\Delta t^2}\mathbf{M} + \tfrac{1}{2\Delta t}\mathbf{C}\right){}^{t-\Delta t}\mathbf{u}, \tag{2.33.} $$

which can be solved for ${}^{t+\Delta t}\mathbf{u}$. In more compact form the unknown displacement vector ${}^{t+\Delta t}\mathbf{u}$ can be expressed as:

$$ {}^{t+\Delta t}\mathbf{u} = \hat{\mathbf{M}}^{-1}.\,{}^{t}\hat{\mathbf{R}}, \tag{2.34.} $$

where the effective mass matrix $\hat{\mathbf{M}}$ and the effective load ${}^{t}\hat{\mathbf{R}}$ are calculated as:

$$ \hat{\mathbf{M}} = \frac{1}{\Delta t^2}\mathbf{M} + \frac{1}{2\Delta t}\mathbf{C}, \tag{2.35.} $$

and

$$ {}^{t}\hat{\mathbf{R}} = {}^{t}\mathbf{R} - \left(\mathbf{K} - \frac{1}{\Delta t^2}\mathbf{M}\right){}^{t}\mathbf{u} - \left(\frac{1}{\Delta t^2}\mathbf{M} - \frac{1}{2\Delta t}\mathbf{C}\right){}^{t-\Delta t}\mathbf{u}. \tag{2.36.} $$

The calculation of ${}^{t+\Delta t}\mathbf{u}$ obviously involves calculation of ${}^{t}\mathbf{u}$ and ${}^{t-\Delta t}\mathbf{u}$. Because of this at the very start of the procedure an additional step has to be carried out for calculating ${}^{0-\Delta t}\mathbf{u}$. Since the initial displacement ${}^{0}\mathbf{u}$, velocity ${}^{0}\dot{\mathbf{u}}$ and acceleration ${}^{0}\ddot{\mathbf{u}}$ are known, the relations (2.31.) and (2.32.) can be used to obtain ${}^{0-\Delta t}\mathbf{u}$:

$$ {}^{0-\Delta t}\mathbf{u} = {}^{0}\mathbf{u} - \Delta t\ {}^{0}\dot{\mathbf{u}} + \frac{\Delta t^2}{2}\,{}^{0}\ddot{\mathbf{u}}. \tag{2.37.} $$

Since this solution requires large number of time steps of a small size, the overall effectiveness of the procedure depends on the effectiveness of a single step solution. Consequently, explicit methods are viable methods only when a lumped mass matrix can be assumed. In that case, the inversion of the lumped mass matrix (diagonal matrix) becomes trivial and the components of the displacement vector at time $t + \Delta t$ can be calculated as follows:

$$ {}^{t+\Delta t}u_i = \frac{\Delta t}{M_{ii}}\,{}^{t}\hat{R}_i. \tag{2.38.} $$

It is also important to note that the product $\mathbf{K}\,{}^{t}\mathbf{u}$ represents internal forces at time t which can be obtain by stress integration at element level. In other word, it is not

necessary to assemble the stiffness matrix so the relation (2.36.) can be rewritten as:

$$^{t}\hat{\mathbf{R}} = {}^{t}\mathbf{R} - {}^{t}\mathbf{F}^{\text{int}} - \frac{1}{\Delta t^2}\mathbf{M}\left({}^{t-\Delta t}\mathbf{u} - 2\,{}^{t}\mathbf{u}\right). \tag{2.39.}$$

Considering now the equation (2.38.) with (2.39.) it becomes clear that the solution can be carried out on a element level. That means that relatively little high speed storage is required which makes this procedure attractive for large systems.

In case of the leap-frog method the time-stepping runs in a staggered way: velocities are advanced in half-time steps while the displacements in full time steps (see Figure 2.5.). It is a second-order integration scheme like the central difference method but more widely used. The velocities in the half time steps can be approximated as:

$$^{t+\Delta t/2}\dot{\mathbf{u}} = \frac{^{t+\Delta t}\mathbf{u} - {}^{t}\mathbf{u}}{\Delta t}; \qquad ^{t-\Delta t/2}\dot{\mathbf{u}} = \frac{^{t}\mathbf{u} - {}^{t-\Delta t}\mathbf{u}}{\Delta t}. \tag{2.40.}$$

Assuming a lumped mass and damping matrix the velocity at time $t + \Delta t/2$ can be calculated as:

$$^{t+\Delta t/2}\dot{u} = \frac{2M_{ii} - \Delta t C_{ii}}{2M_{ii} + \Delta t C_{ii}}\ ^{t-\Delta t/2}\dot{u}_i \ + \ \frac{2\Delta t}{2M_{ii} + \Delta t C_{ii}}(^{t}R - {}^{t}F^{int}). \tag{2.41.}$$

The unknown displacements vector is then calculated as:

$$^{t+\Delta t}\mathbf{u} = {}^{t}\mathbf{u} + {}^{t+\Delta t/2}\mathbf{v}\Delta t. \tag{2.42.}$$

Regardless of the applied finite approximation method the adopted time step Δt has to be smaller than a critical value Δt_{cr} to obtain a valid solution. These schemes are said to be conditionally stable, i.e. for a time step larger than the critical one, any errors from round-off rapidly accumulate blowing up the solution. Therefore, the time step should be carefully chosen - small enough to insure a stable solution, but not too small so that the procedure remains efficient.

Two conditions should be respected. Firstly, according to the CLF condition after Courant, Friedrichs an Lewy (Courant et al., 1967) the time step is evaluated on element level as:

$$\Delta t < \frac{L_e}{\sqrt{\frac{1-\nu}{(1+\nu)(1-2\nu)}\frac{E}{\rho}}}, \tag{2.43.}$$

where L_e is the characteristic element length, ν is the Poisson's ratio, E Young's modulus, and ρ material density. The characteristic element length for tetrahedrons is the minimum altitude, and for hexahedrons is the ratio of the element volume and the area of the largest element surface. Equation (2.43.) essentially says that the the selected

time step must be smaller than the time needed for the body wave to travel across the element.

Secondly, the adopted time step should also comply to the following condition:

$$\Delta t < \frac{2}{\omega_{max}}, \tag{2.44.}$$

where ω_{max} is the largest element frequency of all elements in the mesh (Bathe, 1996).

These conditions stand for linear dynamic analysis, but can be also applied for dynamic non-linear analysis. It is important to note that in non-linear analysis the periods and wave velocities in the finite element system change during its response. To insure the stability of the analysis it is prudent to introduce a safety factor. In the presented studies the calculated time step according to conditions (2.43.) and (2.44.) was reduced by multiplying it with a factor 0.9.

Details about the efficiency of the presented explicit integration methods, their advantages and disadvantages and more are discussed in Chapter 6. For contact analysis the equation (2.26.) has to be modified by applying the forward incremental Lagrangian multipliers method and adding the impermeability condition which is discussed in detail in Chapter 5.

Chapter 3.

Geometrical non-linearity

Geometrical non-linearity can be safely neglected for the first problem studied since the displacements and rotations are not large. On the other hand, the nature of the second problem (sliding and rocking of the foundations) requires the inclusion of geometrical non-linear effects. This chapter introduce the adopted *Total Lagrange formulation* used in the FE code to account for large rotations and displacements.

3.1. Finite strain theory preliminaries

In continuum mechanics the finite strain theory (as opposed to the infinitesimal strain theory) deals with deformations in which both the rotations and strains can be arbitrarily large (see Figure 3.1.). Since the deformed and undeformed configurations of a body can be significantly different, a clear distinction has to be made between them. The change in the configuration of a continuum body is described by the displacement (vector) field which relates the deformed configuration with the undeformed configuration.

Every geometrical non-linearity analysis is based on different configurations of the structure. Among many configurations used, the three most important are: *base configuration* (the configuration defined as the origin of displacements, strain free but not necessarily stress free), *reference configuration* (configuration to which stepping computations in a incremental solution process are referred) and, *current configuration* (any admissible configuration taken during the analysis process). Different configurations taken by a body during the analysis are linked by Cartesian global frames: the *material global frame* with axes (X_1, X_2, X_3) and the *spatial global frame* with axes (x_1, x_2, x_3) with the usual notation as in Crisfield (1991, 1997), Bathe (1996) and Bonet and Wood (2008)). While the material frame track the base configuration, the spatial frame tracks all others.

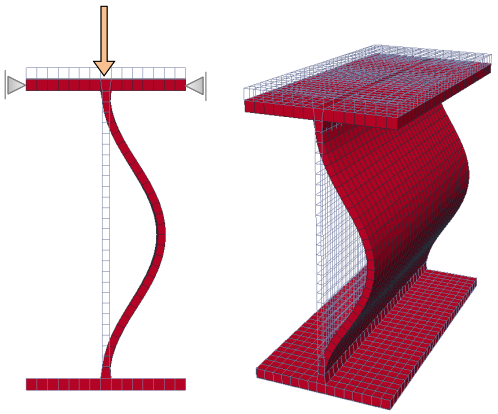

Figure 3.1.: Web buckling of a steel I profile.

The displacement of a body can be broken to two components: (1) rigid-body displacement and, (2) deformation. Rigid-body displacement consists of a translation and a rotation of the body without changing its shape or size. Deformation represents the change in shape and/or size of the body $\mathcal{B}$ from a base (initial undeformed) configuration $\kappa_0(\mathcal{B})$ to a current (deformed) configuration $\kappa_t(\mathcal{B})$.

The kinematic aspect of motion is illustrated in Figure (3.2.). Consider a particle P (P $\subset \mathcal{B}$) in the base (undeformed) configuration and the related particle p in the current (deformed) configuration. The base configuration is related to the coordinate system with the origin at O with unit vectors $\mathbf{E}_1, \mathbf{E}_2, \mathbf{E}_3$ and the current configuration is related to the coordinate system with the origin at o with unit vectors $\mathbf{e}_1, \mathbf{e}_2, \mathbf{e}_3$. The position of particle P in the base configuration is defined with vector $\mathbf{X}$ and, similarly, the position of particle p in the current configuration is defined with vector $\mathbf{x}$.

In the Lagrangian description the displacement vector is:

$$\mathbf{u}(\mathbf{X}, t) = u_i \mathbf{e}_i. \tag{3.1.}$$

Expressed in terms of material coordinates, the displacement field is:

$$\mathbf{u}(\mathbf{X}, t) = \mathbf{b}(t) + \mathbf{x}(\mathbf{X}, t) - \mathbf{X} \qquad \text{or} \qquad u_i = \alpha_{iJ} b_J + x_i - \alpha_{iJ} X_J \tag{3.2.}$$

where $\mathbf{b}$ is the vector by which the coordinate system translation is given, and α_{iJ} are the direction cosines between the material and spatial coordinate systems with unit vectors $\mathbf{E}_J$ and $\mathbf{e}_i$, respectively. Thus $\mathbf{E_J} \cdot \mathbf{e}_i = \alpha_{Ji} = \alpha_{iJ}$.

In the Eulerian description the displacement vector is:

$$\mathbf{U}(\mathbf{X}, t) = U_i \mathbf{E}_i. \tag{3.3.}$$

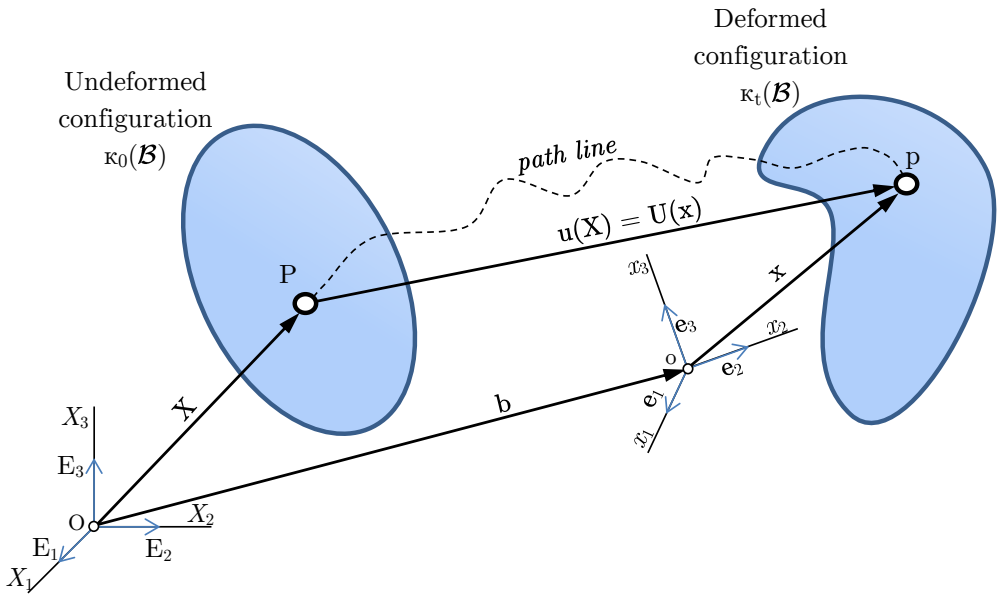

Figure 3.2.: Motion of a continuum body.

Expressed in terms of spatial coordinates, the displacement field is:

$$\mathbf{U}(\mathbf{x},t) = \mathbf{b}(t) + \mathbf{x} - \mathbf{X}(\mathbf{x},t) \qquad \text{or} \qquad U_i = b_J + \alpha_{Ji}x_i - X_J. \tag{3.4.}$$

The relationship between u_i and U_j is then given by $u_i = \alpha_{iJ}U_J$ or $U_J = \alpha_{Ji}u_i$. The relationship between the material and spatial coordinate system can be then expressed as:

$$\mathbf{u}(\mathbf{X},t) = u_i\mathbf{e}_i = u_i(\alpha_{iJ}E_J) = U_J\mathbf{E}_J = \mathbf{U}(\mathbf{x},t). \tag{3.5.}$$

The description of finite strain can be simplified by assuming that the two coordinate systems are identical, i.e. $\mathbf{b}$ becomes equal to 0 and the direction cosines become Kronecker deltas: $\mathbf{E}_J \cdot \mathbf{e}_i = \delta_{Ji} = \delta_{iJ}$. The displacement then may be expressed in material (deformed) coordinates as:

$$\mathbf{u}(\mathbf{X},t) = \mathbf{x}(\mathbf{X},t) - \mathbf{X} \qquad \text{or} \qquad u_i = x_i - \delta_{iJ}X_J \tag{3.6.}$$

and in spatial (undeformed) coordinates as:

$$\mathbf{U}(\mathbf{x},t) = \mathbf{x} - \mathbf{X}(\mathbf{x},t) \qquad \text{or} \qquad U_i = \delta_{Ji}x_i - X_J. \tag{3.7.}$$

Figure (3.3.) shows deformation of a continuum body where the material and spatial coordinate systems are identical and the body experiences deformation that change its shape and/or size. Consider two neighbouring points Q and P with positions defined by vectors $\mathbf{X}$ and $\mathbf{X} + \mathrm{d}\mathbf{X}$, respectively. In the deformed configuration at time t they become points p and q with position vectors $\mathbf{x}$ and $\mathbf{x} + \mathrm{d}\mathbf{x}$.

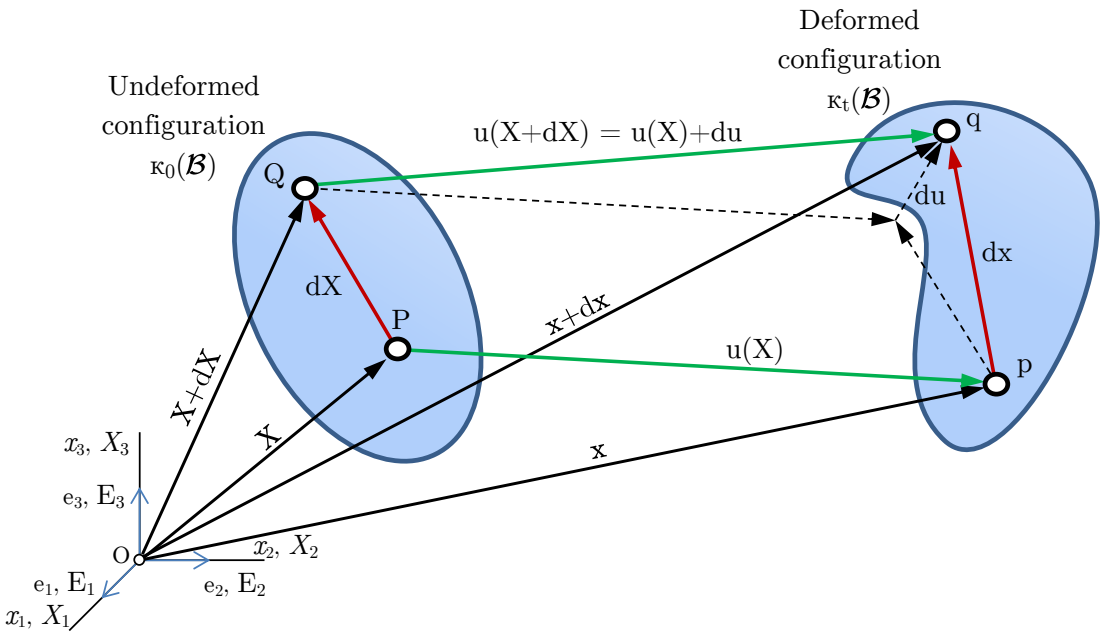

Figure 3.3.: Deformation of a continuum body.

From Figure (3.3.) follows:

$$\begin{aligned} \mathbf{x} + \mathrm{d}\mathbf{x} &= \mathbf{X} + \mathrm{d}\mathbf{X} + \mathbf{u}(\mathbf{X} + \mathbf{u}\mathbf{X}) \\ \mathrm{d}\mathbf{x} &= \mathbf{X} - \mathbf{x} + \mathrm{d}\mathbf{X} + \mathbf{u}(\mathbf{X} + \mathbf{u}\mathbf{X}) \\ &= \mathrm{d}\mathbf{X} + \mathbf{u}(\mathbf{X} + \mathrm{d}\mathbf{X}) - \mathbf{u}(\mathbf{X}) \\ &= \mathrm{d}\mathbf{X} + \mathrm{d}\mathbf{u}, \end{aligned} \tag{3.8.}$$

where d$\mathbf{u}$ is the relative displacement vector, which represents the relative displacement of Q with respect to P in the deformed configuration.

A fundamental measure od deformation of the body is given by the *deformation gradient*. The deformation gradient is a second order tensor, so called two-point tensor that describes the stretches and rotations that the material fibres have undergone from time 0 to time t. Consequently and according to the previously introduced notation it should be denoted as ${}^t_0\mathbf{F}$ (Bathe, 1996). For simplicity, in the following discussion the left subscript and superscript are omitted but always implied. The derivatives of (x_1, x_2, x_3) with respect to (X_1, X_2, X_3), arranged in Jacobian format, constitute the deformation gradient:

$$\mathbf{F} = \frac{\partial(x_1, x_2, x_3)}{\partial(X_1, X_2, X_3)} = \begin{bmatrix} \frac{\partial x_1}{\partial X_1} & \frac{\partial x_1}{\partial X_2} & \frac{\partial x_1}{\partial X_3} \\ \frac{\partial x_2}{\partial X_1} & \frac{\partial x_2}{\partial X_2} & \frac{\partial x_2}{\partial X_3} \\ \frac{\partial x_3}{\partial X_1} & \frac{\partial x_3}{\partial X_2} & \frac{\partial x_3}{\partial X_3} \end{bmatrix}. \tag{3.9.}$$

The inverse relation gives the derivatives of (X_1, X_2, X_3) with respect to (x_1, x_2, x_3) as:

$$\mathbf{F}^{-1} = \frac{\partial(X_1, X_2, X_3)}{\partial(x_1, x_2, x_3)} = \begin{bmatrix} \frac{\partial X_1}{\partial x_1} & \frac{\partial X_1}{\partial x_2} & \frac{\partial X_1}{\partial x_3} \\ \frac{\partial X_2}{\partial x_1} & \frac{\partial X_2}{\partial x_2} & \frac{\partial X_2}{\partial x_3} \\ \frac{\partial X_3}{\partial x_1} & \frac{\partial X_3}{\partial x_2} & \frac{\partial X_3}{\partial x_3} \end{bmatrix}. \tag{3.10.}$$

The coordinate differentials can be related using these matrices:

$$\mathrm{d}\mathbf{x} = \mathbf{F}\ \mathrm{d}\mathbf{X}, \qquad \mathrm{d}\mathbf{X} = \mathbf{F}^{-1}\mathrm{d}\mathbf{x}. \tag{3.11.}$$

From the above can be derived that the volume and density at time t can be related to the volume V and density ρ at time 0 by:

$$\frac{{}^0V}{{}^tV} = \frac{{}^0\rho}{{}^t\rho} = \mathrm{det}\mathbf{F} = J, \tag{3.12.}$$

where J is called the Jacobian of deformation and is equal to the determinant of the deformation gradient.

Considering (3.8.) the deformation gradient defined in (3.9.) can be restated with the displacements:

$$\mathbf{F} = \begin{bmatrix} \frac{\partial u_1}{\partial X_1} & \frac{\partial u_1}{\partial X_2} & \frac{\partial u_1}{\partial X_3} \\ \frac{\partial u_2}{\partial X_1} & \frac{\partial u_2}{\partial X_2} & \frac{\partial u_2}{\partial X_3} \\ \frac{\partial u_3}{\partial X_1} & \frac{\partial u_3}{\partial X_2} & \frac{\partial u_3}{\partial X_3} \end{bmatrix} + \begin{bmatrix} 1 & 0 & 0 \\ 0 & 1 & 0 \\ 0 & 0 & 1 \end{bmatrix} = \nabla\mathbf{u} + \mathbf{I}, \tag{3.13.}$$

where $\nabla\mathbf{u}$ is the displacement gradient with respect to the reference configuration, i.e. the material displacement gradient $\mathbf{G}$. The components $\partial u_i/\partial X_j$ can be calculated by derivation of the appropriate shape functions as shown in sections 2.1.1. and 2.1.2.

A very important property of the deformation gradient is that can be always decomposed into a unique product of two matrices: a symmetric matrix corresponding to a *stretch* and a orthogonal matrix corresponding to a *rotation* (Bonet and Wood, 2008):

$$\mathbf{F} = \mathbf{R}\mathbf{U} = \mathbf{v}\mathbf{R} \tag{3.14.}$$

where $\mathbf{R}$ is the orthogonal tensor ($\mathbf{R}\mathbf{R}^{\mathrm{T}} = \mathbf{R}^{\mathrm{T}}\mathbf{R} = \mathbf{I}$ and $\mathbf{R}^{-1} = \mathbf{R}^{\mathrm{T}}$) representing rtotation; $\mathbf{U}$ is the *right stretch* and $\mathbf{v}$ is the *left stretch* symmetric tensor ($\mathbf{U} = \mathbf{U}^{\mathrm{T}}$ and $\mathbf{v} = \mathbf{v}^{\mathrm{T}}$). The terms *right* and *left* mean that they are to the right and left of the

rotation tensor $\mathbf{R}$, respectively. Equation (3.14.) can be interpreted to mean that the motion of a body can be expressed either by a pure stretch followed by a rotation, or by a rotation followed by a pure rotation. This notion is illustrated in Figure (3.4.):

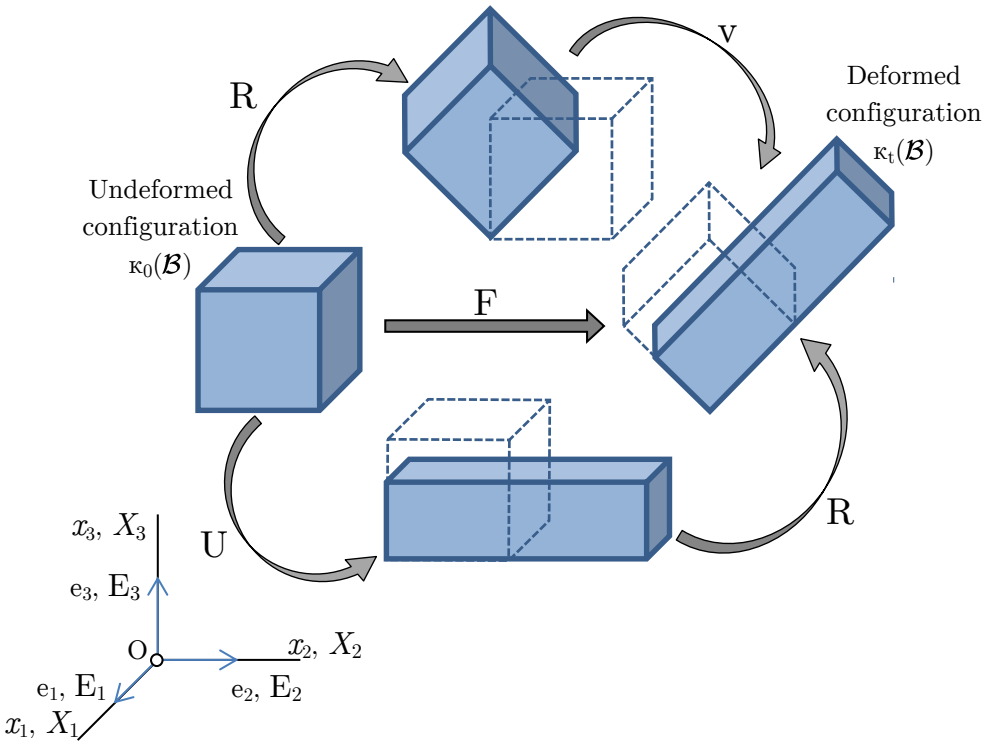

Figure 3.4.: Representation of the polar decomposition of the deformation gradient.

The relation (3.14.) is referred to as the polar decomposition of the deformation gradient. Pre-multiplying (3.14.) with $\mathbf{F}^{\mathrm{T}}$ gives:

$$\mathbf{F}^{\mathrm{T}}\mathbf{F} = \mathbf{F}^{\mathrm{T}}\mathbf{R}\mathbf{U} = \mathbf{U}\mathbf{R}^{\mathrm{T}}\mathbf{R}\mathbf{U} = \mathbf{U}^2 = \mathbf{C}, \qquad \mathbf{U} = \sqrt{\mathbf{F}^{\mathrm{T}}\mathbf{F}} = \sqrt{\mathbf{C}} \tag{3.15.}$$

where $\mathbf{C}$ is called right Cauchy-Green deformation tensor. Similarly, by post-multiplying (3.14.) with $\mathbf{F}^{\mathrm{T}}$ gives:

$$\mathbf{F}\mathbf{F}^{\mathrm{T}} = \mathbf{v}\mathbf{R}\mathbf{F}^{\mathrm{T}} = \mathbf{v}\mathbf{R}\mathbf{R}^{\mathrm{T}}\mathbf{v}^{\mathrm{T}} = \mathbf{v}^2 = \mathbf{B}, \qquad \mathbf{v} = \sqrt{\mathbf{F}\mathbf{F}^{\mathrm{T}}} = \sqrt{\mathbf{B}} \tag{3.16.}$$

where $\mathbf{B}$ is called left Cauchy-Green deformation tensor. Upon taking the square root of $\mathbf{C}$, the rotation can be then computed as $\mathbf{R} = \mathbf{F}\mathbf{U}^{-1}$.

3.2. Total Lagrange formulation

The three most used kinematic descriptions of geometrically non-linear problems in finite element analysis are *Total Lagrangian* (TL), *Updated Lagrangian* (UL) and *Corotational* (CR). They primarily differ in the choice of the reference configuration. In TL the base and reference configurations coalesce and remain fixed throughout the solution. In UL the base configuration remains fixed but the reference configuration is periodically update, usually the reference configuration is set to the last converged solution. In CR the reference configuration is split into base and co-rotated, strains and stresses are measured from co-rotated to current, while base configuration is maintained as reference to measure rigid body motions. For the problems presented in this Thesis, the TL formulation was regarded to be the most appropriate and computationally most efficient.

TL formulation include all kinematic non-linear effects due to large displacements and large rotations. But weather the large strain behaviour is modelled appropriately, actually depends on the constitutive law specified. The basic equation considered in the TL formulation is (Bathe, 1996):

$$\int_{{}^0V} {}^{t+\Delta t}_{0}S_{ij}\ \delta\ {}^{t+\Delta t}_{0}\varepsilon_{ij}\ \mathrm{d}^0V\ =\ {}^{t+\Delta t}\Re, \tag{3.17.}$$

where $\Re$ is the external virtual work, ${}^{t+\Delta t}_{0}S_{ij}$ is the second Piola-Kirchhoff stress tensor (PK2) and ${}^{t+\Delta t}_{0}\varepsilon_{ij}$ is Green-Lagrange strain tensor (GL) integrated over the reference volume ${}^0V$. As the notation suggests both tensors are given at time $t+\Delta t$ with respect to the initial material coordinates at time $t = 0$. The PK2 is the *conjugate* stress measure to GL as the finite strain measure in sense of virtual work (Bathe, 1996; Crisfield, 1997). Precisely, the dot product of stress times the material strain rate is the internal power density.

The Green-Lagrange strain tensor, here denoted simply as $\boldsymbol{\varepsilon}$, can be written in term of Cauchy-Green deformation tensor or in term of gradient of deformation:

$$\boldsymbol{\varepsilon} = \frac{1}{2}\left(\mathbf{C} - \mathbf{I}\right) = \frac{1}{2}\left(\mathbf{F}^{\mathrm{T}}\mathbf{F} - \mathbf{I}\right). \tag{3.18.}$$

Furthermore, its components can be evaluated in terms of displacements (in indicial notation):

$$\varepsilon_{ij} = \frac{1}{2}(u_{i,j} + u_{j,i} + u_{k,i}\,u_{k,j}). \tag{3.19.}$$

The individual components of $\boldsymbol{\varepsilon}$ can obtained by expanding (3.19.):

$$\varepsilon_{ij} = \begin{cases} \dfrac{\partial u_i}{\partial X_i} + \dfrac{1}{2}\left[\left(\dfrac{\partial u_1}{\partial X_i}\right)^2 + \left(\dfrac{\partial u_2}{\partial X_i}\right)^2 + \left(\dfrac{\partial u_3}{\partial X_i}\right)^2\right] & \text{if } i = j \\ \dfrac{1}{2}\left(\dfrac{\partial u_i}{\partial X_j} + \dfrac{\partial u_j}{\partial X_i}\right) + \dfrac{1}{2}\left[\dfrac{\partial u_1}{\partial X_i}\dfrac{\partial u_1}{\partial X_j} + \dfrac{\partial u_2}{\partial X_i}\dfrac{\partial u_2}{\partial X_j} + \dfrac{\partial u_3}{\partial X_i}\dfrac{\partial u_3}{\partial X_j}\right] & \text{if } i \neq j. \end{cases} \tag{3.20.}$$

The parts in the square brackets represent the non-linear portions of the expression. If neglected, (3.20.) comes down to *infinitesimal strain* as in standard linear elasticity. In other words, for infinitesimal small strains, for which the reference and current configurations almost coincide, the GL strain tensor is reduced to the engineering strain definition.

By rewriting (3.18.) it becomes clear that the GL is a symmetric second order tensor immune to rigid body rotation:

$$\boldsymbol{\varepsilon} = \frac{1}{2}\left(\mathbf{F}^{\mathrm{T}}\mathbf{F} - \mathbf{I}\right) = \frac{1}{2}\left(\mathbf{U}\mathbf{R}^{\mathrm{T}}\mathbf{R}\mathbf{U} - \mathbf{I}\right) = \frac{1}{2}\left(\mathbf{U}^2 - \mathbf{I}\right). \tag{3.21.}$$

As was already pointed out the appropriate stress measure to use with the GL strain tensor is the second Piola-Kirchhoff stress tensor. It should be noted that the PK2 stresses have little physical meaning, and they should be transformed to Cauchy stress for practical purposes. Cauchy stress $\boldsymbol{\sigma}$ reflects what is actually happening in the material, so it is usually called the *true* stress. Namely, Cauchy stress relates the actual physical force per unit area in the current configuration with the surface area in the current configuration.

If we relate the actual physical force per unit area in the current configuration with the surface area in the reference configuration we get the first Piola-Kirchoff stress tensor $\mathbf{P}$, usually abbreviated as PK1. This tensor is asymmetric and is related to the Cauchy stress tensor as:

$$\mathbf{P} = J\boldsymbol{\sigma}\mathbf{F}^{-\mathrm{T}} \quad \text{and} \quad \boldsymbol{\sigma} = J^{-1}\mathbf{P}\mathbf{F}^{\mathrm{T}}. \tag{3.22.}$$

The second Piola-Kirchhoff stress tensor is symmetric and can be related to the first Piola-Kirchhoff stress and Cauchy stress as:

$$\begin{gathered} \mathbf{S} = J\mathbf{F}^{-1}\boldsymbol{\sigma}\mathbf{F}^{-\mathrm{T}} \quad \text{and} \quad \sigma = \frac{1}{J}\mathbf{F}\mathbf{S}\mathbf{F}^{\mathrm{T}}, \\ \mathbf{S} = \mathbf{F}^{-1}\mathbf{P} \quad \text{and} \quad \mathbf{P} = \mathbf{F}\mathbf{S}. \end{gathered} \tag{3.23.}$$

PK2 can be interpreted as the force per unit area in the reference configuration decomposed into the Lagrangian base vectors in the reference configuration. Alternatively, in

the Cartesian basis, can be interpreted as a fictional force (the force in the current configuration pulled back to the reference configuration via the inverse deformation gradient) per unit area in the reference configuration.

Another important stress measure (Bathe, 1996; Bažant et al., 2000) is the Cauchy stress tensor rotated back to the initial material coordinates, i.e. the corotational Cauchy stress or back-rotated Cauchy stress, here denoted as $\hat{\boldsymbol{\sigma}}$:

$$\hat{\boldsymbol{\sigma}} = \mathbf{R}^{\mathrm{T}} \boldsymbol{\sigma} \mathbf{R}. \tag{3.24.}$$

Both the Cauchy stress and the corotational Cauchy stress were used as needed in the stress analysis.

The finite element discretisation of the principle of virtual work given in (3.17.) results in a matrix equation in which the unknown displacement vector $\mathbf{u}$ is obtained explicitly from the known state position. Using Voigt notation, the dynamic equilibrium equation can be written as:

$$\mathbf{M}\, {}^{t}\ddot{\mathbf{u}} + \mathbf{C}\, {}^{t}\dot{\mathbf{u}} = {}^{t}\mathbf{R} - {}^{t}_{0}\mathbf{F} \tag{3.25.}$$

where $\mathbf{M}$ is the mass matrix, $\mathbf{C}$ is the damping matrix (proportional to $\mathbf{M}$), $\ddot{\mathbf{u}}$ and $\dot{\mathbf{u}}$ are vectors of nodal point accelerations and velocities, $\mathbf{R}$ is the vector of external force and $\mathbf{F}$ is the vector of internal force. To obtain computational efficiency, the mass matrix $\mathbf{M}$ is diagonalisated and the internal force vector $\mathbf{F}$ on element level is computed by stress integration as:

$${}^{t}_{0}\mathbf{F} = \int_{{}^{0}V} {}^{t}_{0}\mathbf{B}_{L}^{\mathrm{T}}\, {}^{t}_{0}\hat{\mathbf{S}}\, \mathrm{d}^{0}V, \tag{3.26.}$$

where ${}^{t}_{0}\mathbf{B}_{L}$ is linear strain–displacement matrix, ${}^{t}_{0}\hat{\mathbf{S}}$ is the vector form of PK2 and the integration is performed over the reference volume ${}^{0}V$. In Voigt notation the full forms of ${}^{t}_{0}\hat{\mathbf{S}}$ and ${}^{t}_{0}\mathbf{F}$ are:

$${}^{t}_{0}\hat{\mathbf{S}}^{\mathrm{T}} = \begin{bmatrix} S_{11} & S_{22} & S_{33} & S_{12} & S_{23} & S_{13} \end{bmatrix}, \tag{3.27.}$$

$${}^{t}_{0}\mathbf{F}^{\mathrm{T}} = \begin{bmatrix} F_1^1 & F_2^1 & F_3^1 & F_1^2 & F_2^2 & F_3^2 & \dots & F_1^n & F_2^n & F_3^n \end{bmatrix}, \tag{3.28.}$$

where the lower right index indicates the coordinate, the upper right index the node of the finite element, and n is the number of nodes per element. According to this notation the ${}^{t}_{0}\mathbf{B}_{L}$ has the following form:

$$\begin{bmatrix} l_{11}h_{1,1} & l_{21}h_{1,1} & l_{31}h_{1,1} & l_{11}h_{2,1} & \dots & l_{31}h_{n,1} \\ l_{12}h_{1,2} & l_{22}h_{1,2} & l_{32}h_{1,2} & l_{12}h_{2,2} & \dots & l_{32}h_{n,2} \\ l_{13}h_{1,3} & l_{23}h_{1,3} & l_{33}h_{1,3} & l_{13}h_{2,3} & \dots & l_{33}h_{n,3} \\ (l_{11}h_{1,2}+l_{12}h_{1,1}) & (l_{21}h_{1,2}+l_{22}h_{1,1}) & (l_{31}h_{1,2}+l_{32}h_{1,1}) & (l_{11}h_{2,2}+l_{12}h_{2,1}) & \dots & (l_{31}h_{n,2}+l_{32}h_{n,1}) \\ (l_{12}h_{1,3}+l_{13}h_{1,2}) & (l_{22}h_{1,3}+l_{23}h_{1,2}) & (l_{32}h_{1,3}+l_{33}h_{1,2}) & (l_{12}h_{2,3}+l_{13}h_{2,2}) & \dots & (l_{32}h_{n,3}+l_{33}h_{n,2}) \\ (l_{11}h_{1,3}+l_{13}h_{1,1}) & (l_{21}h_{1,3}+l_{23}h_{1,1}) & (l_{31}h_{1,3}+l_{33}h_{1,1}) & (l_{11}h_{2,3}+l_{13}h_{2,1}) & \dots & (l_{33}h_{n,3}+l_{33}h_{n,1}) \end{bmatrix} \tag{3.29.}$$

where $h_{i,j}$ are the shape function derivatives and l_{ij} are the components of the displacement gradient in material coordinates and are calculated as follows, see Equation (3.13.):

$$l_{ij} = \sum_{k=1}^{n} h_{k,j}\, {}^{t}u_i^k. \tag{3.30.}$$

Chapter 4.

Material non-linearity

In the first numerical study the structure (reinforced concrete frame) and the ground (rock masses) are analysed with appropriated constitutive models: microplane for the concrete and plasticity for the reinforcement and the ground. In the second numerical study, where the emphasis is on the SSI, the ground is modelled the same way but the structure is treated as linear elastic. Accordingly, this chapter gives a theoretical overview of these models along with different computational aspects and the numerical implementation.

4.1. Plasticity model

4.1.1. Stress-strain relations in plasticity

A yield criterion f is a hypothesis defining the limit of elasticity in a material and the onset of plastic deformation under any possible combination of stresses. In a 3D stress space (with orthogonal principal stress axes) the yield criterion can be expressed as a yield surface, or yield locus. Allowing for the possibility of a non-associative flow rule, plastic strain increment occur normal to a plastic potential g (Crisfield, 1991):

$$\dot{\boldsymbol{\varepsilon}}_p = \dot{\boldsymbol{\lambda}} \frac{\partial g}{\partial \boldsymbol{\sigma}} = \dot{\boldsymbol{\lambda}}\, \mathbf{b}, \tag{4.1.}$$

where $\mathbf{b}$ is the normal to the plastic potential surface (a column vector) and $\dot{\boldsymbol{\lambda}}$ is a positive constant usually referred to as the plastic strain-rate multiplier. The stress change is then related to the strain change by:

$$\dot{\boldsymbol{\sigma}} = \mathbf{D}_e(\dot{\boldsymbol{\varepsilon}}_t - \dot{\boldsymbol{\varepsilon}}_p) = \mathbf{D}_e(\dot{\boldsymbol{\varepsilon}}_t - \dot{\boldsymbol{\lambda}}\, \mathbf{b}), \tag{4.2.}$$

where $\dot{\boldsymbol{\varepsilon}}_t$ (or simply $\dot{\boldsymbol{\varepsilon}}$) is the total strain rate, $\dot{\boldsymbol{\varepsilon}}_p$ is the plastic strain rate, and assuming isotropic elasticity, $\mathbf{D}_e$ is the elastic stress-strain matrix:

$$\mathbf{D}_e = \frac{E(1-\nu)}{(1+\nu)(1-2\nu)} \begin{bmatrix} 1 & \frac{\nu}{1-\nu} & \frac{\nu}{1-\nu} & 0 & 0 & 0 \\ \frac{\nu}{1-\nu} & 1 & \frac{\nu}{1-\nu} & 0 & 0 & 0 \\ \frac{\nu}{1-\nu} & \frac{\nu}{1-\nu} & 1 & 0 & 0 & 0 \\ 0 & 0 & 0 & \frac{1-2\nu}{2(1-\nu)} & 0 & 0 \\ 0 & 0 & 0 & 0 & \frac{1-2\nu}{2(1-\nu)} & 0 \\ 0 & 0 & 0 & 0 & 0 & \frac{1-2\nu}{2(1-\nu)} \end{bmatrix}. \tag{4.3.}$$

For plastic flow to occur, the stresses must remain on the yield surface, consequently:

$$\dot{f} = \frac{\partial f}{\partial \boldsymbol{\sigma}}^{\mathrm{T}} \dot{\boldsymbol{\sigma}} = \mathbf{a}^{\mathrm{T}} \dot{\boldsymbol{\sigma}} = 0. \tag{4.4.}$$

Equation (4.4.) is illustrated in Figure 4.1.: for a plastic flow, vector $\mathbf{a}$ is normal to the yield surface while the stress change $\dot{\boldsymbol{\sigma}}$ is tangential to it.

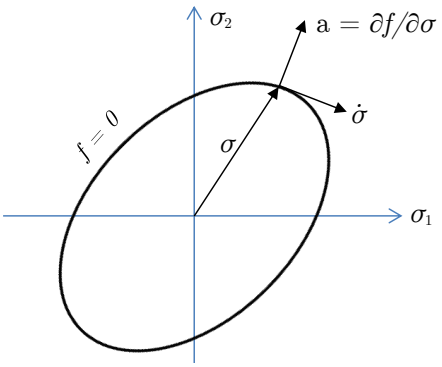

Figure 4.1.: The von Mises yield criterion expressed in terms of principal stress and plane stress conditions

The plastic strain-rate multiplier $\dot{\boldsymbol{\lambda}}$ can be obtained by pre-multiplying equation (4.1.) by the vector $\mathbf{a}^{\mathrm{T}}$ and then using it with (4.4.) :

$$\dot{\boldsymbol{\lambda}} = \frac{\mathbf{a}^{\mathrm{T}} \mathbf{D}_e \dot{\boldsymbol{\varepsilon}}}{\mathbf{a}^{\mathrm{T}} \mathbf{D}_e \mathbf{b}}. \tag{4.5.}$$

Substituting (4.5.) into (4.2.) finally gives:

$$\dot{\boldsymbol{\sigma}} = \left(\mathbf{D}_e - \frac{\mathbf{D}_e \mathbf{b} \mathbf{a}^{\mathrm{T}} \mathbf{D}_e}{\mathbf{a}^{\mathrm{T}} \mathbf{D}_e \mathbf{b}} \right) \dot{\boldsymbol{\varepsilon}}, \tag{4.6.}$$

where the second term in the brackets is the elasto-plastic stress-strain matrix $\mathbf{D}_{ep}$.

Note that the previous relations do not include hardening, i.e. they represent an elastic-perfectly plastic behaviour. Also, in the presented numerical studies associated flow rule

is assumed, i.e. the plastic potential function is set equal to the yield surface function ($f \equiv g$) and consequently $\mathbf{a} = \mathbf{b}$.

4.1.2. Modified Euler scheme with sub-stepping

The non-linear finite element analysis comes to the determination of the increment in stresses which is obtained by integrating the constitutive relations (see the rate form of the stres-strain relation (4.2.)). These integrating procedures are usually referred to as explicit or implicit.

In an implicit method the equations are solved at unknown stress states and consequently the solution is obtained in an iterative way. If a Newton-Raphson scheme is used for this task, the second derivates of the yield function and the plastic potential are needed. The most used implicit procedure is the backward Euler algorithm which can be summarised as follows: first, an elastic trial stress is computed using the tangent elastic or secant elastic moduli and then the trial stress is returned back to the yield surface by closest-point projection iteration. Although, this approach has many advantages, it has also one draw-back. Since it needs second derivates of the yield function and the plastic potential, its implementation can be very difficult for more complex plastic models.

In an explicit integration scheme, the yield surface and the required gradients are evaluated at known stress states which means that no iteration is strictly necessary (Sloan et al., 2001; Jeremić and Yang, 2002). However, it is usually prudent to introduce a simple iteration to correct the final stresses to the yield surface. Explicit schemes require only the first derivatives of the yield function and the plastic potential. That makes them more straightforward and easy to implement then the implicit schemes (Harewood and McHugh, 2007; Sloan et al., 2001). Their accuracy and efficiency can be significantly increased by introducing an automatic sub-incrementation and error control. Each increment is divided in a number of smaller increments and for each of them the exact equilibrium is ensured. This method gives much better result than satisfying the the equilibrium at the beginning of the increment and at the end only. In this procedure usually an linear strain path within an increment is assumed. Unlike implicit methods, explicit methods need to find the intermediate yield stress point when stress pass from an elastic to a plastic state.

The adopted scheme is based on the assumption that the rate of deformation tensor can be additively decomposed into an elastic part and a plastic part. An alternative assumption would be that the deformation gradient tensor can be multiplicatively decomposed in an elastic part and a plastic part. This assumption is based on an intermediate material configuration, which is obtained by a conceptual destressing of the currently deformed

configuration to zero stress. The presented modified forward Euler scheme with the additive decomposition of the rate of deformation has proven reliable for the given tasks while maintaining relative simplicity and efficiency (Sloan et al., 2001). Regarding the choice of strain and stress measures see an in-depth discussion in sections 3.2. and 4.2.2. It should be also noted that in the present study, due to the nature of the problem, no large deformations are expected.

► *Modified forward Euler algorithm for elasto-plastic models*

In this Thesis, integration of the rate form of the stress–strain relation is performed by an explicit integration scheme with automatic sub-stepping and error control based on the forward Euler algorithm (Sloan et al., 2001). The procedure will be presented as a series of computational steps in case of a conventional elasto-plastic model with a constant stress-strain matrix. All the quantities are denoted with a 0 or a 1 in their index representing the start or the end of an increment. Accordantly, for a imposed strain increment, the corresponding stress increment is computed by integrating the stres-strain relations over an pseudo-time interval $T = 0$ to $T = 1$. The yield condition for computational purposes is replaced by the approximation $f \leq |FTOL|$ where $FTOL$ is a small tolerance, typically in the range of 10^{-6} to 10^{-9}.

The stress associated with an imposed strain increment is calculated according the following steps. For the imposed strain increment, an elastic trial stress is computed. Accordantly, the stress increment can be (a) purely elastic, (b) purely plastic and (c) it undergoes a transition from elastic to plastic. In the latter case, a yield surface intersection point has to be found (assuming additive decomposition of the strain increment). Generally, an iterative procedure is started to locate the intersection point but for a conventional ideally elastoplastic model, the intersection point can be directly calculated without any iterations. After that, the plastic portion of the strain increment is automatically divided into a number of subincrements and the appropriate stress subincrements are computed. At the end of each subincrement, a correction of stresses to yield surface is performed to avoid the so-called yield surface drift (Crisfield, 1991, 1997; Sloan et al., 2001).

(1) Enter with the initial stress $\boldsymbol{\sigma}_0$ and the imposed strain increment $\Delta\boldsymbol{\varepsilon}$ for the current step.

(2) Compute the elastic stress increment $\Delta\boldsymbol{\sigma}_e$ and the trial elastic stress $\boldsymbol{\sigma}_e$ as:
$\Delta\boldsymbol{\sigma}_e = \mathbf{D}_e \Delta\boldsymbol{\varepsilon}$,
$\boldsymbol{\sigma}_e = \boldsymbol{\sigma}_0 + \Delta\boldsymbol{\sigma}_e$.

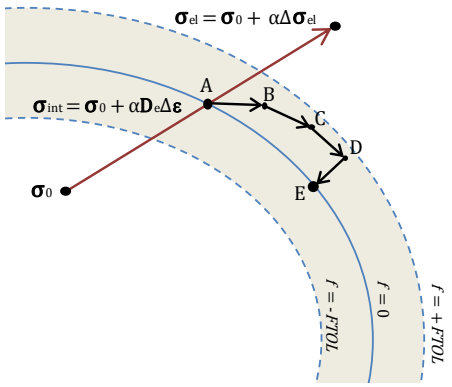

Figure 4.2.: Solution procedure: A - yield surface intersection, elastic to plastic transition; B, C and D - sub-increments; E - final solution obtained with correction from D.

If $f(\boldsymbol{\sigma}_e) \leq FTOL$ than the stress increment is purely elastic: set $\boldsymbol{\sigma}_1 = \boldsymbol{\sigma}_e$ and exit at the end of increment with $T = 1$.

(3) If $f(\boldsymbol{\sigma}_0) < -FTOL$ and $f(\boldsymbol{\sigma}_e) > FTOL$ then the stress undergoes a transition from elastic to plastic behaviour. Find the yield surface intersection point (see Figure (4.2.)), i.e. compute the portion of $\Delta\boldsymbol{\varepsilon}$ that corresponds to purely elastic deformation, α, using the Pegasus intersection scheme (see further in the text) and then go to step 5.

(4) If $f(\boldsymbol{\sigma}_0) \leq FTOL$ and $f(\boldsymbol{\sigma}_e) > FTOL$ then check for elasto-plastic unloading by computing:

$$\cos\Phi = \frac{\mathbf{a}^{\mathrm{T}} \Delta\boldsymbol{\sigma}_e}{\| \mathbf{a} \| \, \| \boldsymbol{\sigma}_e \|}, \text{where } \mathbf{a} \text{ is evaluated at } \boldsymbol{\sigma}_0.$$

> If $\cos\Phi \geq -LTOL$ then:
>
> The stress is purely plastic - set $\alpha = 0$.
>
> else
>
> Elastic unloading occurs followed by a plastic flow. Compute the portion of $\Delta\boldsymbol{\varepsilon}$ that corresponds to a purely elastic deformation, α, using the Pegasus intersection scheme for elasto-plastic unloading.

else:

The stress state is illegal because it lies outside the yield surface - exit with error.

(5) Update the stresses at the onset of plastic yielding as $\boldsymbol{\sigma}_0 \leftarrow \boldsymbol{\sigma}_0 + \alpha\Delta\boldsymbol{\sigma}_e$ and then compute the portion of $\Delta\boldsymbol{\sigma}_e$ that corresponds to plastic deformation according to $\Delta\boldsymbol{\sigma}_e \leftarrow (1 - \alpha)\Delta\boldsymbol{\sigma}_e$.

(6) Set $T = 0$ and $\Delta T = 1$.

(7) While $T < 1$, perform steps (8) to (15).

(8) Compute $\Delta\boldsymbol{\sigma}_i$ for $i = 1$ and 2 using:

$$\Delta\boldsymbol{\sigma}_i = \Delta T \Delta\boldsymbol{\sigma}_e - \Delta\lambda_i \mathbf{D}_e \mathbf{b}_i,$$

where

$$\Delta\lambda_i = \max\left(\frac{\Delta T \mathbf{a}_i^{\mathrm{T}} \Delta\boldsymbol{\sigma}_e}{\mathbf{a}_i^{\mathrm{T}} \mathbf{D}_e \mathbf{b}_i},\ 0\right), \quad \mathbf{a}_i = \left(\frac{\partial f}{\partial \boldsymbol{\sigma}}\right)_i, \quad \mathbf{b}_i = \left(\frac{\partial g}{\partial \boldsymbol{\sigma}}\right)_i,$$

are evaluated at $\bar{\boldsymbol{\sigma}}_i$, and

$$\bar{\boldsymbol{\sigma}}_1 = \boldsymbol{\sigma}_T, \quad \bar{\boldsymbol{\sigma}}_2 = \boldsymbol{\sigma}_T + \Delta\boldsymbol{\sigma}_1.$$

(9) Compute the new stresses and hold them in temporary storage according to:

$$\bar{\boldsymbol{\sigma}}_{T+\Delta T} = \boldsymbol{\sigma}_T + \tfrac{1}{2}(\Delta\boldsymbol{\sigma}_1 + \boldsymbol{\sigma}_2).$$

(10) Determine the relative error for the current substep from:

$$R_{T+\Delta T} = \frac{\parallel \Delta\boldsymbol{\sigma}_2 - \Delta\boldsymbol{\sigma}_1 \parallel}{2 \parallel \bar{\boldsymbol{\sigma}}_{T+\Delta T} \parallel}.$$

(11) If $R_{T+\Delta T} > STOL$ (where STOL is a specified tolerance) the substep is failed and a smaller pseudo time step needs to be found by extrapolation. First compute:

$$q = \max\left(0.9\sqrt{STOL/R_{T+\Delta t}}, 0.1\right),$$

and then set:

$$\Delta T \leftarrow \max\left(q\Delta T, \Delta T_{min}\right).$$

and then return to step (8).

(12) The substep is successful, so update the stress according to:

$$\boldsymbol{\sigma}_{T+\Delta T} = \bar{\boldsymbol{\sigma}}_{T+\Delta T}.$$

(13) If $|f(\boldsymbol{\sigma}_{T+\Delta T})| > FTOL$ then correct $\boldsymbol{\sigma}_{T+\Delta T}$ back to the yield surface using the correction algorithm.

(14) Extrapolate to obtain the size of the next sub-step by computing:

$$q = \max\left(0.9\sqrt{STOL/R_{T+\Delta t}}, 1.1\right).$$

If the previous step failed, limit the step size growth further by enforcing $q = \min(q, 1)$. Compute the new step size and update pseudo time according to:

$$T \leftarrow T + \Delta T, \quad \Delta T \leftarrow q\Delta T.$$

(15) Ensure the next time step size is not smaller than the minimum step size and check that integration does not proceed beyond $T = 1$ by setting:

$$\Delta T \leftarrow \max(\Delta T, \Delta T_{min}) \text{ and then } \Delta T \leftarrow \min(\Delta T, 1 - \Delta T).$$

(16) Exit with stress $\boldsymbol{\sigma}_1$ at the end of increment with $T = 1$.

▶ *Pegasus intersection scheme*

The Pegasus procedure of Dowell and Jarratt (1972) is a very efficient way of finding the intersection needed in step (3) of the modified Euler forward algorithm. The procedure goes as follows.

(1) Enter with the initial stress $\boldsymbol{\sigma}_0$, the strain increment $\Delta\boldsymbol{\varepsilon}$, initial values of $\alpha_0 = 0$ and $\alpha_1 = 1$ bounding the intersection with the yield surface, and the maximum number of iterations $MAXITS = 10$.

(2) Calculate: $\Delta\boldsymbol{\sigma}_e = \mathbf{D}_e\Delta\boldsymbol{\varepsilon}$.

(3) Set $F_0 = f(\boldsymbol{\sigma}_0 + \alpha_0\Delta\boldsymbol{\sigma}_e)$ and $F_1 = f(\boldsymbol{\sigma}_0 + \alpha_1\Delta\boldsymbol{\sigma}_e)$.

(4) Perform steps (5) to (8) a $MAXITS$ number of times

(5) Calculate:

$$\alpha = \alpha_1 - F_1(\alpha_1 - \alpha_0)/(F_1 - F_0),$$
$$F_{new} = f(\boldsymbol{\sigma}_0 + \alpha\Delta\boldsymbol{\sigma}_e)$$

(6) If $|F_{new}| \leq FTOL$ go to step (10).

(7) If F_{new} is of opposite sign to F_0 then:

set $\alpha_1 = \alpha_0$ and $F_1 = F_0$,

else

set $F_1 = F_1F_0/(F_0 + F_{new})$.

(8) Set $\alpha_0 = \alpha$ and $F_0 = F_{new}$.

(9) If convergence is not achieved after $MAXITS$ number of iterations, exit with error message.

(10) Exit with α.

▶ *Correction of stresses to yield surface*

It is possible that, at the end of an increment, the stress diverge from the yield surface. This violation of the yield condition is commonly referred to as *yield surface drift*. The amount of drift depends on the accuracy of the explicit integration scheme and the non-linearity of the constitutive relations. Sub-incrementation can significantly reduce the

dirft. Nevertheless, Crisfield (1991) recommends to introduce some form of stress correction as the effects of drift are cumulative and possibly can heavily affect the solution. At the end of each sub-increment the following procedure is called. First, the correction is attempted by the so called *consistent return scheme*. In rare cases when it fails, the correction is performed by the correction normal to the yield surface which, although is less accurate, is very robust.

(1) Enter with uncorrected stress σ_0.

(2) Perform steps (3) to (4) $MAXITS$ times (typically five to ten).

(3) Compute:

$$\delta\lambda = f_0/(\mathbf{a}_0^{\mathrm{T}}\mathbf{D}_e\mathbf{b}_0),$$

and then correct the stress using:

$$\boldsymbol{\sigma} = \boldsymbol{\sigma}_0 - \delta\lambda\mathbf{D}_e\mathbf{a}_0.$$

(4) If $|f(\boldsymbol{\sigma})| > |f(\boldsymbol{\sigma}_0)|$, then abandon previous correction, and correct the stress normal to the yield surface by computing:

$$\delta\lambda = f_0/(\mathbf{a}_0^{\mathrm{T}}\mathbf{a}_0),$$
$$\boldsymbol{\sigma} = \boldsymbol{\sigma}_0 - \delta\lambda\mathbf{a}_0.$$

(5) If $|f(\boldsymbol{\sigma})| \leq FTOL$, then go to step (8).

(6) Set $\sigma_0 = \sigma$.

(7) If convergence is not achieved after $MAXITS$ steps, print error message and exit.

(8) Exit with stress $\boldsymbol{\sigma}$ on the yield surface.

The applied solution procedures provides an effective way of integrating a wide range of elastoplastic constitutive laws: Tresca, Mohr-Coulomb, modified Cam clay, generalised Cam clay and many others complex model (Sheng et al., 2000; Zhao et al., 2005). Additionally, it fits very well with the adopted explicit time integration scheme. For the purposes of this Thesis two yielding criteria were used: the von Mises yield criterion (for the steel reinforcement) and the Drucker-Prager yield criterion (for the ground material).

4.1.3. The von Mises yield criterion

The von Mises yield criterion states that the yielding of a material begins when the second deviatoric stress invariant J_2 reaches a critical value and prior to yield, material

response is assumed to be elastic. Mathematically it can be expressed as (Crisfield, 1991):

$$f_{vm} = \sqrt{3J_2} - \sigma_0, \tag{4.7.}$$

where σ_0 is the yield strength of the material in case of simple tension and $\sigma_e = \sqrt{3J_2}$ is the effective stress (or von Mises stress).

The von Mises yield criterion is independent of the first stress invariant I_1, i.e. the onset of yielding does not depend on the hydrostatic component of the stress tensor. Sometimes this criterion is referred to as J_2 plasticity. Equation (4.7.) can be expanded in terms of the Cauchy stress tensor components as:

$$f_{vm} = \frac{1}{\sqrt{2}}\sqrt{(\sigma_x - \sigma_y)^2 + (\sigma_y - \sigma_z)^2 + (\sigma_z - \sigma_x)^2 + 6\tau_{xy}^2 + 6\tau_{yz}^2 + 6\tau_{zx}^2} - \sigma_0^2 \tag{4.8.}$$

or in principal stress as:

$$f_{vm} = \frac{1}{\sqrt{2}}\sqrt{(\sigma_1 - \sigma_2)^2 + (\sigma_2 - \sigma_3)^2 + (\sigma_3 - \sigma_1)^2} - \sigma_0^2. \tag{4.9.}$$

In the three-dimensional space the above equation represent a circular cylinder with the radius of $R = \sqrt{\frac{2}{3}}\sigma_0$ around the hydrostatic axis $\sigma_1 = \sigma_2 = \sigma_3$ (see Figure 4.3.a).

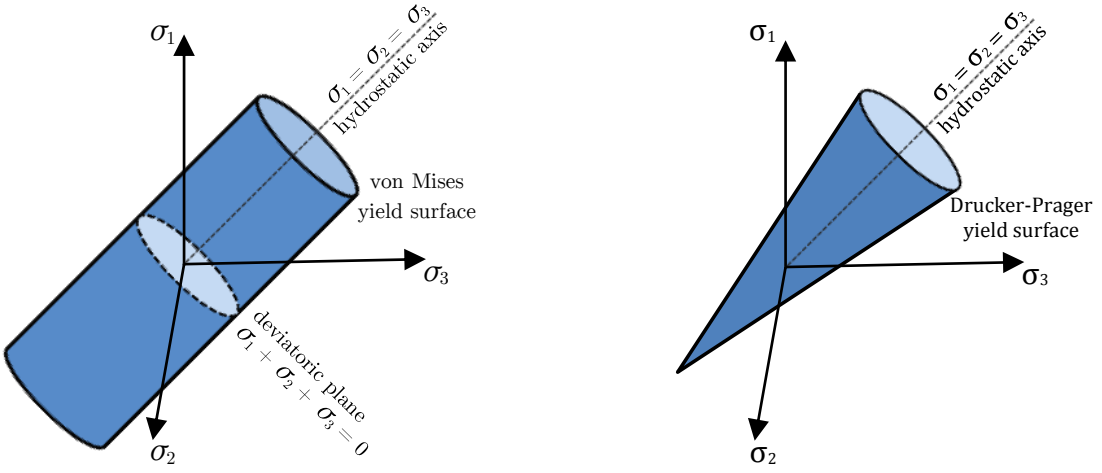

(a) The von Mises yield criterion

(b) The Drucker-Prager yield criterion

Figure 4.3.: Yield surfaces in principal stresses.

Differentiating equation (4.8.) gives:

$$\mathbf{a} = \frac{\partial f}{\partial \boldsymbol{\sigma}} = \frac{1}{2\sigma_e} \begin{bmatrix} 2\sigma_x - \sigma_y - \sigma_z \\ 2\sigma_y - \sigma_x - \sigma_z \\ 2\sigma_z - \sigma_x - \sigma_y \\ 6\tau_{xy} \\ 6\tau_{yz} \\ 6\tau_{zx} \end{bmatrix}. \tag{4.10.}$$

An illustration of von Mises yield criterion is given in Figure (4.4.) which shows the process of a plastic hinge formation in a cantilever beam. As was previously noted, the von Mises criterion is independent of the first stress invariant, i.e. the plastification proceeds equally on both the compressive and the tensile side.

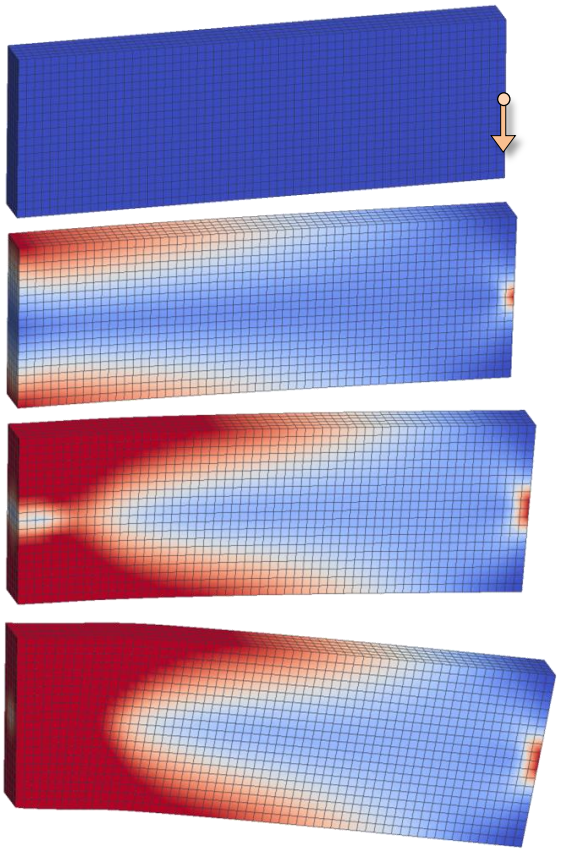

Figure 4.4.: Forming of a plastic hinge in a cantilever beam using the von Mises yield criterion.

4.1.4. The Drucker-Prager yield criterion

The criterion proposed by Drucker and Prager (1952) is a smooth aproximation to the Mohr-Coulomb law. It can be regarded as a modification od the von Mises criterion in

which an extra term is included to introduce pressure sensitivity. The criterion states that the plastic yielding begins when the second invariant of the deviatoric stress and the hydrostatic pressure reach a critical combination (Crisfield, 1991):

$$f_{dp} = \sqrt{J2} - \alpha I_1 - k, \tag{4.11.}$$

where α and k are material parameters. In the principal stress state, the locus of this criterion is a circural cone whose axis is the hydrostatic line (see Figure 4.3.b). For $\alpha = 0$ it becomes the von Mises criterion.

Since the rock mass and soil parameters are often given in terms of Mohr-Coulomb parameters, i.e. cohesion c and friction angle ϕ, it is convenient to relate these parameters to the Drucker parameters α and k. If the Drucker-Prager yield surface circumscribes the Mohr–Coulomb yield surface then the expressions for α and k are:

$$k = \frac{6\, c\, cos\phi}{\sqrt{3}\,(3 + sin\phi)}, \qquad \alpha = \frac{2\, sin\phi}{\sqrt{3}\,(3 + sin\phi)}, \tag{4.12.}$$

or if Drucker-Prager yield surface inscribes the Mohr–Coulomb yield surface:

$$k = \frac{6\, c\, cos\phi}{\sqrt{3}\,(3 - sin\phi)}, \qquad \alpha = \frac{2\, sin\phi}{\sqrt{3}\,(3 - sin\phi)}. \tag{4.13.}$$

These parameters can be also expressed in terms of yield stresses in uni-axial tension σ_t and compression σ_c :

$$\alpha = \frac{1}{\sqrt{3}} \frac{f_t - f_c}{f_t + f_c}, \qquad k = \frac{2}{\sqrt{3}} \frac{f_t \cdot f_c}{f_t + f_c}, \tag{4.14.}$$

Again, if the values of σ_t and σ_c coincide, the Drucker-Prager yield criterion comes down to the von Mises yield criterion. The normal to the yield surface can be obtained by differentiating (4.11.):

$$\mathbf{a} = \frac{\partial f}{\partial \boldsymbol{\sigma}} = \frac{1}{6\sqrt{J_2}} \begin{bmatrix} 6\alpha\sqrt{J_2} + (2\sigma_x - \sigma_y - \sigma_z) \\ 6\alpha\sqrt{J_2} + (2\sigma_y - \sigma_x - \sigma_z) \\ 6\alpha\sqrt{J_2} + (2\sigma_z - \sigma_x - \sigma_y) \\ 6\tau_{xy} \\ 6\tau_{yz} \\ 6\tau_{zx} \end{bmatrix}. \tag{4.15.}$$

An illustration of the Drucker-Prager yield criterion is given in Figure (4.5.) which shows a slope failure induced by a monotonically increasing vertical load at the top of the slope.

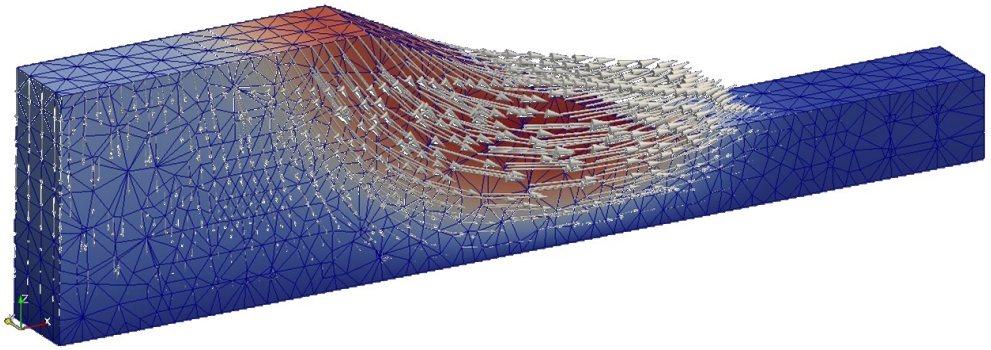

Figure 4.5.: Modelling of a slope failure using the Drucker-Prager yield criterion.

4.2. Microplane model

4.2.1. Introduction

Concrete is a composite material made of aggregate interconnected by a cement matrix. By its mechanical behaviour, concrete falls into the group of quasi-brittle materials. This phenomenological macro-scale observation is the result of micro-structural phenomena such as cohesion, friction and aggregate interlocking. Accordingly, the modelling of concrete can be approached by describing the stress-strain relations at the microlevel (microscopic models) or by considering the material behaviour as an average response of a complex micro-structural stress transfer mechanisms (macroscopic models). Although the microscopic approach is more accurate, for practical purposes only the macroscopic models are a viable option.

In the microplane model, the material is characterized by stress-strain relation on planes of various orientations. These planes can be regarded as damage or weak planes in the micro-structure, such as contact layers between aggregate pieces in the concrete. In an actual FE analysis the macro-micro transitions of mechanical properties are carried out by projecting the macroscopic values onto the tangential planes of a unit sphere imagined at every FE Gauss point. For computational purposes, the ideal surface of the sphere is replaced by a discrete geometrical approximation. To preserve an accurate description of the model while maintaining computational efficiency Bažant and Oh (1986) proposed two 21-integration points formulae which are implemented in the presented computer program (see Figure (4.6.)). The 21 integration points approximate one symmetric half of the sphere.

The main advantage of this model is its conceptual simplicity: only a set of uniaxial stress-strain curves on the microplane level need to be defined and the macroscopic model response comes automatically out as a result of the numerical integration over a number

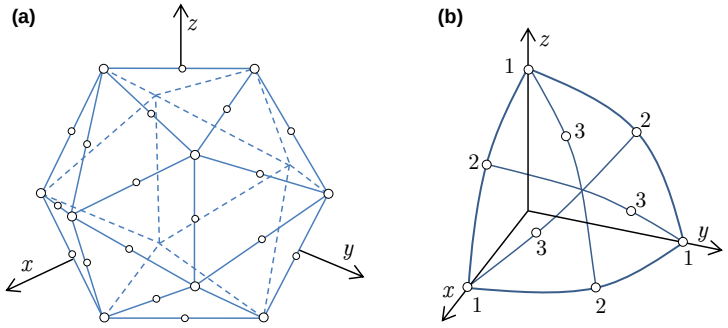

Figure 4.6.: Spatial discretisation of the surface of the sphere by 21 integration points: (a) 9th degree without fully symmetric formula and, (b) 9th degree with fully symmetric formula.

of microplanes. Furthermore, the tensorial invariance restrictions need not be directly enforced. They are automatically satisfied by superimposing, in a suitable manner, the responses from all microplanes. The model is suitable for full three-dimensional analysis and a number of numerical studies proved the model's capabilities in realistic prediction of concrete behaviour (Bažant and Prat, 1988; Bazant et al., 1996a,b; Bažant and Ožbolt, 1990; Bazant et al., 2000; Caner and Bazant, 2000).

4.2.2. Microplane model with relaxed kinematic constraint

In the early phase of the theory development it was assumed that the stress vector acting on microplanes with different orientations is the projection of the macroscopic stress tensor integrated at the gauss points. Later on, it was realised that that in order to obtain the unique solution for softening, the static constraint should be replaced with the *kinematic constraint* in which the microplane strain components are projections of the macroscopic strain tensor. The model used in this Thesis is a modification of the M2 model (Bažant and Prat, 1988; Ožbolt and Bažant, 1992, 1996) and based on the *relaxed kinematic constraint principle* (Ožbolt et al., 2001). It is aimed to be used for three-dimensional damage and fracture analysis of concrete and reinforced concrete structures in the framework of smeared crack approach. The main assumptions, theory and features of the model are hereafter presented.

Microplane coordinate system

The microplanes are tangential planes on the unit micro-sphere defined by outward normal vectors:

$$\mathbf{n} = \{n_1, n_2, n_3\}. \tag{4.16.}$$

The related microplane tangential unit vectors $\mathbf{m}$ and $\mathbf{k}$:

$$\mathbf{m} = \{m_1, m_2, m_3\}, \quad \mathbf{k} = \{k_1, k_2, k_3\}, \tag{4.17.}$$

are chosen in such a way to form a local coordinate system for each microplane, i.e. $\mathbf{k} \times \mathbf{m} = \mathbf{n}$ (see figure 4.7.).

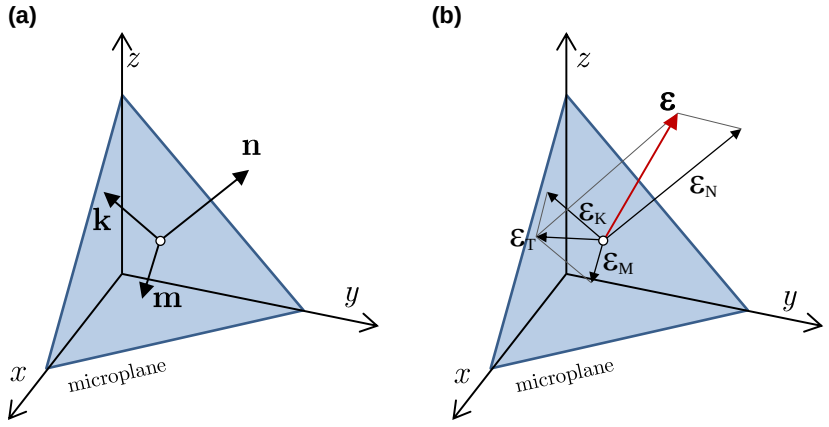

Figure 4.7.: Representation of a single microplane: (a) microplane unit vectors and, (b) decomposition of the total macroscopic strain tensor on the microplane.

Microplane strain components

According to the kinematic constraint principle the strain vector $\mathbf{e}_N$ on a particular microplane can be calculated from the macroscopic tensor $\boldsymbol{\varepsilon}$ as (Bazant and Gambarova, 1984):

$$\varepsilon_{N_i} = \varepsilon_{ij} n_j. \tag{4.18.}$$

The equation above is given in indicial notation where the lower-case indices refer to the components in Cartesian coordinates x_i, $i = 1, 2, 3$. The normal strain on the microplane is then:

$$\varepsilon_N = n_i \varepsilon_{N_i}. \tag{4.19.}$$

By substituting (4.18.) into (4.19.) the microplane normal component e_N can be related to the macroscopic strain tensor $\boldsymbol{\varepsilon}$ through the projection tensor $\mathbf{N}$:

$$\varepsilon_N = N_{ij} \varepsilon_{ij}, \tag{4.20.}$$

where

$$N_{ij} = n_i n_j. \tag{4.21.}$$

The shear strains on each microplane are characterised by their components in directions defined by orthogonal unit vectors **m** and **k**, of components m_i and k_i, lying within the microplane. The directions of vectors **m** and **k** can chosen arbitrary, but to minimise the direction bias the vector **m** are alternatively chosen normal to axes x_1, x_2, x_3 and then **k** is determined as $\mathbf{m} \times \mathbf{n}$. The shear strain components in these directions are $e_M = m_i(\varepsilon_{ij} n_j)$ and $e_K = k_i(\varepsilon_{ij} n_j)$. Taking the advantage of the symmetric property of the tensor ε_{ij}:

$$e_M = M_{ij}\varepsilon_{ij}, \quad e_K = K_{ij}\varepsilon_{ij}, \tag{4.22.}$$

where the projecting tensors M_{ij} and K_{ij} are:

$$M_{ij} = (m_i n_j + m_j n_i)/2, \quad K_{ij} = (k_i n_j + k_j n_i)/2. \tag{4.23.}$$

Furthermore, the length of vector **n** can be decomposed as:

$$e_N = e_V + e_D \tag{4.24.}$$

where e_V is the volumetric part and e_D is the deviatoric part given by:

$$e_V = \frac{1}{3}\mathrm{Tr}(\boldsymbol{\varepsilon}); \quad e_D = e_N - e_V. \tag{4.25.}$$

The volumetric part e_V does not depend on the microplane orientation, i.e. for a given Gauss point at which the macroscopic strain tensor $\boldsymbol{\varepsilon}$ is projected onto the corresponding microplanes, the volumetric strain components are equal and constant.

As was already stated, the present study uses the microplane model with relaxed kinematic constrain developed by Ožbolt et al. (2001). It was proposed as an extension of the kinematic constraint models by Bažant and Prat (1988) and by Ožbolt and Bažant (1992). The later introduced a general cyclic form with rate sensitivity and both models demonstrated their capabilities in realistic prediction of concrete behaviour. However, for dominant tensile damage, i.e. tensile softening, the models exhibit pathological behaviour which is manifested by unrealistic lateral expansion. In the framework of continuum mechanics, cracking is represented by the localisation of strains. In reality, material ruptures and the strain field experiences a discontinuous change. Perpendicularly to the discontinuity plane as well as in the three-dimensional space around it, the stress and strains relax (unload) proximately to zero (see Figure 4.8.).

In order to eliminate this pathological behaviour the so-called effective microplane strain components are adopted which account for the loss of continuity of the strain field for dominant tensile loads. Basically, instead of working with the microplane strain calculated from the total strain tensor (continuous strain field, see (4.21.) and (4.22.)),

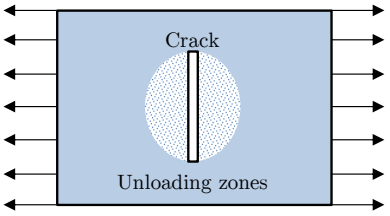

Figure 4.8.: Material loading zones around the crack surface.

the microplane stress is calculated from the effective microplane strain. Except for the volumetric strain, the effective microplane strains are resolved components of the total macroscopic strain tensor ε_{ij} multiplied by function ψ:

$$\begin{aligned} e_V &= \varepsilon_{kk}/3, \qquad & e_D &= (N_{ij}\varepsilon_{ij} - e_V)\psi, \\ e_M &= M_{ij}\varepsilon_{ij}\psi, \qquad & e_K &= K_{ij}\varepsilon_{ij}\psi. \end{aligned} \tag{4.26.}$$

For dominant tensile loads, ψ introduced in (4.26.) relaxes the kinematic constraint. Since it reflects discontinuity as a consequence of discrete tensile cracking, it is know as the *discontinuity function.* For each individual microplane it is decided weather the function applies or not and is related to the volumetric stress-strain relationship. At the onset of cracking (localisation od strain), the microplane perpendicular to to the crack surface has negative deviatoric strain ($e_D = e_N - e_V$; $e_N \to 0$ and $e_D < 0$), i.e the plane need to be unloaded or relaxed. On the contrary, the microplane parallel to the crack surface, has positive deviatoric strain ($e_D = e_N - e_V$; $e_N > e_V$; $e_N > 0 \to e_D > 0$) and it is loaded in tension. The total strain for individual deviatoric and shear components is then multiplied by the discontinuity function depending on weather the microplane is loaded or unloaded.

To account for the above effects the discontinuity function takes the form depending on the strain in question. For the deviatoric strain the discontinuity function is determined as:

$$\begin{aligned} e_D < 0, \quad e_V > 0, \quad \sigma_I > \sigma_{I,min} \quad &\to \quad \psi = \mathrm{e}^{-|f(\sigma_I)e_V/e_1|^m}, \\ e_D \geqslant 0 \quad &\to \quad \psi = 1, \end{aligned} \tag{4.27.}$$

where e_1 is an empirical factor (see further in text), $\sigma_{I,min}$ is a small limit value of the maximum principal stress, and $f(\sigma_I)$ is a function introduced to assure a smooth transition from a discontinuous state (crack) into a continuous state (crack closure and

subsequently loading in compression), see Figure 4.9. This function is determined as:

$$\begin{aligned} \sigma_{I,min} \leqslant \sigma_I \leqslant 0 \quad &\rightarrow \quad f(\sigma_I) = 1 - \chi, \quad \chi = \sin\left(\frac{\pi}{2}\left|\frac{\sigma_I}{\sigma_{I,min}}\right|\right), \\ \sigma_I > 0 \quad &\rightarrow \quad f(\sigma_I) = 1, \\ \sigma_I < \sigma_{I,min} \quad &\rightarrow \quad f(\sigma_I) = 0. \end{aligned} \tag{4.28.}$$

The shear discontinuity function for individual microplanes is:

$$\begin{aligned} e_V > 0, \quad \sigma_I > \sigma_{I,min} \quad &\rightarrow \quad \psi = \mathrm{e}^{-|f(\sigma_I)e_V/e_1|^m}, \\ \text{else} \quad &\rightarrow \quad \psi = 1. \end{aligned} \tag{4.29.}$$

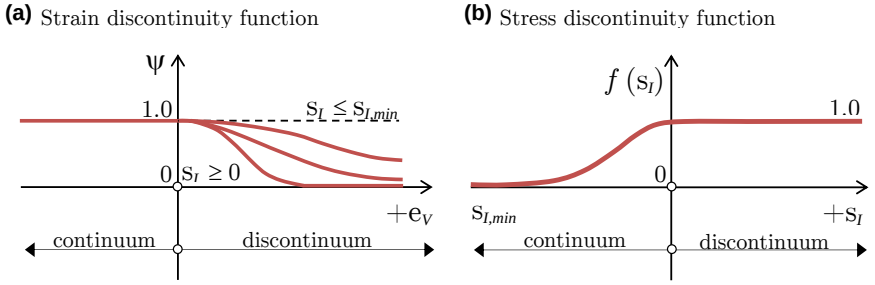

Figure 4.9.: Microplane discontinuity function: (a) strain and (b) stress discontinuity function.

Microplane stress components

Microplane stress increments are calculated from the respective known strain increments as:

$$\begin{aligned} \mathrm{d}s_V &= E_V \mathrm{d}e_V, \\ \mathrm{d}s_D &= E_D \mathrm{d}e_D, \\ \mathrm{d}s_M &= E_M \mathrm{d}e_M, \\ \mathrm{d}s_K &= E_K \mathrm{d}e_K, \end{aligned} \tag{4.30.}$$

where E_V, E_D, E_M and E_K represent tanget moduli obtained from known uni-axial microplane stress-strain relationships which are the same as those introduced by Ožbolt

and Bažant (1992) and are based on the scalar damage theory:

$$\begin{aligned} s_V &= C_V e_V, \\ s_D &= C_D e_D, \\ s_M &= C_M e_M, \\ s_K &= C_K e_K, \end{aligned} \tag{4.31.}$$

with (expect for volumetric compression):

$$\begin{aligned} C_V &= E_{V,0}(1-\omega_V), \\ C_D &= E_{D,0}(1-\omega_D), \\ C_T &= E_{T,0}(1-\omega_T), \end{aligned} \tag{4.32.}$$

where C_V, C_D and C_T are the secant moduli with their initial values equals to the respectiv tangent moduli. The shear microplane moduli C_T represents both components M and K. The scalar damage parameters ω are defined as:

$$\begin{aligned} \omega_V &= 1 - \mathrm{e}^{-|e_V/e_1|^m} \quad \text{for} \quad e_V \geq 0, \\ \omega_D &= 1 - \mathrm{e}^{-|e_D/e_1|^m} \quad \text{for} \quad e_V \geq 0, \\ \omega_D &= 1 - \mathrm{e}^{-|e_D/e_2|^n} \quad \text{for} \quad e_V < 0, \\ \omega_T &= 1 - \mathrm{e}^{-|e_T/e_5|^k}, \end{aligned} \tag{4.33.}$$

where parameters $e_1, e_2, e_3, e_4, m, n, k$ are empirical material constants. Parameter e_5 in equation (4.33.) is dependent on the volumetric strain e_V as: $e_5 = e_3$ if $e_V \geq 0$ and $e_5 = e_3 - e_4$ if $e_V < 0$. It reflects the internal friction which is an additional kinematic constraint. For volumetric compression, there is no damage ($\omega_V = 0$), so stress-strain relationship is adopted as:

$$C_V = E_{V,0}\left[\left(1 + \left|\frac{e_V}{a}\right|\right)^{-p} + \left|\frac{e_V}{a}\right|^q\right], \tag{4.34.}$$

where a, b, p, q are also empirical constants. The above equations are schematically plotted in Figure 4.10. Note that only the shear component is assumed to be symmetric.

Macroscopic stress tensor

After retrieving the microplane stress components, the macroscopic stress tensor σ_{ij} is obtained by integrating all the microplane stresses over all microplanes such that the stress equilibrium between all the microplane stresses and macroscopic stress tensor is approximately fulfilled. In total form, this equilibrium can be approximately be enforced

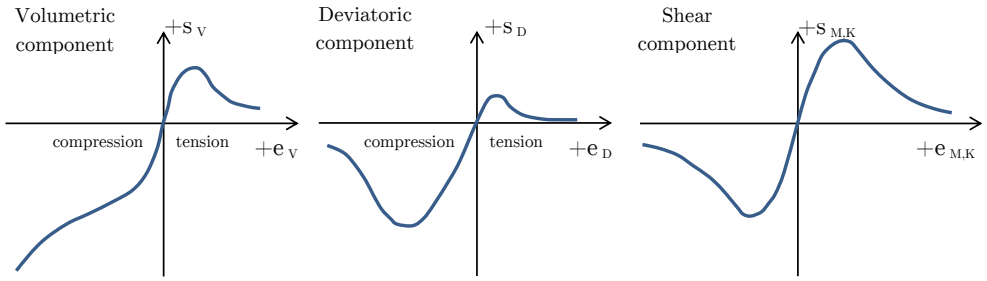

Figure 4.10.: Schematic representation of microplane stress-strains relationships for virgin load: volumetric V, deviatoric D and shear-stress components M and K.

by the virtual work equation as (Bažant and Prat, 1988):

$$\frac{2\pi}{3}\sigma_{ij}\delta\varepsilon_{ij} = \int_S \left(s_N\delta e_N + s_M\delta e_M + s_K\delta e_K\right)\Omega(\mathbf{n})\mathrm{d}S, \tag{4.35.}$$

where $\mathbf{n}$ represents unit vector normal to the microplanes and $\delta\varepsilon_{ij}, \delta e_N, \delta e_M, \delta e_K$ are small variations of the strains on the macro and micro levels. The left-hand size of equation (4.35.) is the macroscopic work done on the unit sphere while the right-hand side is the microscopic work done over the surface of the same sphere. Function $\Omega(\mathbf{n})$ is a weight function of the normal direction $\mathbf{n}$ that introduces anisotropy of the material in its initial state. For normal concrete $\Omega(\mathbf{n})$ is equal to 1, which implies initial isotropy. By substituting (4.20.) and (4.22.) into (4.35.) we get the macroscopic stress tensor as:

$$\sigma_{ij} = \frac{3}{2\pi}\int_S \left[n_i n_j s_V + n_i n_j s_D + \frac{1}{2}(m_i n_j + m_j n_i)\sigma_M \frac{1}{2}(k_i n_j + k_j n_i)\sigma_K\right]\Omega(\mathbf{n})\mathrm{d}S \tag{4.36.}$$

Carol and Bazant (1997) suggest that the term $n_i n_j \sigma_D$ in (4.36.) should be replaced by $(n_i n_j - \delta/3)s_D$. This integral is evaluated numerically employing the approximate formula:

$$\frac{4\pi}{3}\int_S \cong 6\sum_{\kappa=1}^{n} X_\kappa, \tag{4.37.}$$

in which subscript κ refers to a certain discrete set of microplanes characterised by spatial discretisation of their normals associated with points on a unit hemisphere, and X_κ are the weights of the directions, i.e. numerical integration coefficients.

The presented microplane model also includes rate sensitivity (Ožbolt et al., 2006; Ožbolt et al., 2014). The rate of deformation is measured at the macroscopic level, with the scalar quantity associated to the Green-Lagrange strain tensor leaving the micro stresses unaffected. However, when structural inertia forces govern structural response, the rate dependency at the constitutive level is not of special interest (Ožbolt et al., 2011; Travaš et al., 2009; Travaš, 2009).

Choice of stress and strain tensor for microplane model

As was already discussed, the conceptual simplicity of the microplane model comes from the fact that the normal and shear stress components on the microplanes are directly used to describe physical phenomena such as friction and strength or yield limit, as opposed to classical (macroscopic) constitutive equations expressed in terms of tensors and their invariants. However, in this approach it is necessary that the stress components on the microplanes characterize the true stress on planes of various orientations within the material. For large stretches the components of the second Piola-Kirchhoff stress tensor can differ considerably from the corresponding components of the Cauchy stress tensor. Therefore, for large strains, the Cauchy stress, which rapresents true stress, should be considered. Although the Cauchy stress tensor would give a clear physical meaning for the microplane stress components, it is not referred to the initial configuration of the material and is not conjugate to any Lagrangian finite strain tensor. Therefore, it cannot be used in a constitutive equation for a material such as concrete that has a memory of the initial state. An appropriate stress measure is then the Cauchy (true) stress tensor rotated back to the initial coordinates attached to the material also called back-rotated Cauchy stress or corotational Cauchy stress, see equation (3.24.).

The back-rotated Cauchy stress tensor coincide with the Cauchy stress tensor if there is no coordinate rotation, i.e. $\mathbf{R} = \mathbf{I}$. For non-zero rotations the component values get transformed while the physical meaning of stress remains the same. The hydrostatic pressure, which is important for pressure-sensitive materials such as concrete, soils and rocks, is given by $\mathrm{tr}\,\mathbf{S}$ which is true regardless of rotation because the trace of a tensor is an invariant.

Regarding the strain measure, the most appropriate choice is the Green-Lagrange strain tensor. The use of any other strain tensor would greatly complicate the formulation of a microplane constitutive model (Bažant et al., 2000). Consequently, it is reasonable to base the finite-strain microplane model on the Green-Lagrange strain tensor and the back-rotated Cauchy stress tensor.

The above is extensively discussed in Bažant et al. (2000) and the transformation between different stress measures are given in section 3.2. In this context, it should be noted that in the present studies the stretches are not large.

Cyclic loading

The present model include unloading, loading and cyclic loading for a general triaxial stress-strain state. For this purpose loading-unloading rules have to be added to each

uni-axial stress-strain microplane relationship.

Each microplane strain component has to be monitored for virgin loading which occurs if:

$$e\Delta e \geqslant \quad \text{and} \quad (e - e_{max})(e - e_{min}) \geqslant 0, \tag{4.38.}$$

where e_{max} and e_{min} are the maximum and minimum values of the effective microplane strain that have occurred so far. If these conditions were not met, unloading or reloading takes place. For cycling loading, as opposed to virgin loading, the stress-strain relations must be written in incremental form:

$$\mathrm{d}\sigma = E\mathrm{d}e, \tag{4.39.}$$

where E represents unloading-reloading tangent moduli which is given by:

$$\begin{aligned} E =& E_0\alpha + \sigma\left(\frac{1-\alpha}{e-e_1}\right), \\ & e_1 = e_p - \frac{s_p}{E_0} + \beta(e - e_p) \quad \text{if} \quad e > e_p, \\ & e_1 = 0 \quad \text{otherwise.} \end{aligned} \tag{4.40.}$$

where s_p and e_p denote the positive or negative peak stress and strain for each microplane component using values s_p^+, e_p^+ for positive and s_p^-, e_p^- for negative peaks. α and β are empirically chosen constants between 1 and 10 and E_0 is the initial elastic stiffness moduli for the corresponding microplane component. The loading-unloading rules are illustrated in Figure 4.11. In the compressive part the loading-unloading modulus is defined by the initial elastic modulus $E_{V,0}$ while for the tension part the loading-unloading modulus is controlled by Equation (4.40.). Typical load cycle for virgin loading in tension, unloading in compression and reloading in tension is O-P-A-B-C-D-A-B-E-F-O-A. Virgin loading in compression, unloading and loading in tension is O-A'-B'-D'-A' or O-A'-B'-D'-A' or O-A'-B'-O-P-A-B-E-F-O-A.

Smeared crack concept

The so called *smeared crack concept* is used for the description of cracking (Ožbolt and Bažant, 1996; Weihe et al., 1998). According to this concept, the cracking trajectories are represented by contours of principal tensile deformations with a threshold value set to the value of the reference deformation ε_r that causes the crack to open. According to the engineering definition od strain, ε_r is defined as:

$$\varepsilon_r = \frac{w_{cr}}{L_{min}} \tag{4.41.}$$

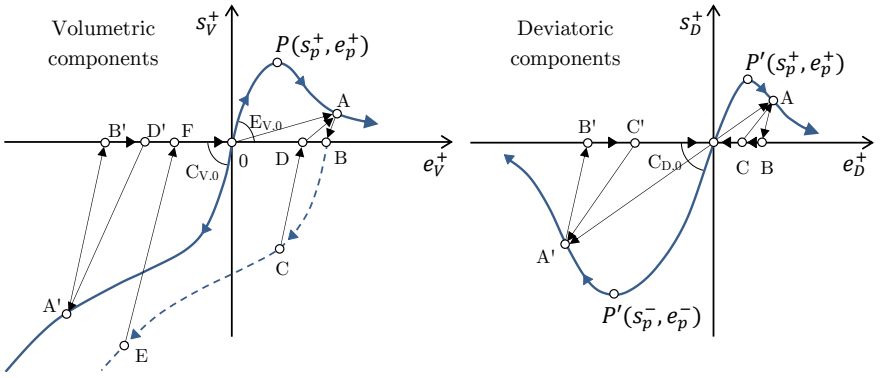

Figure 4.11.: Loading-unloading rules for volumetric and deviatoric microplane strain components.

where w_{cr} is the critical crack aperture depended on the type of concrete and L_{min} is the minimum finite element edge length. To obtain results that are objective with respect to element size, the crack band method is employed (Bažant and Oh, 1983; Ožbolt and Bažant, 1996).

An illustration of the smeared crack concept is given in Figures (4.12.) and (4.13.). In both examples the mesh continuity is preserved which satisfies the continuum mechanics assumptions. Figure 4.12. shows crack evolution in a concrete block by a controlled displacement as shown. Similarly, Figure 4.13. shows cracking of a reinforced concrete cantilever beam. The reinforcement bars are represented by rows of finite elements modelled according with theory of plasticity by adapting the von Mises yield criterion.

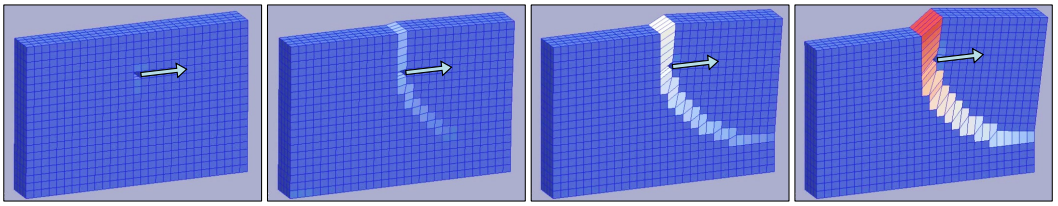

Figure 4.12.: Crack evolution in a concrete block.

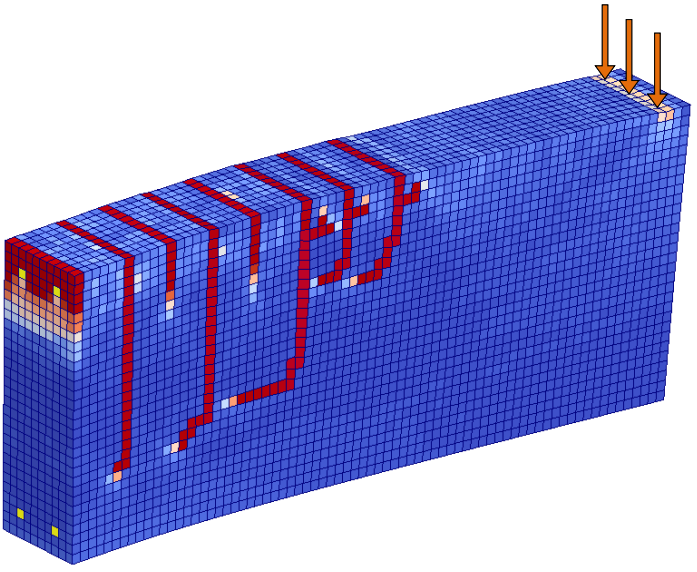

Figure 4.13.: Cracking of a reinforced concrete cantilever beam.

Chapter 5.

Contact non-linearity

The key point of the second numerical study is the modelling of the soil-foundation interface as a contact discontinuity with the aim to capture possible foundation sliding and/or uplifting during strong ground motion. Consequently, this chapter is dedicated to the theoretical preliminaries of contact mechanics and its numerical application.

5.1. Introduction

In order to be able to properly describe the contact between bodies (FE meshes) additional kinematic and kinetic conditions have to be set on the contact interface Γ_c (see Figure 5.1.). The kinematic condition assures that there is no penetrations between the body domains and the kinetic condition takes into account the physical behaviour at the contact interface. Accordingly, the contact problem (also known as the Signorini problem) can be formulated by adding these conditions to the differential equations governing continuum deformation. These additional boundary conditions can be stated as:

$$g_i \geqslant 0, \tag{5.1.a}$$

$$t_i \leqslant 0 \quad \text{on} \quad \Gamma_c, \tag{5.1.b}$$

$$g_i t_i = 0. \tag{5.1.c}$$

The first *impenetrability contact condition* (5.1.a) states that the gap value g has to be non-negative, i.e. contact events requires for $g_i = 0$, there is no contact for $g_i > 0$, and $g_i < 0$ represents an illegal state of penetration between the bodies. The second *intensility contact condition* (5.1.b) states that the normal traction t_i on Γ_c can be compressive only. Finally, the third *complementarity contact condition* or *unitary condition*(5.1.c) combine

the first and second condition in form of a product stating that if the gap value is positive than there is no contact forces, or if the gap value is positive than contact occurs with compressive traction t_i.

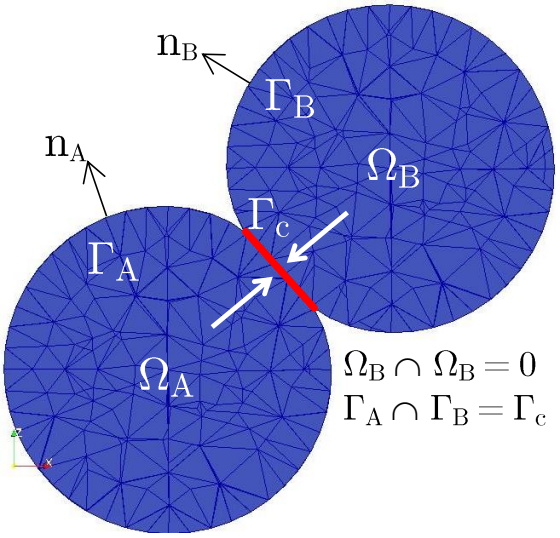

Figure 5.1.: Two bodies in contact: domains Ω_A and Ω_B, bounded by Γ_A and Γ_B with the contact surface Γ_c.

The non-linear nature of contact between deformable bodies requires an incremental solution (Carpenter et al., 1991; Anderheggen et al., 1993). In each time increment Δt contact simulation is performed in two computational stages. (1) Since the previously introduced equation of motion (see equation (2.30.)) can not recognise FE mesh boundary interactions, a new procedure has to be employed to monitor the deformation path and to notify if contact occurs. (2) After the localisation of the mesh regions in contact, forces on the interface have to be determined according to contact mechanics. The first stage which involves kinematic aspects is known as *contact detection stage* while the second which involves mechanical aspects is known as *contact resolution stage*. Both stages are covered in the following sections.

Only contact between two bodies (FE meshes) discretised with linear tetrahedrons will be considered here. For this purpose several terms will be introduced to simplify the description of the contact detection and resolution stage (see Figures 5.3. and 5.4.). It is common practice to name the two bodies in contact as *master* and *slave* and the related FE discretisations as *master* and *slave* discretisation. In this manner, nodes on the boundary of the slave FE mesh are called slave nodes, and nodes on the boundary of the master FE mesh are called master nodes. Master nodes belong to the boundary elements which are are all the elements which have at least one node on the boundary. Boundary surfaces, or master surfaces, are all triangles on the boundary of the master FE discretisation, i.e. they are formed by three master nodes belonging to a single boundary

element. The nodes involved in the contact form *contact elements*. They consist of one slave node, called *contractor node*, and the respective master surface, called *target surface*.

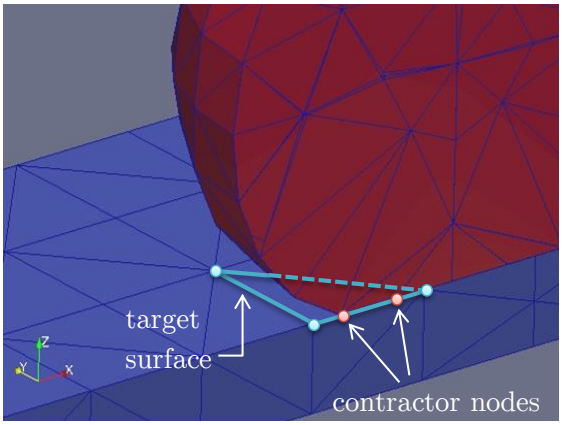

Figure 5.2.: Two bodies in contact (master body - blue and slave body - red) with an illustration of two contact elements (two contractor nodes shearing the same target surface).

The lists of boundary nodes, surfaces and elements have to be formed only once, before the start of the incremental analysis. Then, in each time step contact detection and contact resolution phase is performed with one body as the slave body and the other as the master body. After that, but before proceeding to the next time step, the master-slave associations are switched between the meshes and a second contact detection and contact resolution phase is performed. In order to maximise the computational efficiency, it is possible in some particular cases to omit the second contact analysis without affecting the accuracy and stability of the entire procedure.

5.2. Contact detection

The first part of the contact analysis is the contact detection stage which has the purpose to identify contact constraints violations and if so, form contact elements. It is split into the *global* and *local detection phase* (Carpenter et al., 1991; Heinstein et al., 1993). The global detection phase has the purpose to determine if any of the boundary nodes of the slave body penetrated into one of the boundary elements of the master body. This phase finishes with a list of these nodes called *contractor nodes*. Next, in the local detection phase, every contractor node has to be matched with the corresponding target surface, along with the time and position of their intersection. This forms the list of contact elements for the resolution phase.

5.2.1. Global detection

At the end of each time increment the mesh boundaries should be separated and thus fulfilling the impenetrability condition. However, at the beginning of the next time increment new incremental nodal displacement $\Delta\mathbf{u}$ are calculated according to the explicit time integration previously introduced. At this point it is possible that some of the boundary nodes found them selves in an non-physical position. These nodes are identified in the global detection stage by a performing a procedure based on the point in a polygon test.

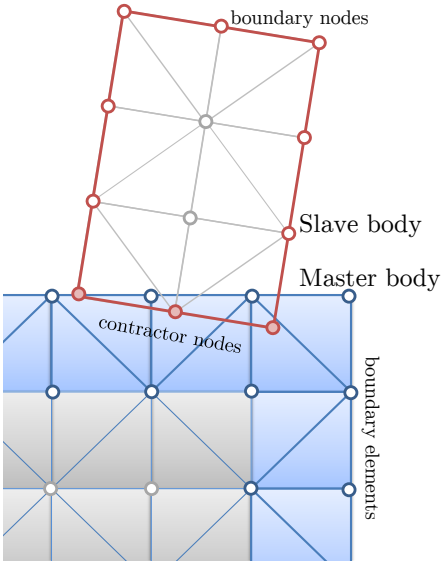

Figure 5.3.: Simplified 2D representation of a master and slave body with the respective boundary elements and nodes for contact analysis.

As was previously discussed, the barycentric coordinates ξ of a point P are positive if the point is inside the element domain (see Section 2.1.1.) and their sum is equal to 1. Based on this fact the global detection phase can be performed as follows. First, a computational loop is started over n_{bn} slave boundary nodes with coordinates (x^c, y^c, z^c) and then a second loop is started over n_{be} master boundary elements checking for penetration using equation (2.2.):

$$\begin{aligned} &\text{for} \quad node = 1, 2, ..., n_{bn} \\ &\text{for} \quad element = 1, 2, ..., n_{be} \\ \xi(x^c, y^c, z^c) =&(\alpha_i^{el} + x^c\beta_i^{el} + y^c\gamma_i^{el} + z^c\delta_i^{el}), \quad \text{for} \quad i = 1, 2, 3, 4, \end{aligned} \tag{5.2.}$$

where the coefficients $\alpha_i^{el}, \beta_i^{el}, \gamma_i^{el}$ and δ_i^{el} are given in equation (2.7.). If all the coordinates (volumes) are positive than the point will be inside the element domain indicating penetration.

The used strategy is very simple and robust, but also very expensive. To reduce the computational time the list of all possible contractor nodes should be reduced to region in which the contact is anticipated which is not always possible. Some of this aspects are discussed in the following chapter.

5.2.2. Local detection

After obtaining the list of contractor nodes in the global detection stage, the local detection stage is started. A detailed search is performed to find the matching target surface for each contractor node along with the position and time at which the contractor hit the target surface.

The position of contact is needed to distribute the magnitude of contact forces $\boldsymbol{\lambda}$ over the three target plane nodes of the corresponding surface of the 3D finite element and the contractor node that hit the plane. For this purpose the coordinates of contact are expressed in terms of element local coordinates ξ (Wriggers, 2002), see Figure 5.4. The corresponding unit vectors are $\mathbf{t}_1$ and $\mathbf{t}_2$ with the normal vector $\mathbf{n} = \mathbf{t_1} \times \mathbf{t_2}$. By knowing the coordinates of contact $\{\xi_1, \xi_2\}$, the force distribution is conducted by multiplying the contact force vector $\boldsymbol{\lambda}$ with the contact matrix $\mathbf{G}$ structured as:

$$\mathbf{G} = \begin{bmatrix} N_1(\xi) & 0 & 0 & N_2(\xi) & 0 & 0 & N_3(\xi) & 0 & 0 & -1 & 0 & 0 \\ 0 & N_1(\xi) & 0 & 0 & N_2(\xi) & 0 & 0 & N_3(\xi) & 0 & 0 & -1 & 0 \\ 0 & 0 & N_1(\xi) & 0 & 0 & N_2(\xi) & 0 & 0 & N_3(\xi) & 0 & 0 & -1 \end{bmatrix} \tag{5.3.}$$

in which $N(\xi)$ denotes the target plane node shape function. As can be noted, matrix (5.3.) implies force equilibrium by specifying that the sum of components in each row is equal to zero (since the sum of local coordinates is always 1). The problem is now reduced on identifying the coordinates of intersection $\{\xi_1, \xi_2\}$, i.e. on estimating the contact coordinates at which the contractor node hit the target plane.

The continuous collision detection strategy is invoked to obtain the local coordinates of intersection $\{\xi_1, \xi_2\}$ (Hutter and Fuhrmann, 2007). Particularly, for a given contractor node, the strategy establishes the time of contact t_c at which the node hit the target surface. The strategy is based on the geometrical and kinematical properties of nodes involved in contact. Particularly, by assuming that the nodal velocities $\mathbf{v}$ does not change between time level n and $n+1$, the strategy will reveal if and when the contractor node hits the candidate boundary surface. The idea is based on the fact that at the time of collision t_c, the four nodes are coplanar. Provot (1997) showed that for four points defined by the position vectors $\mathbf{x}_\mathrm{n}$ and constant velocities $\mathbf{v}_\mathrm{n}$, the time t_c at which the

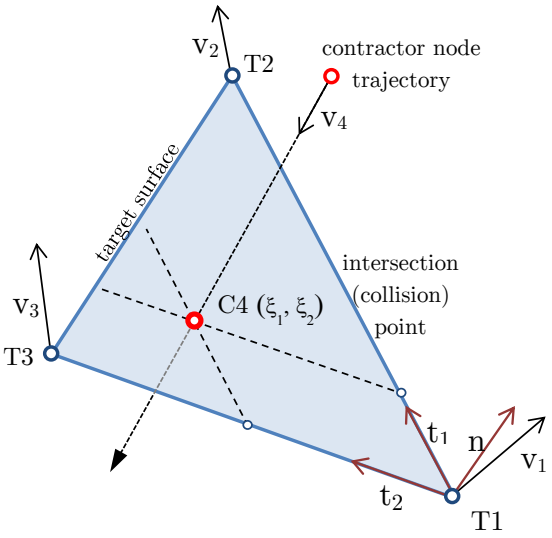

Figure 5.4.: Local detection of contact

points are coplanar satisfy the following:

$$(\mathbf{x}_{21} + t_c\mathbf{v}_{21}) \times (\mathbf{x}_{31} + t_c\mathbf{v}_{31}) \cdot (\mathbf{x}_{41} + t_c\mathbf{v}_{411}) = 0 \tag{5.4.}$$

where $\mathbf{x}_{ij} = \mathbf{x}_i - \mathbf{x}_j$ and $\mathbf{v}_{ij} = \mathbf{v}_i - \mathbf{v}_j$. Since the nodal coordinate vectors $\mathbf{x}_n$ and velocities $\mathbf{v}_n$ at a time t_n are known (reference frame), in order to solve equation (5.4.) the monomial form of the polynomial is needed. By extending the differences in equation (5.4.) and grouping the outcome by means of t_c, the solution is obtained by 188 additions and 192 multiplications. From the perspective of execution time, it is obvious that this computation requires considerable computational effort. However, the polynomial can be computed by only 50 additions and 48 multiplications, provided that the coefficients are grouped and rewritten as dot-products and cross-products (Hutter and Fuhrmann, 2007): $a_3 = \mathbf{v}_{21}\mathbf{v}_{31} \times \mathbf{v}_{41}$, $a_2 = \mathbf{x}_{21}\mathbf{v}_{31} \times \mathbf{v}_{41} - \mathbf{v}_{41}\mathbf{x}_{31} \times \mathbf{v}_{21} - \mathbf{v}_{21}\mathbf{x}_{41} \times \mathbf{v}_{31}$, $a_1 = \mathbf{v}_{41}\mathbf{x}_{21} \times \mathbf{x}_{31} - \mathbf{x}_{21}\mathbf{x}_{41} \times \mathbf{v}_{31} - \mathbf{v}_{21}\mathbf{x}_{21} \times \mathbf{v}_{41}$ and $a_0 = \mathbf{x}_{41}\mathbf{x}_{31} \times \mathbf{v}_{21}$. The time in which the points are coplanar represents the real roots of the cubic polynomial in time:

$$P(t_c) = a_3\, t_c^3 + a_2\, t_c^2 + a_1\, t_c + a_0 \tag{5.5.}$$

The time of collision is equal to the result with the lowest real value. This value must also be positive, and in the range of the adopted time increment. Otherwise, the procedure skips to the next candidate. If a legal value for the time of collision is found the corresponding position is calculated. Note that the local coordinates of intersection must be positive and in the range between 0 and 1, which assures that the contractor node is inside the target surface at the moment of impact.

Since a typical numerical analysis consists of a considerable number of small time increments, the robustness and efficiency of the local strategy is crucial for the analysis to be successful. A false detection, or no detection will likely result in a unrecoverable error. Serious difficulties in the computation of t_c can arise from the the fact that nodal movements can be in the order of magnitude as the computational round-off errors. For this purpose all the variables must be declared to be *double presision* (REAL 8) which increase the computational time.

Because of the difficulties discussed above, it is prudent to have an additional safety procedure which will be invoked only if the main strategy fails. This strategy is based on the idea that the volume of the element formed by the contractor node and the target surface has a non-positive value at the start of the increment, a non-negative value at the end of the increment, and exactly zero at the time of collision. The volume changes are linear so t_c can be easily computed. This procedure is simple and effective, but not so precise as the main procedure.

5.3. Contact resolution

To include the influence of contact forces between the FE meshes in the dynamic equilibrium equation (2.30.), the forward incremental Lagrangian multipliers method is used (Carpenter et al., 1991). In mathematical optimization problems, this method is used for fining local maxima and minima of a function subjected to equality constraints. Consider a two-dimensional optimisation problem presented in Figure 5.5.: maximise $f(x, y)$ subject to $g(x, y) = c$. For this purpose a new variable λ is introduced called a Lagrange multiplier. The Lagrange function is then defined by:

$$\Lambda(x, y, \lambda) = f(x, y) + \lambda(g(x, y) - c \tag{5.6.}$$

If $f(x_0, y_0)$ is a maximum of $f(x, y)$ for the constrained problem, then there exists λ_0 such that (x_0, y_0, λ_0) is a stationary point for the Langrange function, i.e. the partial derivatives of Λ are zero.

For the present contact analysis Lagrange multipliers $\boldsymbol{\lambda}$ represent contact forces with the constraint condition being the impenetrability condition. Accordantly, equation (2.30.) obtains the form:

$$\mathbf{M}\,\ddot{\mathbf{u}}_{\mathrm{n}} \;+\; \mathbf{C}\,\dot{\mathbf{u}}_{\mathrm{n}} \;+\; \mathbf{f}_{\mathrm{n}}^{\mathrm{int}} \;+\; \mathbf{G}_{\mathrm{n+1}}^{\mathrm{T}}\boldsymbol{\lambda}_{\mathrm{n}} \;=\; \mathbf{f}_{\mathrm{n}}^{\mathrm{ext}}, \tag{5.7.}$$

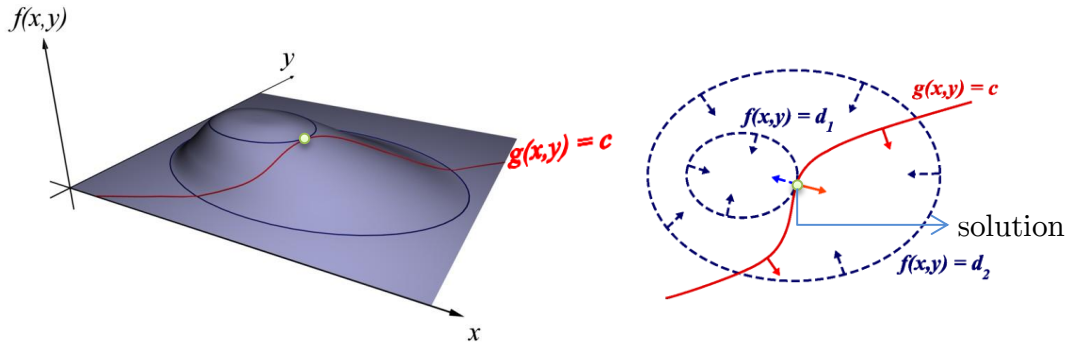

Figure 5.5.: Optimisation problem: find x and y to maximise $f(x, y)$ subject to a constraint $g(x, y)$

where the unknown displacement vector $\mathbf{u}$ in the time step $\mathrm{n}+1$ should meet the impenetrability condition given in the form:

$$\mathbf{G}_{\mathrm{n}+1}\left\{\mathbf{u}_{\mathrm{n}+1}-\mathbf{u}_{\mathrm{n}}+\mathbf{X}\right\}=0. \tag{5.8.}$$

By analysing equations (5.7.) and (5.8.) it can be seen that the Lagrange multipliers are calculated at n, while the displacement constraint is set at $n+1$. Hence the name *forward* Lagrange multiplier method.

As was previously discussed, the unknown displacement vector $\mathbf{u}$ in a time level $\mathrm{n}+1$ is obtained as follows. At the beginning of each time step it is assumed that there are no mechanical interactions between FE meshes in the reference configuration defined by coordinates vector $\mathbf{X}$. In other words, by temporarily ignoring the influence of contact, the computation start with the contact predictor stage where the nodal displacements are calculated with respect to the classical explicit update (2.34.). The computation proceeds with the global contact detection algorithm. For those nodes that violate the impenetrability condition and penetrate in a forbidden mesh domain, the local detection algorithm is activated. The algorithm localizes the position of contact ξ which is needed for assembling the contact matrix $\mathbf{G}_{\mathrm{n}+1}$ (5.3.). Once the contact detection procedures are executed, the correction of the previously calculated displacement field (2.34.) is performed by adding the contact displacement contribution. For this purpose, the contact forces $\boldsymbol{\lambda}_{\mathrm{n}}$ are determined according to:

$$\boldsymbol{\lambda}_{\mathrm{n}}=\left[\Delta t^{2}\,\mathbf{G}_{\mathrm{n}+1}\,\mathbf{M}^{-1}\,\mathbf{G}_{\mathrm{n}+1}^{\mathrm{T}}\right]^{-1}\,\mathbf{G}_{\mathrm{n}+1}\left\{\mathbf{u}_{\mathrm{n}+1}^{\mathrm{D}}-\mathbf{u}_{\mathrm{n}}+\mathbf{X}\right\}, \tag{5.9.}$$

where $\mathbf{u}_{n+1}^{D}$ is the displacement predictor calculated according to the standard explicit update (equation 2.34.) ignoring contact. In order to prevent non-physical penetration, the contact displacement vector $\mathbf{u}^{\mathrm{C}}$ is calculated by distributing the contact forces $\boldsymbol{\lambda}_{\mathrm{n}}$ among the nodes involved in contact. Depending on the position of contact ξ the contact

displacements $\mathbf{u}^{\mathrm{C}}$ at time level $\mathrm{n}+1$ are calculated as:

$$\mathbf{u}^{\mathrm{C}}_{\mathrm{n+1}} = -\Delta t^2\, \mathbf{M}^{-1}\, \mathbf{G}^{\mathrm{T}}_{\mathrm{n+1}}\, \boldsymbol{\lambda}_{\mathrm{n}}. \tag{5.10.}$$

At time level $\mathrm{n}+1$ the total nodal displacements $\mathbf{u}_{\mathrm{n+1}}$ are calculated as:

$$\mathbf{u}_{\mathrm{n+1}} = \mathbf{u}^{\mathrm{C}}_{\mathrm{n+1}} + \mathbf{u}^{\mathrm{D}}_{\mathrm{n+1}}. \tag{5.11.}$$

The briefly illustrated procedure can be very efficiently executed by Gauss-Seidel iteration strategy (Carpenter et al., 1991). During the Gauss-Seidel iterative procedure the coordinates of nodes in contact are progressively updated employing (5.11.). According to that, it has to be mention that there are situations in which the iterative procedure will put the contact node outside the penetrated domain. In that case, the next iteration loop will tends to pull back the node to the position of intersection, provoking tensile contact reaction. Obviously, this scenario cannot happen at the soil-structure interface and the node under consideration should be released from contact. It follows that the contact force components should be progressively monitored to include the nodal separation. For this purpose, note that $\boldsymbol{\lambda}$ in (5.9.) is given in respect to global coordinate system. In order to test the normal component λ_{N} for tension, $\boldsymbol{\lambda}$ should be transformed into local coordinates of the belonging contact surface. Since the contact surface is here always flat, the normal component λ_{N} can be defined as $(\boldsymbol{\lambda} \cdot \mathbf{n})\boldsymbol{\lambda}$ where $\mathbf{n}$ denotes the target plane normal vector. If the force λ_{N} denotes tension, the nodal separation is simply reproduced by setting λ_{N} equal to zero.

Apart the normal reaction force λ_{N}, the allowed limit of tangential component λ_{T} is also prescribed by the assumed frictional constitutive model. Particularly, the Coulomb frictional model is here employed to differentiate the stick from the slip contact condition. To perform the tangential check force limit, the force component λ_{T} should be obtained from $\boldsymbol{\lambda}$ and the related target surface vectors $\overline{\mathbf{a}}_{\alpha}$ and $\overline{\mathbf{a}}_{\beta}$. The computation involves basic vector algebra as $\lambda_{\mathrm{T}} = (\lambda\mathbf{m}) \cdot \mathbf{m} + (\lambda\mathbf{k}) \cdot \mathbf{k}$ where the projection vectors $\mathbf{m}$ is defined as (Wriggers, 2002):

$$\mathbf{m} = \frac{\overline{\mathbf{a}_{\alpha}}}{\|\overline{\mathbf{a}_{\alpha}}\|} \tag{5.12.}$$

and vector $\mathbf{k}$ is given by:

$$\mathbf{k} = \frac{\overline{\mathbf{a}_{\beta}} - (\overline{\mathbf{a}_{\beta}} \cdot \mathbf{m}) \cdot \mathbf{m}}{\|\overline{\mathbf{a}_{\beta}} - (\overline{\mathbf{a}_{\beta}} \cdot \mathbf{m}) \cdot \mathbf{m}\|} \tag{5.13.}$$

Once the force component λ_{T} is known the influence of friction can be quantified. In other words, after calculating the contact force vector $\boldsymbol{\lambda}$ the obtained force is decomposed into its normal λ_{N} and tangential part λ_{T}. The computation proceeds with checking the nodal tendency for contact separation (if $\|\lambda_{\mathrm{N}}\| > 0$ then $\lambda_{\mathrm{N}} = 0$) which is in accordance with the Coulomb frictional model where the tangential force λ_{T} depends on λ_{N}. It

is clear that if the node establishes tension load, further checking will not be required since the node will be released from the contact. On the other hand, if the tensile force is not present, the tangential force components have to be tested for eventual sliding contact condition. By computing the relative tangential displacement vector $\mathbf{g}_{\mathrm{T}}$, at the numerical implementation level the tangential force λ_{T} is subject to the condition (Ling and Stolarski, 1997; Wriggers, 2002):

$$\text{if} \quad \|\boldsymbol{\lambda}_{\mathrm{T}}\| > \mu\, \boldsymbol{\lambda}_{\mathrm{N}} \quad \text{then} \quad \boldsymbol{\lambda}_{\mathrm{T}} = -\mu\, \|\boldsymbol{\lambda}_{\mathrm{T}}\|\, \frac{\dot{\mathbf{g}}_{\mathrm{T}}}{\|\dot{\mathbf{g}}_{\mathrm{T}}\|}, \tag{5.14.}$$

in which μ is the friction coefficient defined by the static μ_{S} and dynamic friction coefficient μ_{D} through the function:

$$\mu(\dot{\mathbf{g}}_{\mathrm{T}}) = \mu_{\mathrm{D}} + (\mu_{\mathrm{S}} - \mu_{\mathrm{D}}) \exp(-c\, \|\dot{\mathbf{g}}_{\mathrm{T}}\|), \tag{5.15.}$$

in which c represents a parameter that defines how fast is the transition from μ_{S} to μ_{D}. The condition (5.14.) is activated for each contractor node after the computation step in equation (5.9.). Note that if the tangential force component λ_{T} has been modified (according to the assumed frictional constitutive description), a new respective contact force λ should be computed before moving onto the next iterative cycle.

Finally, it ought to be mentioned that during the Gauss-Seidel iteration cycles the components of the displacement constraint matrix $\mathbf{G}_{\mathrm{n+1}}$ (5.3.) are not alternated. However, if the numerical simulation is characterized by large slings, the matrix components will vary due to the sliding of contractor nodes along target surfaces. For this purpose, even if a very small time increment Δt is adopted, which will consequently produce a relatively small incremental nodal displacements, it would be convenient to calculate $\mathbf{G}_{\mathrm{n+1}}$ at the beginning of each Gauss-Seidel iteration process or at the beginning of each time increment.

The k to $k+1$ Gauss-Siedel iteration is summarized in equation 5.16. with the following special notation. The upper left superscripts in displacement and force terms represent the current iteration, i.e. ${}^{k}u_{n}^{i}$ represents the displacement of contractor i, at time n at the beginning of iteration step k, while ${}^{k+1}u_{n}^{i}$ the respective value at the end of the same iteration. The difference between the two is Δu^{i}. The current estimate of u_{n+1}^{i}, during iteration k to $k+1$, is ${}^{k,k+1}u_{n+1}^{i}$. In each iteration a loop is performed over all contractor nodes i, with n_c being the number of contractor nodes. For the first iteration $\Delta\mathbf{u}^{c}$, $\mathbf{u}_{n+1}^{c}$,

$\Delta\boldsymbol{\lambda}$ and $\boldsymbol{\lambda}_n$ are set to zero.

$$\text{for} \quad i = 1, 2, ..., n_c \tag{5.16.a}$$

$$^{k,k+1}\mathbf{g}^i = \mathbf{G}^i_{n+1}\{\mathbf{X}_n + \mathbf{u}^D_{n+1} + \mathbf{u}^C_{n+1}\} \tag{5.16.b}$$

$$\Delta\boldsymbol{\lambda}^i = \left[\Delta t^2 \mathbf{G}^i_{n+1}\mathbf{M}^{-1}\left(\mathbf{G}^{\mathbf{i}}_{\mathbf{n+1}}\right)^{\mathrm{T}}\right]^{-1} \cdot {}^{k,k+1}\mathbf{g}^i \tag{5.16.c}$$

$$^{k+1}\boldsymbol{\lambda}^i_n = {}^{k}\boldsymbol{\lambda}^i_n + \Delta\boldsymbol{\lambda}^i \quad \rightarrow \quad \text{friction model} \tag{5.16.d}$$

$$\Delta\mathbf{u}^c = -\Delta t^2 \mathbf{M}^{-1}\left(\mathbf{G}^i_{n+1}\right)^{\mathrm{T}} \Delta\boldsymbol{\lambda}^i \tag{5.16.e}$$

$$^{k,k+1}\mathbf{u}^c_{n+1} \leftarrow \left\{ {}^{k,k+1}\mathbf{u}^c_{n+1} + \Delta\mathbf{u}^c \right\} \tag{5.16.f}$$

After the last step in (5.16.) a convergence test has to be performed:

$$\|\Delta\lambda\| < tol\| \, ^{i+1}\Lambda_n\|. \tag{5.17.}$$

An simple example of contact analysis is illustrated in Figure 5.6. An elastic sphere collide with a rigid flat surface with the friction coefficient μ set to 0 and 1.

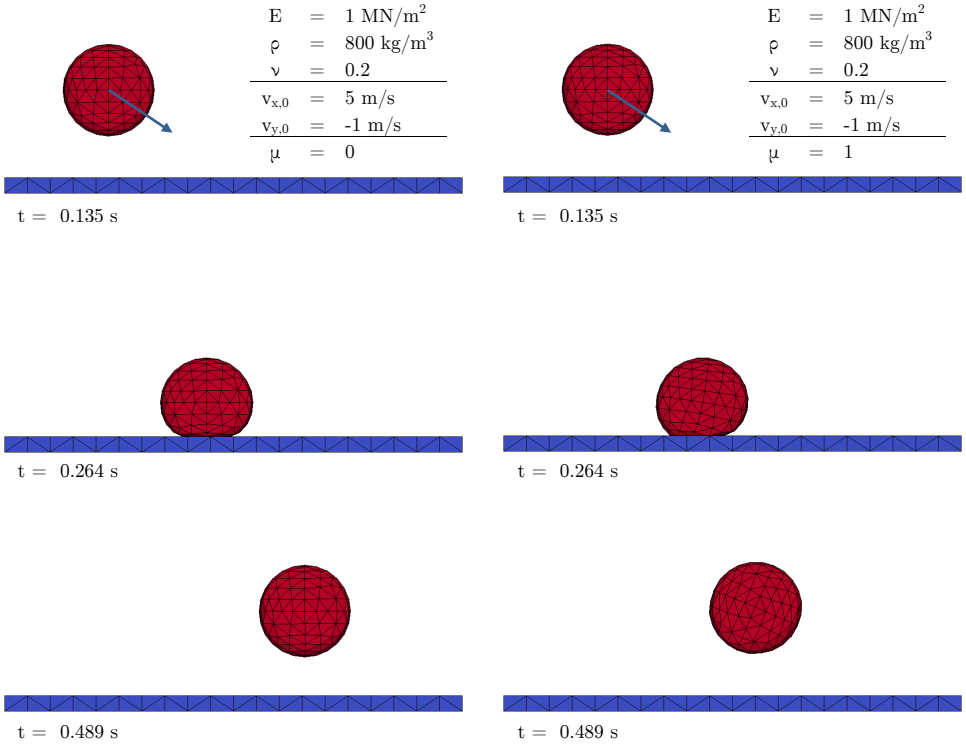

Figure 5.6.: Collision of a sphere with a flat rigid surface: (a) left column $\mu = 0$, (b) right column $\mu = 1$.

In case of $\mu = 0$, i.e. no friction, after impact the sphere continues on its trajectory with no rotation and throughout the impact the deformation of the sphere is symmetric. On

the other hand, when $\mu = 1$, the friction cause the sphere to rotate. The transformation of energies for both cases is shown in Figure 5.7. In the first case (no friction) there is no energy loss, while in the second case, the dissipation of energy due to friction is evident throughout the impact time, resulting in the decrease of sphere speed (kinetic energy).

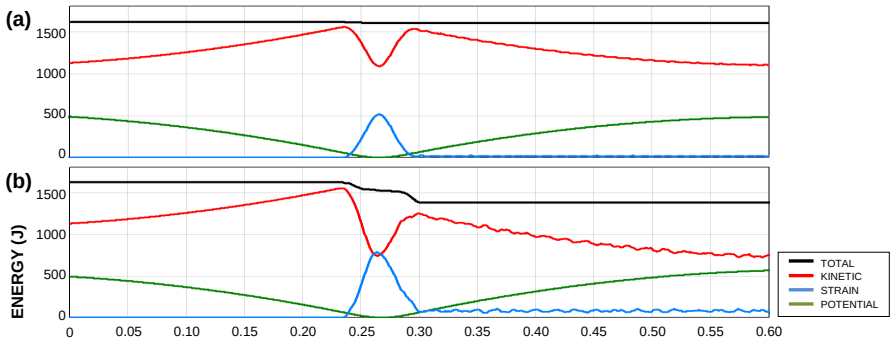

Figure 5.7.: Collision of a sphere with a flat rigid surface: (a) left column $\mu = 0$, (b) right column $\mu = 1$.

Chapter 6.

Computer program structure and computational aspects

6.1. Computer program structure

The primary objective of this thesis was the development and application of an original computer program for three-dimensional non-linear dynamic analysis of site and structure response with emphasis on SSI. The programme code was developed in Fortran95 program language with PGI Visual Fortran (PGI, 2010). Femap (Siemens, 2009) was used as a pre-processing tool (3D modelling and FE mesh generation) and Para View (Kitware, 2012) as a post-processing tool (data processing and visualisation). See Figure 6.1.

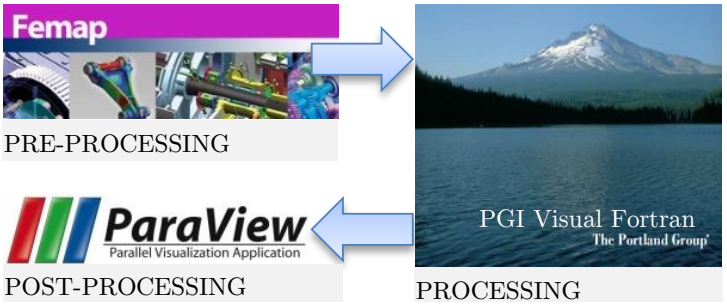

Figure 6.1.: Pre-processing, processing and post-processing tools and their connection.

The program itself consists of 96 source files containing more then 7,000 code lines. The structure of the program can be explained by taking a look at the main program file `main.f90`, see Listing 6.1. At the very beginning of the main file is the information on the current program version. Next, there are two blocks of sub-routines: (1) the initialisation block (lines 7 to 23), and (2) the main loop for the incremental analysis (lines 26

to 49).

```
1   PROGRAM _main
2   USE MOD_DATA
3   IMPLICIT NONE
4
5   Ver = "EQ.30.10"
6
7   CALL INI
8   CALL ini_DATA
9   CALL ini_MESH
10  CALL ini_Time_History
11  CALL ini_MEMO
12  CALL ini_MICROPLANE
13  CALL Damping
14  CALL ELT4
15  CALL ELH8
16  CALL EFT_NFT
17  CALL Dmtx
18  CALL CRITICAL_dt
19  CALL ini_CONTACT
20  CALL EXPLICIT_INTEGRATION
21  CALL Mass
22  CALL INFO
23  CALL START
24
25  !############################ LOOP ###
26 2 CALL SOLVER                 !
27  !---------------------------!
28   CALL CONTACTsolve          !
29  !---------------------------!
30   CALL VEL_ACC               !
31   CALL Reactions             !
32   CALL ENERGY                !
33  !---------------------------!
34   CALL DEFORMATION_GRADIENT  !
35   CALL GREEN_LAGRANGE        !
36   CALL STRESS                !
37   CALL Finternal             !
38  !---------------------------!
39   CALL ETM                   !
40   CALL OUTPUT_MC             !
41   CALL OUTPUT_PV             !
42   CALL OUTPUT_SCR            !
43   CALL Recovery              !
44  !---------------------------!
45   CALL UPDATE                !
46  !---------------------------!
47   CALL TheEnd                !
48  !---------------------------!
49   GOTO 2                     !
50  !############################ LOOP ###
51
52   END PROGRAM
```

Listing 6.1.: Main file

The subroutines in the initialisation block are executed only once, at the starting of the program, and before the actual incremental analysis. The `ini` sub-routines allocate the needed space in the high-speed memory and read all the input data (material properties, loads, contact parameters and FE mesh data). The subroutine `damping` sets the appropriate damping factors and builds the damping vector (see equation (7.2.) and Figure 7.2.). Subroutines `ELT4` and `ELH8` calculate the shape functions for tetrahedral and hexaherdal elements, respectively (section 2.1.). `EFT-NFT` then forms a list of degreees of

freedom per element and per node. `Dmtx` forms an elasticity matrix for each material in the analysis as in (4.3.). `CRITICAL_dt` calculates the critical time increment according to (2.43.) and (2.44.) and set Δt to a lower value by multiplying it with a predefined factor less than 1. `EXPLICIT_INTEGRATION` calculates the vectors ${}^{0-\Delta t}u_i$ or ${}^{0-\Delta t}\dot{u}_i$ depending on whether the central difference or leap-frog method was chosen according to equations (2.37.) and (2.41.). `INFO` writes a file containing all parameters for the current analysis for user reference. And finally, `START` calls the welcome screen shown in Figure 6.2. The welcome screen of the program shows the calculated critical time step and the adopted time step, the program version, and offers four choices: (1) start of a new analysis, (2) read the input data from a previously performed static analysis, (3) read the input data from a previously performed dynamic analysis, and (4) continue a previously started analysis (form the backup location). After selecting one of the options, it is required to enter a number of increments and then the analysis starts.

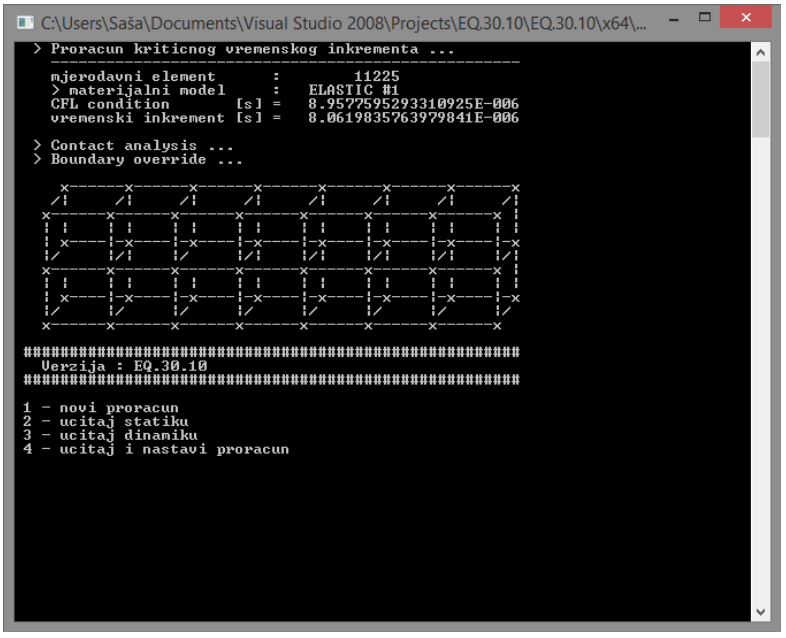

Figure 6.2.: Welcome screen of the program

After the initialisation block is over, the main loop for the incremental analysis is started for a prescribed number of increments. The loop starts with the subroutine `SOLVER` which computes the displacement vector according to the chosen integration method as in (2.38.) or (2.41.). If the analysis includes a contact problem then the subroutine `CONTACTsolve` is called. It is performed as one or two-pass algorithm in three stages: global detection, local detection and contact resolution. When the new displacement vector is finally computed, subroutines `VEL_ACC`, `Reactions`, and `ENERGY` compute the velocity and acceleration vectors, reactions if needed, and potential, kinetic and strain

energy for the current time step. `DEFORMATION_GRADIENT` compute the deformation gradient for every element in every Gauss point according to (3.13.) and optionally performs its polar decomposition. `GREEN-LAGRANGE` computes the Green-Lagrange strain tensor as in (3.18.). For the imposed strains increments `STRESS` computes the coresponding stresses according to one of the included material descriptions (elastic, plastic or microplane model). `Finternal` computes the vector of internal forces by integrating the stresses as in (3.26.). `ETM` estimates the time remaining till the end of the analysis based on progress so far. Subroutines `OUTPUT_MC` and `OUTPUT_PV` writes all selected output data for the current increment formatted for MathCAD and ParaView programs. `OUTPUT_SCR` writes the basic analysis information on screen for user control. `RECOVERY` is called sporadically to perform a back-up of the current progress. Finally the subroutine `UPDATE` update the displacement and velocity vectors for the explicit integration, and strain vectors for the stress analysis in the next time step. When the number of prescribed increments is reached `TheEnd` writes on screen a summary of the performed analysis with the options to continue the analysis by entering an additional number of increments or save the progress.

6.2. Computational aspects

Any non-linear numerical analysis of site response and SSI is always challenging because inevitably involves large and complex models requiring considerable computational effort. Consequently, the problem of computational efficiency merges naturally. Both numerical studies here presented are computationally demanding, but involve different challenges. This section covers several computational aspects of the program implementation and briefly discusses the benefits and disadvantages of the chosen numerical approach.

The first numerical study involves a very large model (ground representation) which is by itself computationally demanding. Nevertheless the most expensive routines are those involving the microplane model. The application of such an expensive model can be easily justified by a very accurate representation of concrete which allows a three-dimensional damage and fracture analysis within the smeared crack approach. In this sense, such approach is superior to the classical structure representation using beam elements.

The second numerical study involves a much smaller model, the considered structure is simplified and treated as elastic, but the computation is nevertheless equally demanding. Namely, the computational challenge lies in the effective implementation of the contact mechanics procedures. The contact procedure, as previously discussed, consists of three stages: global detection, local detection and contact resolution. Contact resolution is effectively performed using the Gauss-Siedel iteration procedure shown in (5.16.). Since

the adopted procedure resolves contact elements independently, the computational time is proportional to the number of contacts and the convergence is linear. The adopted local detection strategy is equally effective. The most time consuming stage by far, which makes the contact procedure expensive overall, is the global detection. In a general case, like the one shown in Figure 5.6., it is impossible to predict all the contractor nodes in advanced so the detection procedure must be general. But, in the case of the considered problem, the contractor list can be known in advanced. Also the list of potential target surfaces can be narrowed down to a small area around the foundation. In this way, the computational time is dramatically shortened. Obviously, that means that an eventual complete overturning of the structure would not be detected. In that case a general detection should be employed.

One of the most important choices in the process of approaching these problem was the selection of method of solving the dynamic equation of motion. Namely, there are several reasons why the dynamic equation of motion is integrated in an explicit manner rather than using an implicit version. It should be noted that the explicit time integration is found to be more appropriated to simulate the process of cracking in the concrete than the implicit ones. Namely, opening of new cracks (and their closure) happen in a in a very short period of time. Consequently, a very short time increment is needed to be able to capture these effects in a proper manner which automatically makes implicit schemes less attractive. Additionally, for the microplane material model, the computation of the local tangent matrix will be more expensive than retriving the stresses from the given strains, which is the case in the explicit time integration. The same can be concluded for the used plastic model for the soil. It is interesting to note the memory requirements for an implicit solution. The actual stiffness matrix in its original form is just too big for any practical purpose. In the actual computer solution, the stiffness matrix has to be condensed in a one-dimensional array containing only element on the main diagonal and all non-zero elements above the diagonal of the original matrix. Even in this condensed form (for the presented problem, see Figure 6.3.), the stiffness "array" contains approximately $1.5 \cdot 10^9$ elements which in double-precision format takes 11.0 GB of storage space.

Since the solution in the explicit schemes can be carried out on the element level, little high-speed storage is needed and systems of very large order can be solved effectively. For the presented problem, the entire high-speed memory demand is approximately 300 MB. However, to obtain a stable numerical solution, the adopted time step Δt has to be smaller than the computed critical one Δt_{cr}. For the first numerical study, a uniform time step of 6.25 μs is adopted. A small time step is not needed only for ensuring the stability of the solution, but also, as noted above, to be able to capture the cracking of the concrete, which happens in very short period of time.

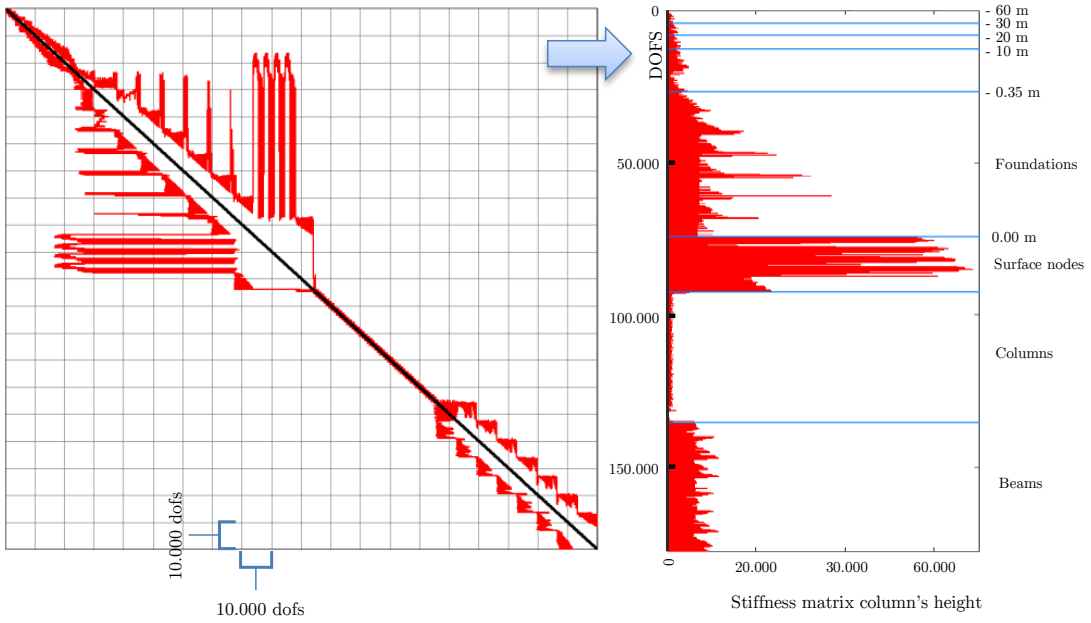

Figure 6.3.: The stifnness matrix topology and its condensed vector form

As was discussed in Section 2.2.2. explicit methods are viable methods only when a lumped mass matrix can be assumed. Additionally, for solving (2.30.) there is no need for the assemblage of the stiffness matrix (the internal forces are are computed by stress integration on element level). Consequently, the damping matrix $\mathbf{C}$ cannot be related to the stiffness matrix, but should be defined as $\beta\mathbf{M}$ where β is a real number (Wilson, 1995) which is an approximation needed for preserving computational efficiency.

In both numerical studies, before starting the dynamic analysis, the initial field of deformations and stresses has to be obtained by performing a static analysis. For practical purposes, the static analysis is replaced with a dynamic analysis with critical damping. This approach is much more computationally efficient, especially for the problem in the first study.

The inevitable issue of computational efficiency can be approached by parallelisation of the most expensive routines using OpenMP or similar procedures. The idea of parallerisation is to distribute the computation of a non-iterative loops to all available CPU cores instead of computing them in a serial manner by one core only. An efficient implementation of OpenMP procedures is not a trivial task and was outside the scope of this research.

Chapter 7.

Numerical studies

7.1. Numerical study 1

This study is based on a series of numerical analyses which include modelling of a reinforced concrete frame with a large portion of the ground consisting of various horizontal layers resting on rigid bedrock (see Figure 7.1.). The ground is modelled as a cylinder 60 m deep with a diameter of 120 m. The cylinder consists of two layers, each with a thickness of 30 m. The FE discretisation of the ground is shown in Figure 7.1.a (upper level is shown in orange and the lower layer is shown in dark grey). The ground is discretised with tetrahedral elements while the structure is modelled employing hexahedral elements. The input motion is applied in the bottom nodes of the cylinder in the form of an accelerogram in the desired horizontal direction which generates vertically propagating shear waves. These waves travel from its source (at the bedrock) through different ground layers, finally reaching the surface. They reflect from the surface back to the rigid bedrock, which also acts as a perfect reflector. Through time, they superimpose themselves with new waves originating from the source which contributes to the attenuation or amplifications of the surface wave amplitudes.

Ground types used in the present study are rock masses with properties shown in Table 7.1. These parameters were determined using RocLab (Rocscience, 2002) which is based on the Hoek–Brown failure criterion (Hoek and Diederichs, 2006).

The Hoek–Brown failure criterion is widely used for determining input parameters for analysis of rock mass behaviour. It consists of empirical relationships for estimating parameters of an isotropic rock mass deformation modulus based on Geological Strength Index (GSI) classification scheme and several additional parameters. It also provides equivalent Mohr–Coulomb or Drucker–Prager input parameters, which were then used

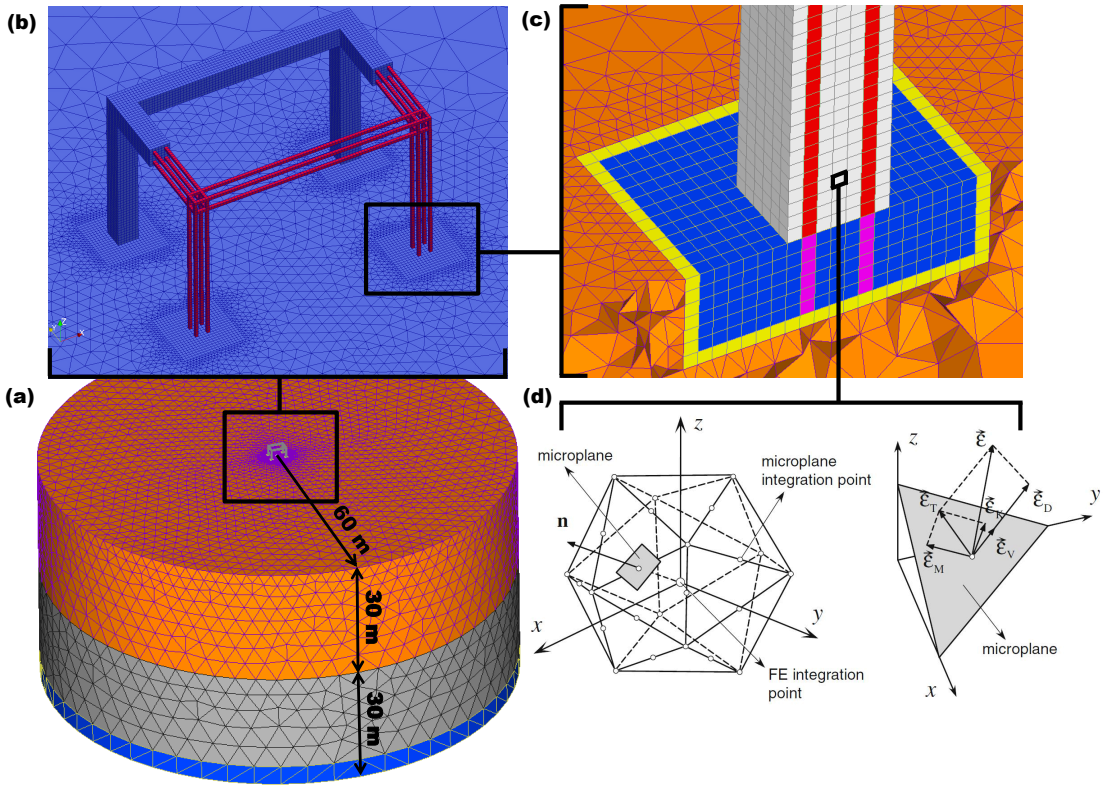

Figure 7.1.: (a) FE model of the ground: upper layer (orange), lower layer (dark grey) and elastic bottom layer on which is applied the input motion (blue), (b) reinforced concrete frame discretisation, (c) section of the FE model: concrete (white), concrete elastic (blue), reinforcement (red), reinforcement elastic (magenta), interface elements (yellow), ground top layer (orange) and (d) decomposition of the macroscopic strain vector into microplane strain components - normal (volumetric and deviatoric) and shear.

Table 7.1.: List of ground types: deformation modulus, uniaxial compressive and tensile strength, normal and shear wave propagation velocities.

Ground type	E_{rm} (GPa)	f_c (MPa)	f_t (MPa)	v_{NORMAL} (m/s)	v_{SHEAR} (m/s)
1	0.610	0.143	0.004	510.6	312.7
2	1.220	0.613	0.013	722.1	442.2
3	2.440	1.290	0.029	1021.1	625.3
4	4.880	2.427	0.062	1444.1	884.3
5	9.760	4.938	0.157	2042.3	1250.6

in this study. GSI values are estimated from lithology, structure and surface condition of the discontinuities and have a range between 0 and 100. Rock mass deformation moduli are calculated varying the geological strength index (GSI) from 10 (laminated, sheared structure with poor surface condition) to 60 (blocky structure with fair surface condition). Starting with the softest ground type 1 (E_{rm} = 0.610 GPa), the rock mass deformation modulus is doubled in each subsequent step to the stiffest ground type 5 (E_{rm} = 9.760 GPa). In this way, a large span of rock mass stiffness is covered. Note that the stiffness ratio between ground type 5 and 1 is 16, while the shear wave velocity ratio is 4. The described ground types, according to shear wave velocity, would be commonly classified from type C ($180 < v_{s,30} < 360$ m/s) to type A ($v_{s,30} > 800$ m/s) where $v_{s,30}$ is the average value of propagation velocity of S waves in the upper 30 m of the soil profiles. Since the density is the same for all considered ground types, the vertical pressure at the bottom is equal for all investigated models and it has a value of approximately 1.5 MPa. While the stress distribution is similar for all models, the strains differ and consequently the total strain energy stored in the system. The strain energy is then inversely proportional to the ground stiffness.

Varying the ground types for the two layers overlaying the bedrock, a total of 15 different configurations are considered. The individual configuration is given a name in the form of Mxy: x standing for the ground type of the upper layer and y standing for the ground type of the lower layer (see Table 7.1.). The configurations in which the upper layer is stiffer than the lower layer are not considered.

The described ground configurations are further expanded by placing a reinforced concrete structure in the centre of the ground model (Figures 7.1.b and 7.1.c). The structure is a RC space frame with the following dimensions: height is 2.80 m, the longer span (x direction) is 4.20 m and the shorter span (y direction) is 2.80 m. The cross section of the columns and beams are 350 x 350 mm. The columns are based on square footings 1050 x 1050 x 350 mm. Columns and beams are reinforced with four steel rebars with diameter d = 14 mm. The mass of the beams is increased to account for an extra live load of 5 kN/m2 applied to the entire area of the frame storey. The total mass of the frame (without the foundations) is 9973 kg. Assuming linear elastic behaviour, the first three eigenvalues of the frame are 0.0762 s (x direction), 0.0728 s (y direction) and 0.0581 s (torsion). The mechanical properties of the concrete are: modulus of elasticity E_c = 30 GPa, Poisson's ratio $\nu = 0.18$, uni-axial compressive strength f_c = 45.0 MPa, tensile strength f_t = 2.70 MPa, fracture energy G_F = 0.10 N/mm and mass density ρ_c = 2300 kg/m3. The mechanical properties of the steel reinforcement are: E_s = 200 GPa, ν = 0.30, yield strength f_{yd} = 400 MPa and ρ_s = 7850 kg/m3. The discretisation of concrete and reinforcement is performed with linear hexahedrons (Figures 7.1.b and 7.1.c). Since the section of the actual reinforcement is smaller than the area of the elements used to

model it, the modulus of deformation and the yield strength of the reinforcement were reduced in an adequate manner to assure an objective modelling. To obtain a more realistic interaction between the column footings and the ground, a row of non-linear interface elements were inserted (shown in yellow in Figure 7.1.c). These elements can take up compressive and but no tensile stresses.

Prior to the dynamic analysis, a static analysis was performed to obtain the initial field of deformations and stresses indispensable for further dynamic analyses. For the static analysis, Dirichlet conditions of zero displacements are imposed at the bottom surface in the vertical direction and at the lateral surface in the horizontal direction (see Figure 7.2.a). In the dynamic analysis, perfect reflection characteristics of such elementary boundaries can trap the energy in the mesh that in reality would propagate in the radial direction away from the region of interest resulting in the so-called box effect. To prevent this effect, on each node of the lateral boundary, a set of viscous dampers (zero length elements, see Figure 7.2.b) is placed according to Lysmer and Kuhlemeyer boundary condition (Lysmer and Kuhlemeyer, 1969) expressed by the following equations:

$$\sigma = \rho\, v_p\, \dot{u}_n\,, \quad \tau = \rho\, v_s\, \dot{u}_t, \tag{7.1.}$$

where σ and τ are the normal and shear stress on the boundary, v_p and v_s are the velocities of the P waves and S waves in the base material, ρ is the density of the base material and $\dot{u}_n$ and $\dot{u}_t$ are the normal and tangential particle velocities at the boundary. Radiation damping can be derived according to these equations and then applied using lumped dashpots with the following factors:

$$C_{n,i} = a\, \rho\, v_p \int N_i \,\mathrm{d}A, \quad C_{t,i} = b\, \rho\, v_s \int N_i \,\mathrm{d}A, \tag{7.2.}$$

where N_i is the element shape function, and a and b are dimensionless parameters. For small incident values the most effective value for a and b is one. Additionally, the static pressure at the lateral boundaries obtained from the static analysis is applied on the respective boundary of the dynamic model. At the start of the dynamic analysis, all fixed supports on the nodes at the base of the model are removed and a time-history acceleration is specified. In other words, the motion at the base of the model is completely prescribed in all three directions according to the specified accelerogram (see Figure 7.2.b).

The earthquake record used in the present study is taken from the Japanese digital strong-motion seismograph network Kik-net (NIED, 2013) which consists of pairs of seismographs installed in borehole together with seismographs on the ground surface. The accelerogram shown in Figure 7.3. was recorded at the Gozenyama site on 11

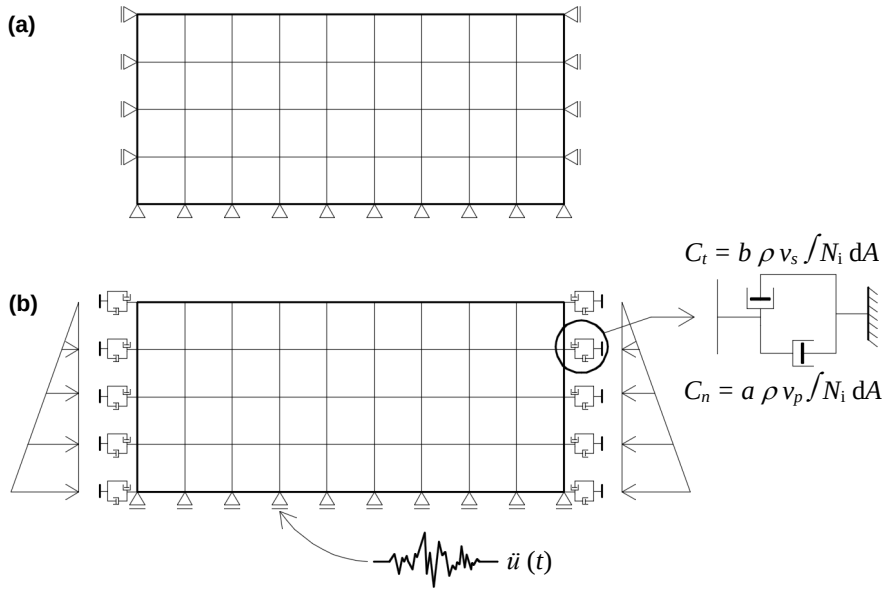

Figure 7.2.: Simplified 2D representation of boundary conditions for (a) static analysis and (b) dynamic analysis.

March 2011 on a borehole seismograph installed on bedrock at an altitude of −62 m (see Appendix A for more information). Since the used accelerogram does not represent outcrop motions, but rather "in-depth" motions, the deconvolution analysis is not really necessary. The numerical analysis is performed for a 2.25 s fragment of the original record scaled to peak ground acceleration (PGA) of 0.1 g with peak ground velocity (PGV) equal to 0.05405 m/s and peak ground displacement (PGD) equal to 0.00683 m. The selected fragment has a mean period of 0.24 s and produces an acceleration response spectrum with a relative narrow band in the high frequency range. The described accelerogram is applied at the bottom nodes of the model in the x direction. The elements containing one or more of these nodes were modelled as elastic (shown in blue in Figure 7.1.(a)).

Figure 7.4. shows the arrival of shear waves to the ground surface for configurations M11, M22, M33, M44 and M55 in the form of horizontal displacements. The waves are generated by the input motion described above. Decreasing the ground stiffness (from M55 to M11) the shear wave velocity decreases taking more time for the wave to reach the surface. At the same time, the amplitudes and periods of the surface motion increase in magnitude.

A comparison between considered models regarding PGA, PGV and PGV/PGA is shown in Table 7.2. The PGA and PGV are very useful parameters for characterising ground motion amplitudes, PGA providing a more accurate estimation in the high frequencies range while PGV in intermediate range. The PGV/PGA parameter is often used to characterise the damage potential of the ground motions, i.e. higher values meaning larger

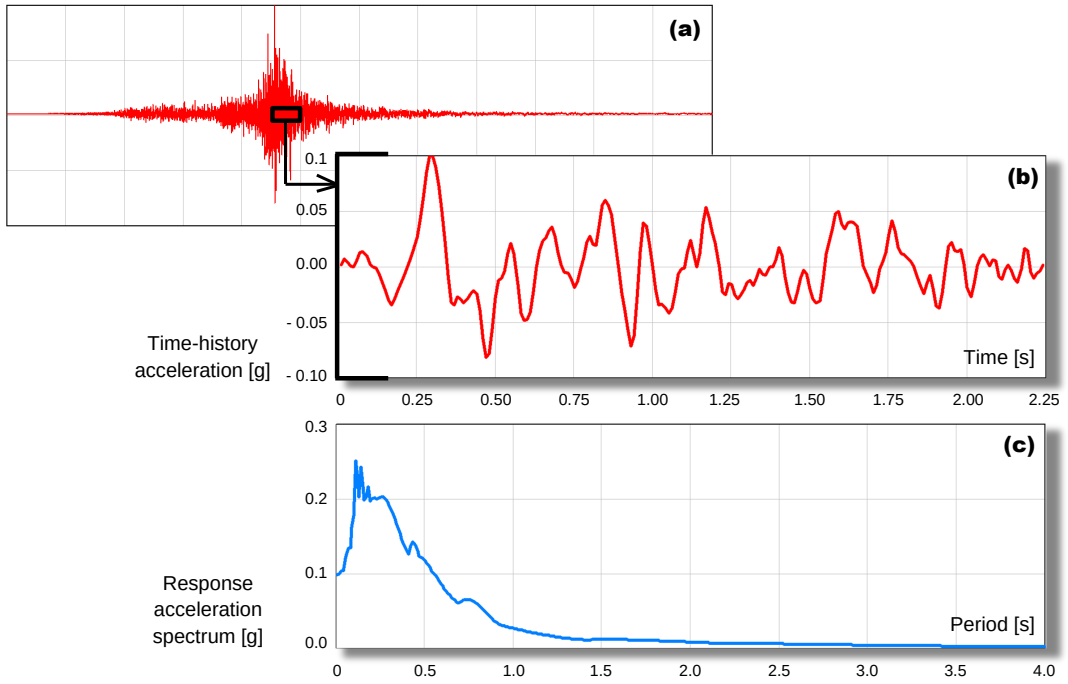

Figure 7.3.: (a) Full Gozenyama earthquake record, (b) the strongest 2.25 s fragment used in the analysis and (c) respective response acceleration specrtum.

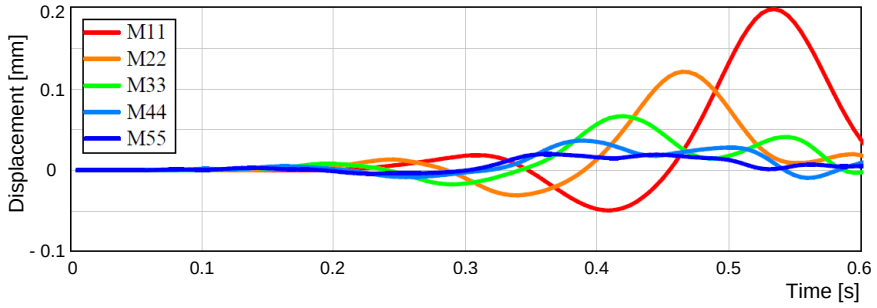

Figure 7.4.: Arrival of shear waves at the ground surface (showing horizontal displacements).

damage potential. All mentioned parameters tend to be larger as the ground becomes softer (see Table 7.2.). Namely, the largest values were obtained for configurations with the softest top layer. The ratio between the maximum recorded PGA (model M13) and the minimum recorded PGA (model M55) is roughly four while the stiffness ratio is 16.

The response acceleration spectra for all models are shown in Figure 7.5.a and they represent peak response values of a SDOF system subjected to the given accelerogram with a critical damping ratio of 5%. Models are grouped accordingly to the ground type of the upper level: red for ground type 1, yellow for 2, green for 3, blue for 4 and black for 5. It can be seen that the models with the top layer of the same ground type

Table 7.2.: Considered models with resulting PGA, PGV and PGV/PGA ratio.

Model	PGA (g)	PGV (m/s)	PGV/PGA (s)
M15	0.125	0.02705	0.0220
M25	0.107	0.02131	0.0202
M35	0.096	0.01625	0.0172
M45	0.081	0.01171	0.0148
M55	0.042	0.00504	0.0122
M14	0.129	0.03096	0.0245
M24	0.136	0.02311	0.0173
M34	0.114	0.01989	0.0178
M44	0.065	0.01088	0.0171
M13	0.191	0.03733	0.0199
M23	0.117	0.02439	0.0213
M33	0.110	0.01939	0.0180
M12	0.152	0.03506	0.0235
M22	0.121	0.02323	0.0196
M11	0.139	0.03315	0.0243

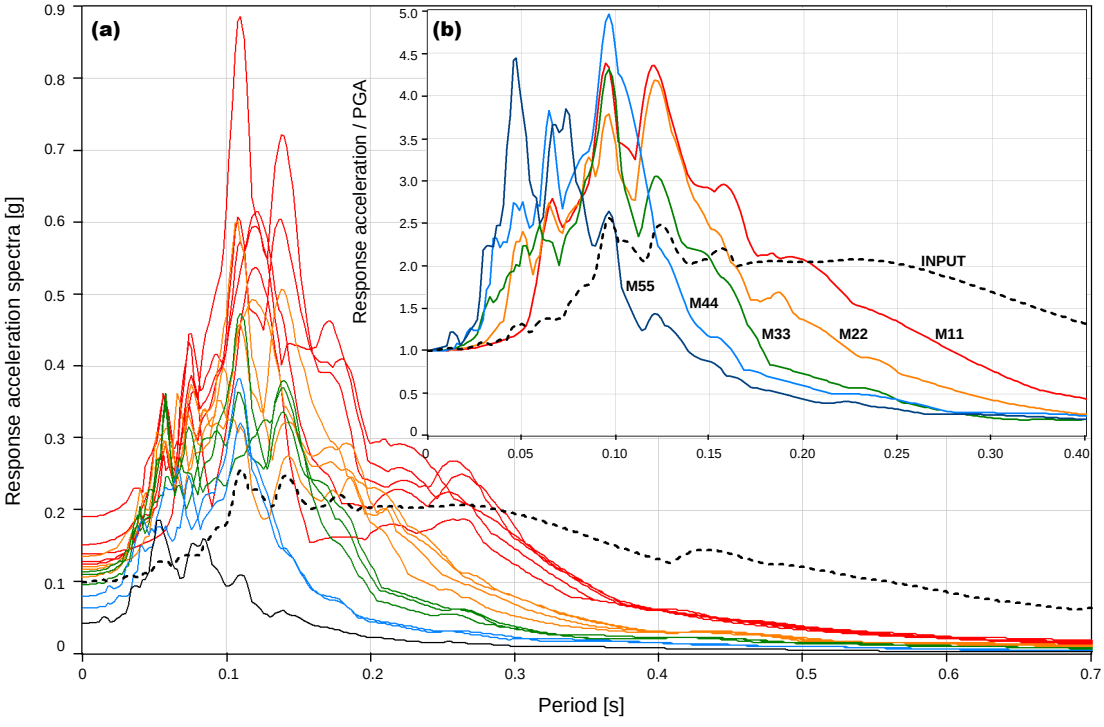

Figure 7.5.: (a) Resultant acceleration spectra for the models with material 1 (red), 2 (yellow), 3 (green), 4 (blue) and 5 (dark blue) as top layer; response spectra of the input accelerogram is represented with a dashed black line and (b) Normalised response spectra for the models with equal upper and lower materials and the response spectra of the input accelerogram.

have the acceleration response spectra grouped closely together. The ground type of the top layer has a great influence on ground motion characteristics while the ground type of the bottom layer has only a minor influence. Maximum amplification of accelerations (ground/bedrock) is observed for the model M13 (1.91) while the maximum de-amplification is observed for model M55 (0.42). Figure 7.5.b show normalised acceleration response spectra for models M11, M22, M33, M44 and M55 and for the input accelerogram. It can be seen that softer sites amplified the medium-range bedrock frequencies more than stiffer sites. Similarly, the stiffer sites amplified high-range frequencies more than softer sites. It is important to note that the non-linear behaviour of soil makes the amplification dependent on the bedrock motion magnitude, i.e. stronger motion causes more non-linear behaviour which generally reduces the amplifications. Since the bedrock is assumed to be perfectly rigid, the incoming waves reflected from the surfaces will again be perfectly reflected from the bedrock, i.e. there is no loss of energy. More accurate modelling would regard the bedrock as elastic. This would mean that only a part of the incoming wave would be reflected and the other part would continue travelling downward (radiation damping). The transmitting wave removes energy from the soil deposit and makes its response to be lower than it would have been for the case of rigid bedrock. For some soft rock sites, rigid bedrock assumption can lead to overestimation of amplification effects.

The response of the RC frame for the model M33 is shown in Figure 7.6.. The displacements, velocities and accelerations (ground, storey and relative) in the x direction are shown in Figures 7.6.a, 7.6.b and 7.6.c, respectively. Total base shear history is shown in 7.6.d and energy transformations are shown in 7.6.e. Reactions of the individual columns for all three directions is shown in Figure B1. in the Appendix B.

The shear waves propagate 60 m from their source to the surface in 0.1 s. After 2.4 s the surface ground motion practically stops and the structure continues to oscillate freely. Maximum recorded acceleration of the storey is 0.56 g while the PGA is 0.11 g. The maximum base shear is 55 kN. The energy of RC varies through time between 3 (in resting) and the maximum of 24 J. Cracking of concrete cover is observed in the base of the columns and beams while the reinforcement remains elastic.

Figures 7.7.a and 7.7.b shows the energy transformations in the entire system during the analysis. The total and the strain energy practically coincide because the kinetic and potential energies are of much lower magnitude. Namely, the total energy varies between 97 and 105 MJ while the kinetic energy varies between zero and 0.3 MJ. The induced earthquake motion raised the total energy of the system by approximately 10 MJ. As expected, it can be seen that the contribution of the potential energy in the total energy of the system can be neglected.

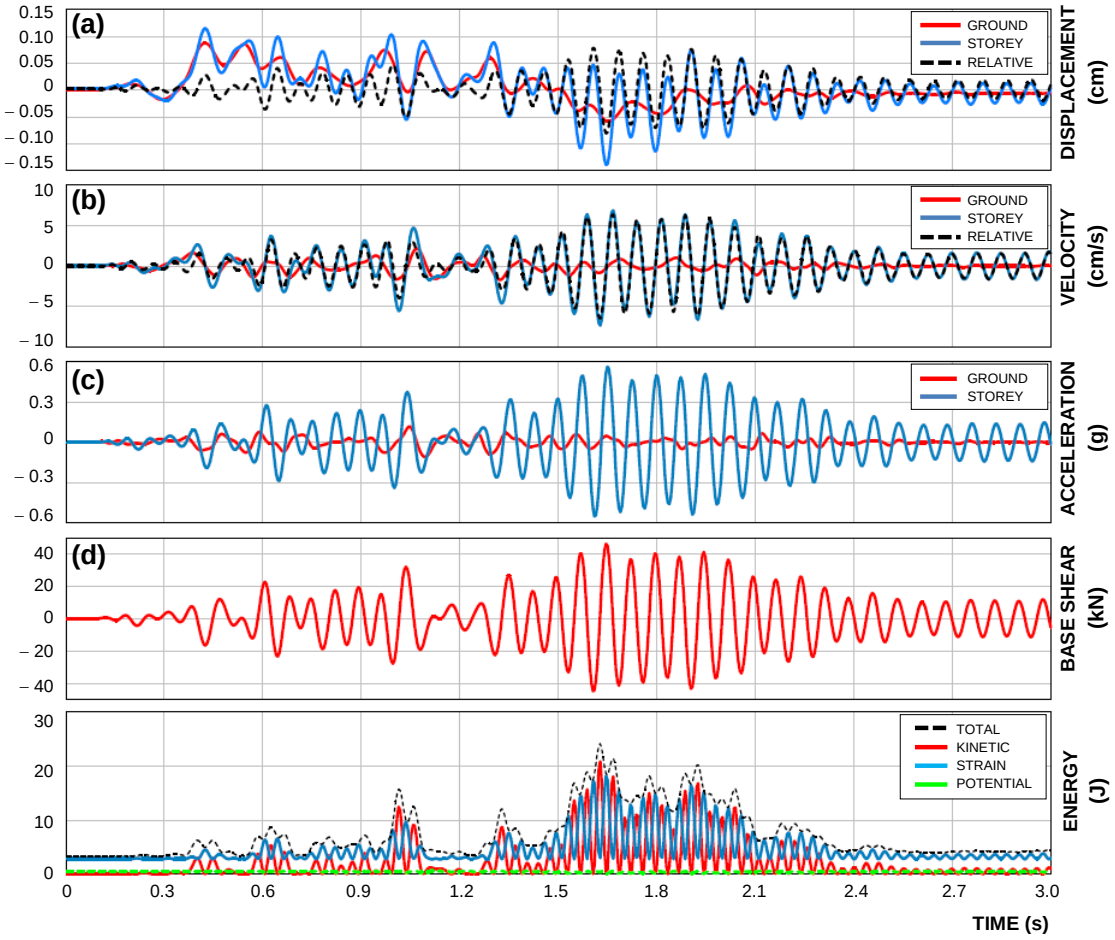

Figure 7.6.: (a) Displacements, (b) velocities, (c) acceleration history, (d) total base shear, and (e) energy transformations for the considered RC frame (model M33).

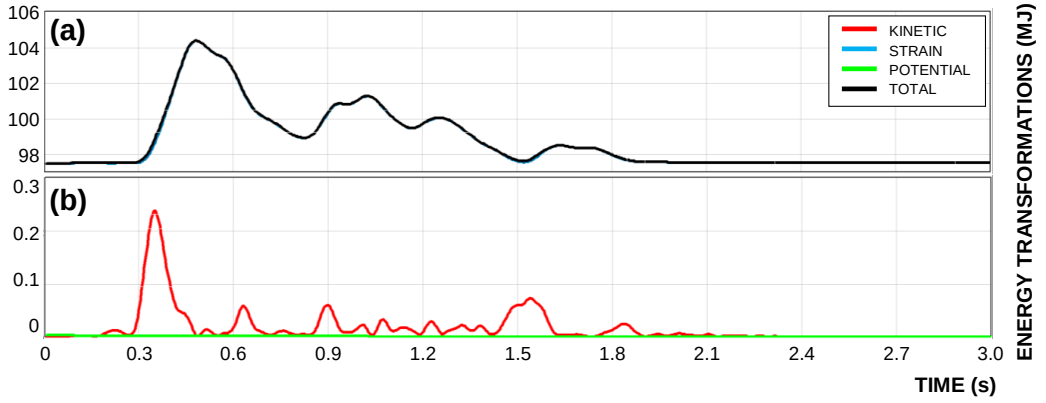

Figure 7.7.: Energy transformations in the entire system for model M33.

Additional simulations were performed considering the structure linear elastic with SSI. Structural response resulting from a linear elastic analysis with initial stiffness is shown in Figure 7.8.. Although the selected input motion is relatively low in magnitude, the difference in the structural response in regard to non-linear analysis is evident. Non-linear effects, i.e. structure stiffness degradation, lead to lower natural frequencies of the structure. Thus, as can be seen from the acceleration response spectra in Figure 7.5., even a small difference in the fundamental period of oscillation can have a major effect on the structural response. Prolongation of the fundamental period is not only caused by structural degradation (cracking of concrete, yielding of reinforcement), but also because of ground non-linearity around the foundation and the applied interface between the foundation and the ground. Described phenomena, which are accounted for in the proposed model, are of crucial importance for a realistic response. Moreover, in the design practice, it is usually assumed that a simpler linear analysis is more conservative than an advanced non-linear analysis. This assumption is not generally true, which means that accounting for all non-linearities does not necessarily mean that the demand on the structure will be lower. The scope of advanced methods is not only to design more economical structures, but also to identify weak spots which cannot be detected when employing a relatively simple method of analysis.

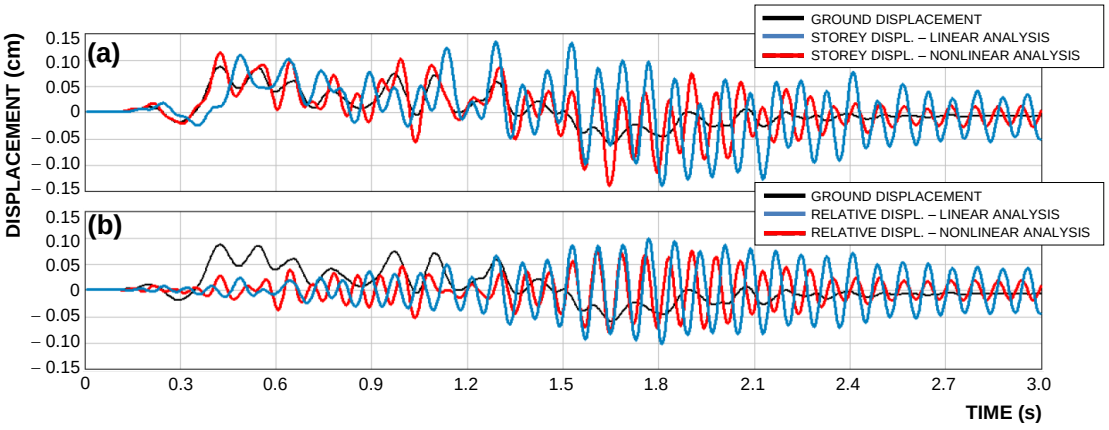

Figure 7.8.: (a) ground and storey and (b) ground and relative displacements for the considered RC frame (model M33) resulting from non-linear and linear analysis with initial stiffness.

The original input motion was increased in magnitude by a factor of 5 to induce more damage on the RC structure. A typical failure mode of the considered structure in the x direction is shown in Figure 7.9.. The cracking of the concrete (red zone) is represented by means of maximal principal strains. For this purpose, it is assumed that the critical crack opening w_{cr} is 0.2 mm, which corresponds to the critical strain $\varepsilon_{cr} = w_{cr}/h_e = 0.004$, where h_e is the average element size (50 mm). Yielding of reinforcement is shown in red. First, cracks in the concrete appear at the base of the columns. Cracks in the

longitudinal beams follow: in the upper zone of the section on one side and in the lower zone on the other. The cracking progression in the members of the RC frame is shown in Figure B3. and Figure B2. shows the time-history of the principle stress σ_{zz} for an individual element in the cracking zone (see Appendix B).

Maximum total base shear of the frame reached 120 kN while the strain energy was 136 J. Furthermore, it would be possible to continue the simulation and to assess the performance of such a damaged structure to a future aftershock.

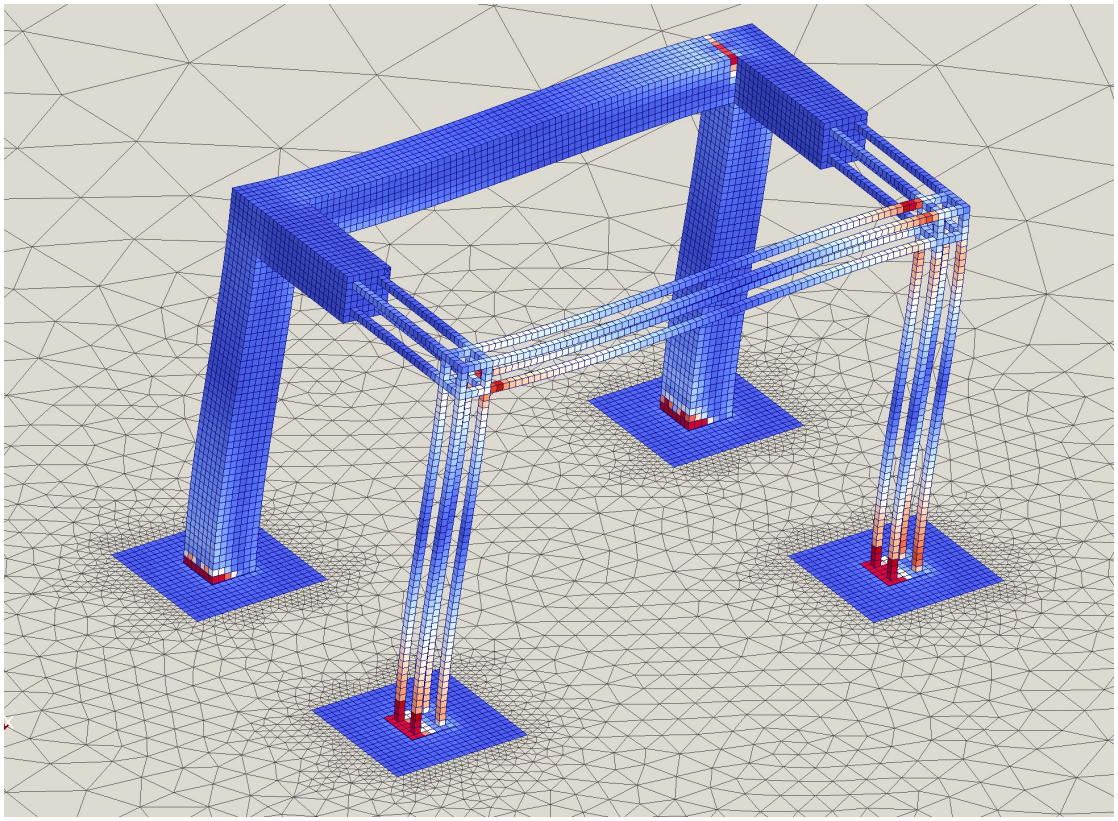

Figure 7.9.: Failure mode of the RC frame.

Minimal element size was set to 50 mm resulting in a mesh with approximately 120,000 elements and 180,000 degrees of freedom. It should be noted that the RC frame structure takes half of these degrees of freedom. It is the minimum number of nodes (and degrees of freedom) that allows a reasonable three-dimensional geometrical representation and modelling of cracking of concrete. It is obvious that for more accurate results, a finer mesh should be employed, especially regarding the structure response. However, any reduction in element size would dramatically increase the computation time. Namely, the critical time step decreases proportionally to the reduction while the number of elements increases by the third power. Alternatively, instead of three-dimensional solid elements, for the frame structure, beam finite elements could be used. However, in such case, information related to strain rate, crack velocity or change of failure mode

due to high loading rate cannot be accounted for. A more in depth discussion of the computational aspects is given in Chapter 6.

The entire dynamic analysis took eight days on a personal computer equipped with a single Intel i7 processor running the code in serial (480.000 increments for 3.0 s of actual time). From the computational point of view, the most expensive procedure is by far the stress calculation in the concrete elements (integration is performed over 21 microplanes in each of the eight gauss points of each hexahedral element). This high computational cost is justified by a very accurate representation of concrete and allows a three-dimensional damage and fracture analysis within the smeared crack approach. The accuracy of the results is affected to a certain degree by a relatively coarse discretisation of the cross sections of the frame elements. But, as discussed above, a finer discretisation comes at a cost of significant increase of computational time.

7.2. Numerical study 2

This study examines the influence of a contact discontinuity between the soil and the structure. A series of numerical analyses were performed by varying the ground motion intensity (by setting the PGA of the selected accelerogram) and for different coefficients of friction μ. To emphasis the contact discontinuity in the presented numerical examples the structure is founded on a flat ground surface. Namely, in this case almost all of the seismic energy will be transferred through the contact discontinuity by friction forces. A minor part of the energy will be transferred by normal forces, i.e. by ground elevation. The emphasis is on the physics of the soil – foundation system in the perspective of two important interconnected non-linear mechanisms: (1) foundation sliding and/or detachment from the soil with subsequent uplifting and (2) formation and accumulation of plastic deformations in the ground below the footing. The interaction of these mechanisms can eventually lead to collapse by dynamic instability (overturning) or collapse by soil failure.

In order to simulate the energy transfer mechanism through the contact discontinuity and to account for the frictional energy dissipation on the same interface, contact between different FE discretisations (bodies) has to be considered. The procedure is based on satisfying the Karush-Kuhn-Tucker conditions of optimality (Wriggers, 2002). Accordingly, in each time increment Δt the contact analysis requires two different tasks to be solved. (1) Since the contact event is evident in mesh boundary interactions and, on the other hand, the introduced equation of motion (2.26.) cannot recognize contact events, an exterior computational procedure is needed to monitor the deformation path and to notify if contact between meshes (bodies) occurs. (2) By identifying and localizing mesh contact regions, the description of forces over the contact interfaces should be given according to the principles of contact mechanics (Wriggers, 2002). These two procedures can be classified as contact detection and contact resolution stage. The stages are principally different and are discussed in detail in Chapter 5.

The structure analysed in the present study is a concrete column on a square footing 1.60 x 1.60 x 0.50 m. The cross section of the column is 0.36 x 0.36 m and the height of the column is 2.88 m. An additional block is placed on the top of the column with the dimensions 0.96 x 0.96 x 0.42 m The mass of the block is increased to account for an extra live load of 37.15 kN. The total mass of the structure is then equal to 9010 kg. Assuming linear elastic behaviour and the fix end boundary the first 3 eigenvalues of the column are 0.276 s (x direction), 0.276 s (y direction) and 0.099 s (torsion). The mechanical properties of the concrete are: modulus of elasticity $E_c = 30$ GPa, Poisson's ratio $\mu = 0.18$ and mass density $\rho_c = 2400$ kg/m^3.

The dimensions of the portion of the ground taken into account are 10 x 10 m in plan and 5 m in depth, which is more than enough for the so called pressure bulb to form. Ground type used in the present study is a soft rock mass. The generalized Hoek-Brown strength parameters and rock mass parameters were determined using RocLab (Rocscience, 2002) with the following input data: unconfined compressive strength of intact rock $sigci = 50$ MPa, intact rock parameter mi = 14, disturbance factor $D = 0$ and modulus ratio value MR =400. Rock mass deformation modulus E_{rm} has the value of 0.610 GPa and is calculated according to the generalized Hoek-Diederichs equation (Hoek and Diederichs, 2006) with the geological strength index (GSI) equal to 10 (laminated, sheared structure with poor surface condition). The uniaxial compressive f_c and tensile strength f_t are 0.143 and 0.004 MPa, respectively. The described ground type, according to shear wave velocity alone (312.7 m/s), would be commonly classified to type C ($180 < v_{s,30} < 360$ m/s).

The discretisation of the ground and the foundation is performed with linear tetrahedrons and the rest of the structure with linear hexahedrons. The total number of elements is 14747 and total number of nodes is 7613. The bottom surface of the footing is discretised with 49 nodes (7x7). These nodes are potential contractor nodes, which with the respective target surfaces make contact elements. The FE discretisation is shown in Figure 7.10.a.

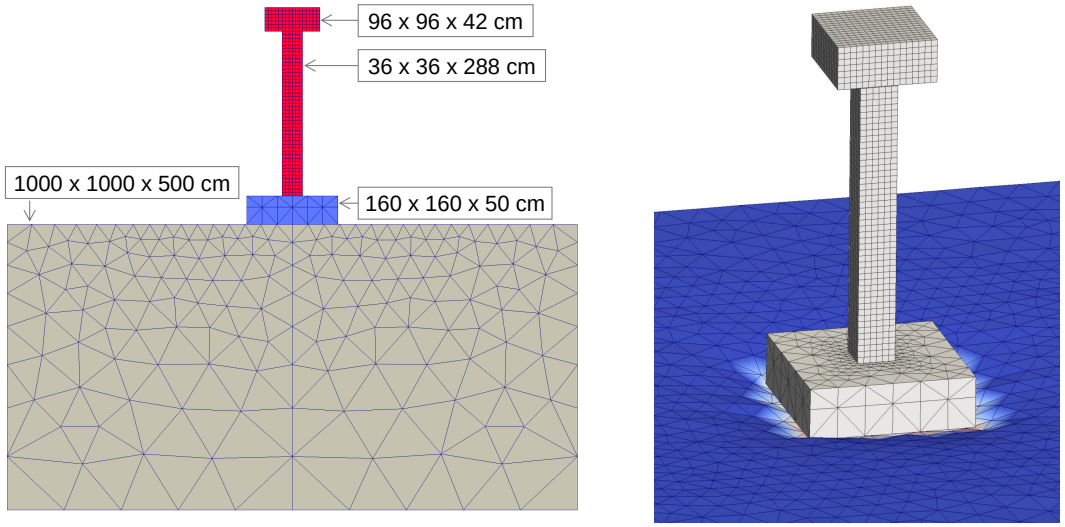

(a) Geometry of the structure. **(b)** Model in the initial state.

Figure 7.10.: 3D FE model of the structure in the second study

The earthquake record used in the present study is taken from the Japanese digital strong-motion seismograph network - Kik-net NIED (2013). The numerical analysis is performed for a 4.00 seconds representative fragment of the original record scaled to PGA of 0.1g

(PGV = 0.05405 m/s, and PGD = 0.00683 m), see Figure 7.3.. The selected fragment has a mean period of 0.24 seconds and produces an acceleration response spectrum (Figure 7.3.c) with a relative narrow band in the high frequency range (appropriate for the structure in question with the fundamental period of 0.276 s). The described accelerogram is applied on all the nodes of the ground elements in the x direction.

Prior to the dynamic analysis, a static analysis is performed in order to realize contact forces between the ground and the structure and to achieve a state of initial deformations. For this purpose, Dirichlet conditions of zero displacements are imposed at the bottom surface in the vertical direction and at the lateral surface in the horizontal direction.

A series of numerical analyses are performed varying the peak ground acceleration PGA (0.1g, 0.2g and 0.3g) and friction coefficients μ (0.10, 0.25, 0.40 and 0.55). Friction coefficients between the concrete surface and surface of various ground types have a large range of values. Additionally, many factors can change their typical values. For example, wet conditions and thermal insulation below the foundation can significantly reduce friction. Furthermore, there are special constructions details, such as the friction pendulum system (FPS), that allow for a controlled sliding of the foundations by intentionally reducing friction. The emphasis here is not on the exact values of friction coefficients, but rather to investigate their influence on the SSI with contact discontinuity and consequently on the structure response.

Table 7.3. shows maximum total displacements (d_{tot}) of the top of the column, maximum relative displacements (d_{rel}) and relative velocities (v_{rel}) and maximum total base shear force (B.S.) for various of PGA and μ. The total B.S. force is equal to the horizontal component of the contact forces at a certain time which is, as mentioned before, limited in magnitude by the respective vertical component. The energy of the ground motion is transmitted to the structure through friction. When the maximal allowable friction force is reached, sliding between the ground and the foundation occurs. For the motion of the lowest intensity studied (0.1g), the value of the friction coefficient $\mu = 0.25$ is sufficient to prevent sliding. For lower values of μ, sliding occurs and energy dissipates through friction and for larger values of μ the response remains virtually unchanged. With increasing the intensity of the motion to PGA of 0.2g and then 0.3g, the threshold value of μ raises to 0.40 and 0.55, respectively. The mentioned thresholds are a consequence of the weight of the structure and the investigated structure is fairly light. Increasing the weight of the structure would increase the maximal allowable friction force and consequently the friction thresholds.

An illustration of sliding (for the case of PGA = 0.2g and μ =0.1) is shown in Figure 7.11.a and 7.11.b. Figure 7.11.a shows the relative movement of the footing to the ground and Figure 7.11.b the respective horizontal contact force. When the horizontal contact

Table 7.3.: Maximum total displacement d_{tot} of the top of the column, relative displacements d_{rel} and relative velocities v_{rel} and maximal total base shear force B.S. for various of values of PGA and μ.

PGA (g)	μ	d_{tot} (cm)	d_{rel} (cm)	v_{rel} (cm/s)	B.S. (kN)
0.1	0.10	1.36	0.39	9.06	8.81
	0.25	1.36	0.58	14.81	17.34
0.2	0.10	2.13	0.50	12.49	8.94
	0.25	2.75	0.98	23.43	35.77
	0.40	2.76	1.12	26.47	31.83
0.3	0.10	0.58	0.18	4.69	8.77
	0.25	2.51	1.71	14.66	66.00
	0.40	2.65	1.04	9.61	36.64
	0.55	2.69	1.70	12.38	56.67

force reaches the maximal allowable value, represented by a dashed horizontal line, starts the sliding between the structure and the ground. In the pictured case, this threshold was reached 4 times. After 4 s the ground motion stops and the structure continues to oscillate freely but with a residual displacement of the entire structure.

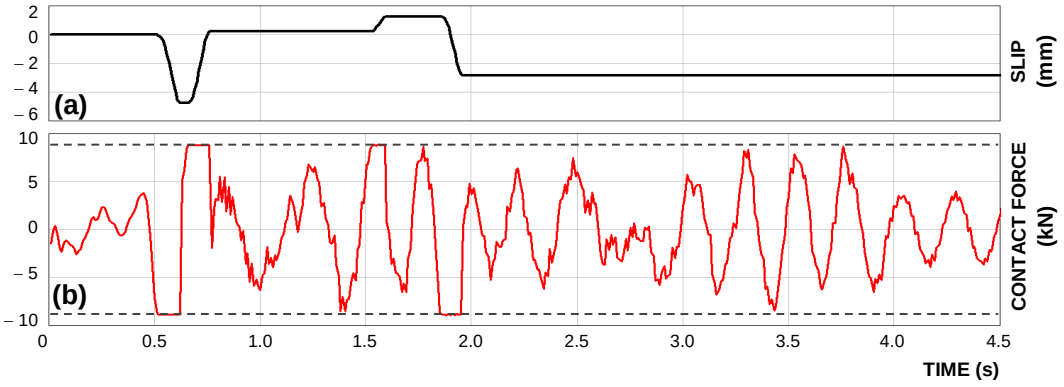

Figure 7.11.: (a) horizontal slip between the foundation and the soil and (b) horizontal contact force, both for PGA of 0,2g and μ of 0,1.

As expected, increasing the coefficient of friction for a given level of ground motion, more energy is transmitted to the structure, and less is dissipated through sliding, thus increasing the relative displacements, relative velocities and the total B.S. force (see Table 7.3.). Figure 7.12. shows the relative displacements of the structure for $\mu = 0.10$ (black line), $\mu = 0.25$ (blue line) and $\mu = 0.25$ (red line) for the case of PGA = 0.2g. Energy transformations in the structure for $\mu = 0.10$ are shown in Figure 7.12.a. It can be noted that the kinetic energy is the most present form and reaches its maximum values while the sliding occurs (translator movement of the entire structure). At the same time the variation of the potential energy is negligible. Increasing the friction coefficient even more (to $\mu = 0.40$) the foundation undergoes partial uplifting from the ground and

rocking becomes the main form of oscillations. Figure 7.13.b clearly shows the rocking phenomena in the form of energy transformation and in particular potential energy.

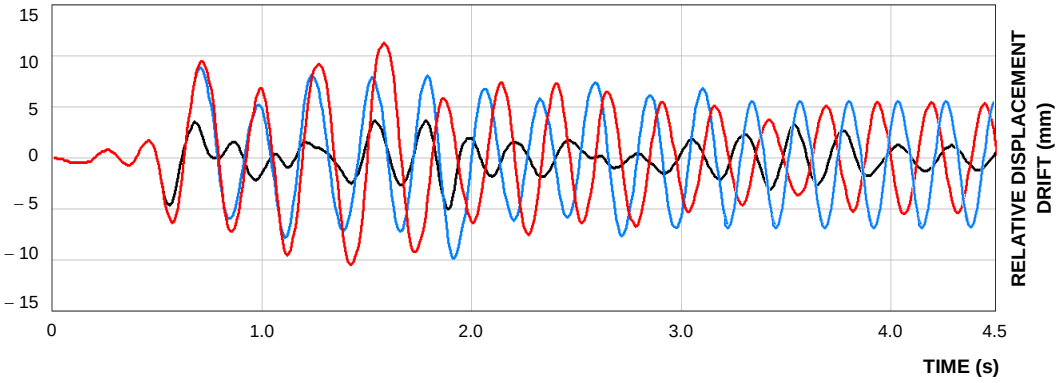

Figure 7.12.: Relative displacements for PGA of 0.2g and $\mu = 0.10$ (black), $\mu = 0.25$ (blue) and $\mu = 0.40$ (red).

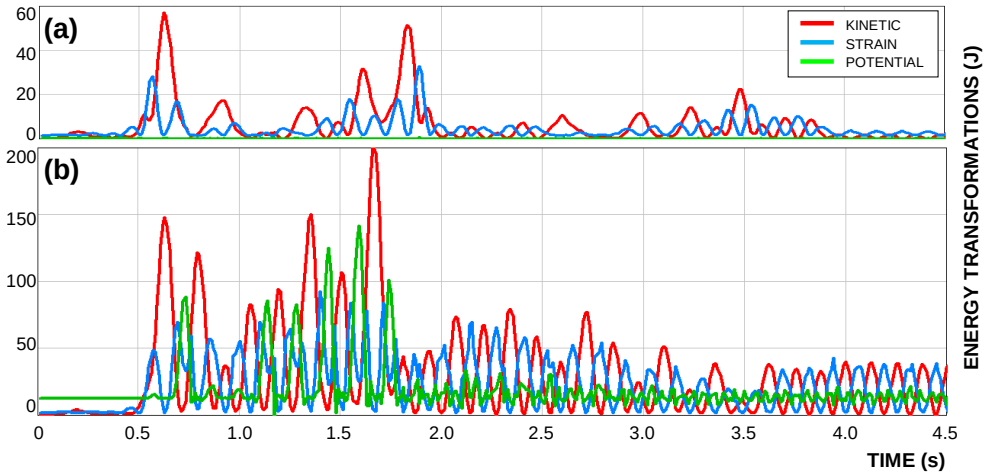

Figure 7.13.: Structure energy transformations for PGA = 0.2g and $\mu = 0.1$ (a) and $\mu = 0.4$ (b).

For higher intensity of ground motions rocking becomes very important. While one side of the footing detaches from the ground (foundation uplifting), the other side of the footing exhibits concentrated compressive loads on the ground (see Figure 7.14.). If the bearing capacity of the soil is reached the rocking is damped which may lead to collapse due to soil failure. Otherwise, the rocking can persist which may lead to collapse by dynamic instability (overturning). In both cases the non-linear behaviour of the ground is important. Note that even treating the soil as perfectly elastic, once that uplift occurs, the problem becomes geometrically non-linear. Allowing plastic deformations of soil below the footing the soil start to act as a cushion reducing the impact during the rocking. To simulate a complete overturning of the structure, the potential contractor

nodes list should include all the nodes on the boundary of the structure. That would, of course, dramatically increase the computational time.

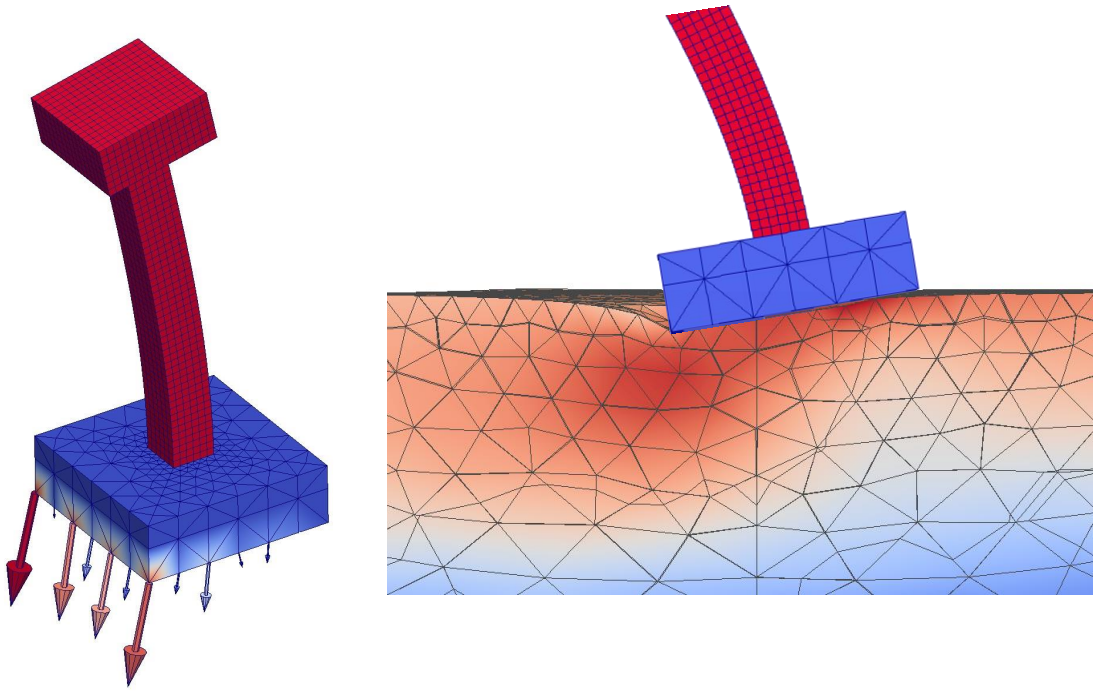

(a) Structure with resultant contact forces on the foundation.

(b) Cross section of the ground with the structure at the same moment.

Figure 7.14.: Snapshots from the FE analysis in the moment of uplifting.

As demonstrated, treating the soil structure interface as a continuum can lead to realistic results only for special cases (combinations of certain ground motion intensities with certain values of μ). To correctly account for the sliding and rocking phenomena the soil structure interface should be treated as a strong discontinuity. In both of this cases (sliding and rocking) the natural frequency period of the system increases. This is important since the typical ground motion carries virtually no energy at large periods of oscillations. The overall effect can be beneficial or detrimental. This depends on many parameters which show the highly non-linear nature of the contact phenomena.

As mentioned before, the emphasis of the present numerical investigation is on the modelling of soil structure interaction with the application of full contact and geometric non-linearities. In this sense, two parameters are studied in some detail regarding the structural response: the friction coefficient between the two bodies and the intensity of the ground motion. There are many other parameters which have an influence on the structure response but the analysis of their significance is out the scope of this study. They interact in a complex manner with varied importance in different cases. Some of these parameters are the following: characteristics of the ground motion (frequency

content and duration), characteristics of the structure (dynamic properties, slenderness, size and shape of the foundations), characteristics of the soil (stiffness and strength) and other.

Chapter 8.

Summary and conclusions

Summary

In the present thesis, a three-dimensional finite element model for non-linear dynamic analysis of seismic site and structure response was proposed and discussed. The aim of this thesis was to investigate the objectivity of the current principles used in the design of structures for earthquake resistance and formulations of guidelines for their improvement with the purpose of constructing more reliable and economic structures. There was also an intention to demonstrate the possibility of advanced numerical approaches in simulation of complex engineering problems such as soil-structure interaction in case of earthquake loading. Although, such an approach cannot be employed in standard structural design, it can be effectively used in design of structures of common interest, such as bridges, nuclear power plants and similar kind of structures. The primary objective of this thesis was the development and application of an original computer program code (written in Fortran language) which was used in the two presented numerical studies.

First numerical study includes modelling of a reinforced concrete frame with a large portion of the ground consisting of various horizontal layers resting on rigid bedrock. The investigated examples encompass geometry and phenomena in the range of several orders of magnitude: starting from the ground (hundreds of meters), RC structure (m), steel reinforcement (cm) and, finally, cracking of concrete (mm). Therefore, considering the inevitable large-size models and all the incorporated non-linearities, a problem of computational efficiency merges naturally. The influence of soil layers configurations on the ground and structure response due to earthquake was investigated.

Second numerical study focuses on the soil - structure interface which was treated as a strong discontinuity. Based on a structure with relatively simple geometry a parametric

study was carried out by varying the intensity of the ground motion and the coefficient of friction. Two important interconnected non-linear mechanisms were studied - foundation sliding and/or uplifting and formation and accumulation of plastic deformations in the ground below the footing.

The numerical formulation of the problems lies in the framework of continuum mechanics and irreversible thermodynamics. Finite element method was used to perform the discretisation of the governing differential equations in space and the finite difference method was used for the discretisation of time. Total Lagrange formulation of finite strain was adopted to account for large deformations and rotations. Cracking and damage of concrete were accounted for by applying the microplane model within the smeared cracks concept. The reinforcement and the foundation rock masses were modelled according to theory of plasticity adopting the Von Mises and Drucker-Prager yield criteria. The interface between the foundation and the soil was regarded as a strong discontinuity and modelled on the principles of contact mechanics.

Conclusions

Based on the numerical results obtained in the analyses, the following can be concluded.

First numerical study

The presented model is able to reproduce seismic wave propagation through the ground and assess its impact on a RC structure. The developed model does not need to assume the surface ground motion. Instead, the surface ground motion is a result of the motion of the bedrock influenced by the different ground layers above the bedrock and the structure itself. Comparing the response acceleration spectra for different ground configurations, it can be seen that stiffer sites amplify high frequencies more than the softer sites. Similarly, the softer sites amplify mid-range frequencies more than stiffer sites. The quality of the top ground layer has a crucial role in the surface ground motions. Resulting PGA and PGA/PGV ratio increase as ground becomes softer. Significant difference in the structural response obtained from the linear analysis with initial stiffness and full non-linear analysis is observed. The structural stiffness degradation in non-linear analysis leads to lower natural frequencies of the structure and thus affects its response. For a given accelerogram, even a small difference in the fundamental period of oscillation can have a major effect on the structural response. Non-linear soil behaviour becomes important for ground motions of higher intensity and, generally, it can be expected that non-linear modelling would decrease the demand on structure. Whether the neglect of this effects is conservative or non-conservative depends on the specific problem at hand and must be evaluated on a case by case basis. For a typical site, parameters based on

site-specific analyses are likely to be more accurate than code-based parameters and they are also likely to result in more economical design. Finally, the implemented microplane model for concrete and explicitly modelling of reinforcement allow for a detailed damage analysis. Such advanced and detailed models can give an edge in assessing seismic performance, but still not without a high computational cost.

Second numerical study

In the presented case study almost all of the induced seismic energy is transferred to the structure through the contact discontinuity by friction forces. When the maximum allowable frictional force is reached, sliding between the ground and the foundation occurs, which becomes the principal source of energy dissipation that in turn reduces the demand on the structure. For every level of ground motion there is a threshold value of the coefficient of friction below which sliding occurs, which makes the continuum assumption inappropriate. On the other extreme, for high ground motion intensities and with large enough values of μ usual forms of structure oscillations are replaced by rocking. In both cases the non-linear behaviour of the supporting ground is important. The interplay of these mechanisms can possibly lead to the collapse by dynamic instability (overturning) or collapse by soil failure. For extreme scenarios with highly geometrically non-linear behaviour, as sliding and rocking, the proposed model is more adequate than usual spring-dashpot elements with continuum assumptions with a reasonable computational efficiency. Being able to capture these phenomena, the presented model could be of interest for special structures like tall columns, monuments, elevated water and control towers and for special construction details relaying on very low friction coefficients like the friction pendulum system.

Future work

Future work will go in two basic directions. Firstly, the inevitable issue of computational efficiency will be approached by an attempt to parallelise the most expensive routines. That should lead to finer discretisations, but without the increase of computational time. Also, a more efficient code should be able to process more complex structures, especially when including contact discontinuity in modelling SSI as in the second numerical study. Secondly, new constitutive laws will be added into the code for modelling different types of foundation soils with the possibility to include materials with high initial anisotropy.

Appendix A

Kik-Net time-history record

The earthquake record used in the present study is taken from the Japanese digital strong-motion seismograph network Kik-net (NIED, 2013) which consists of pairs of seismographs installed in borehole together with seismographs on the ground surface. The accelerogram shown in Figure 7.3. was recorded at the Gozenyama site on 11 March 2011 on a borehole seismograph installed on bedrock at an altitude of -62 m. Since the used accelerogram does not represent outcrop motions, but rather in-depth motions, the deconvolution analysis is not really necessary. The numerical analysis is performed for a 2.25 s fragment of the original record scaled to peak ground acceleration (PGA) of 0.1 g with peak ground velocity (PGV) equal to 0.05405 m/s and peak ground displacement (PGD) equal to 0.00683 m. The selected fragment has a mean period of 0.24 s and produces an acceleration response spectrum with a relative narrow band in the high frequency range.

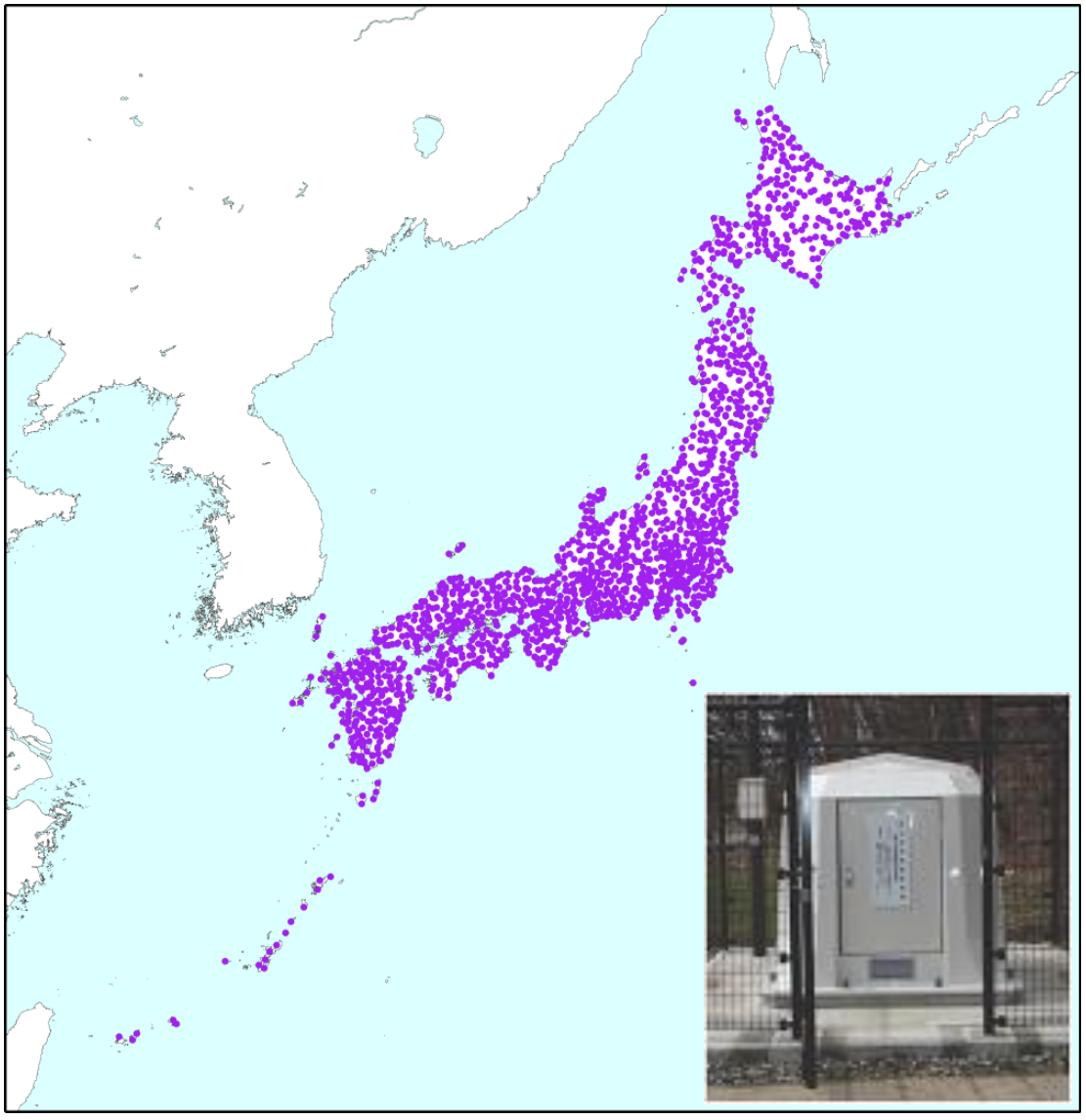

Figure A1.: The Japanese digital strong-motion seismograph network Kik-net.

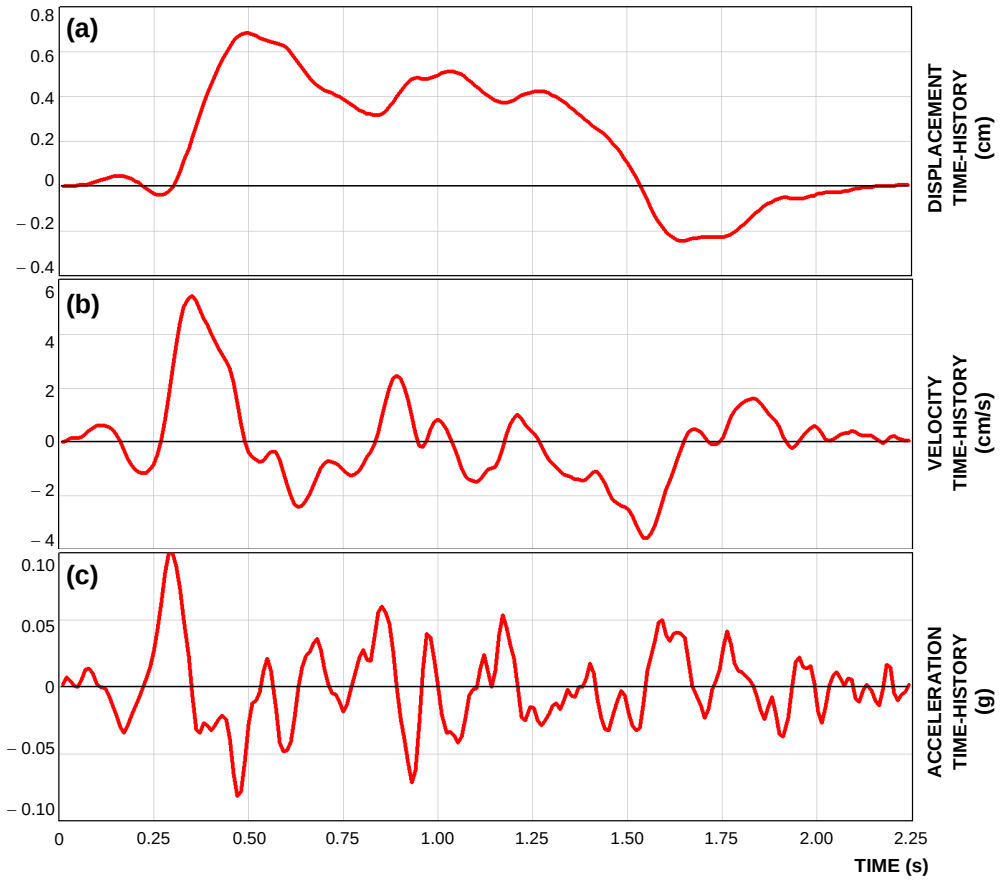

Figure A2.: Displacement, velocity and acceleration time-history of the used record.

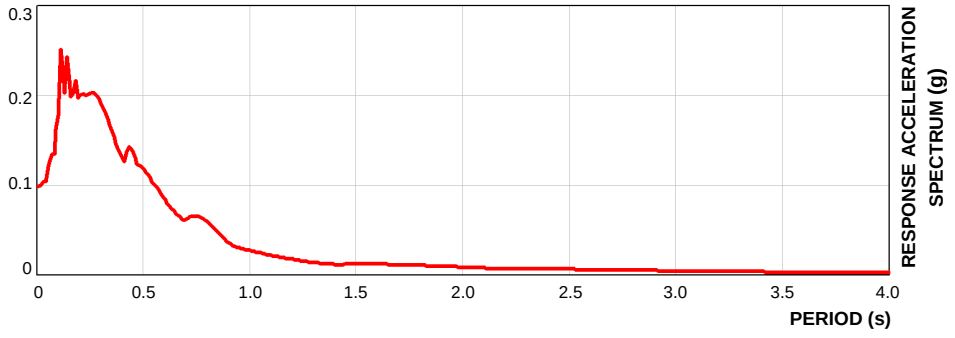

Figure A3.: Acceleration response spectrum of the used record.

Appendix B

Supplementary material - numerical study 1

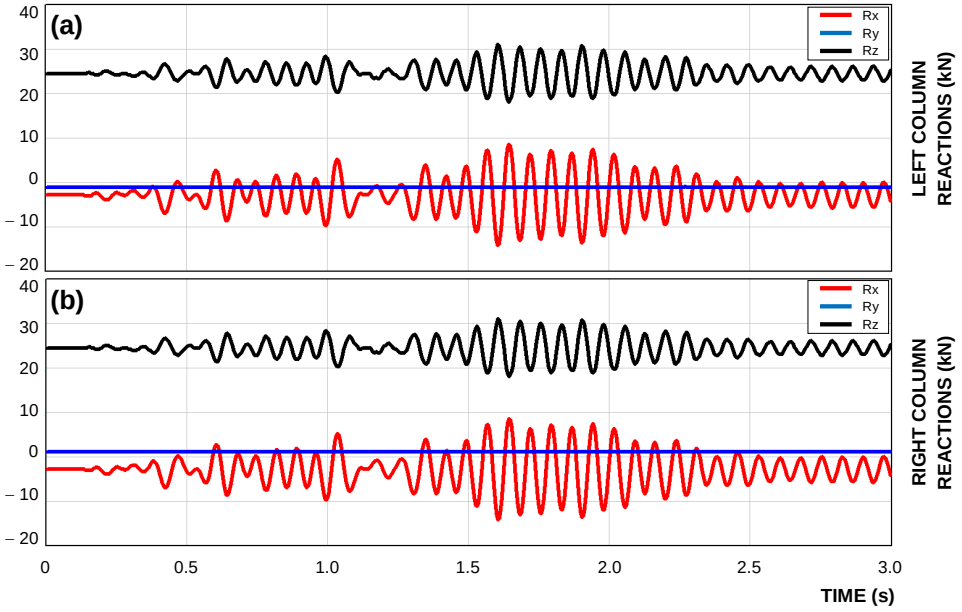

Figure B1.: Reactions of the RC frame columns.

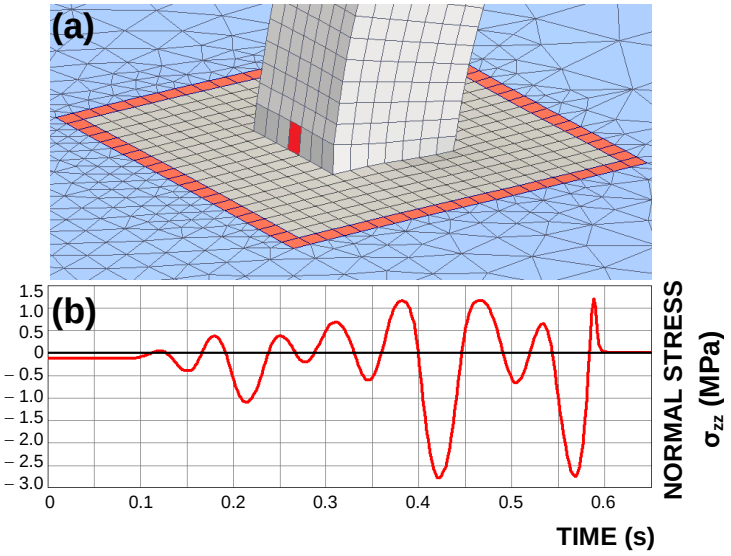

Figure B2.: Normal stress time history for a single element in the base of the column.

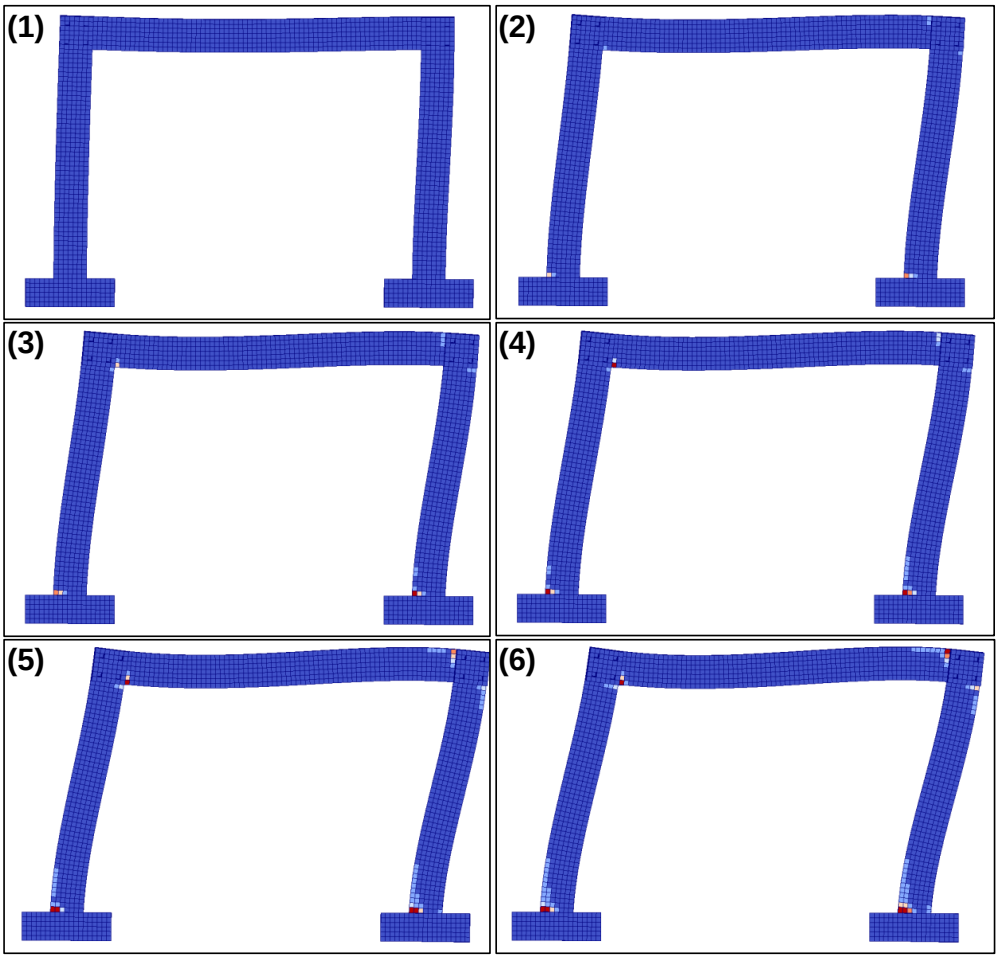

Figure B3.: Crack progression in RC frame members.

Bibliography

Anderheggen, E., Ekchian, D., Heiduschke, K., and Bartelt, P. (1993). A contact algorithm for explicit dynamic fem analysis. In Brebbia, C. and Aliabadi, M., editors, *WIT Transactions on Engineering Sciences vol. 1.*

Aoi, S., Kunugi, T., and Fujiwara, H. (2004). Strong-motion seismograph network operated by nied: K-net and kik-net. *Journal of Japan Association for Earthquake Engineering*, 4(3).

Apostolou, M., Gazetas, G., and Garini, E. (2007). Seismic response of slender rigid structures with foundation uplifting. *Soil Dynamics and Earthquake Engineering*, 27(7):642 – 654.

Bažant, P. and Oh, B. H. (1986). Efficient numerical integration on the surface of a sphere. *ZAMM - Journal of Applied Mathematics and Mechanics / Zeitschrift für Angewandte Mathematik und Mechanik*, 66(1):37–49.

Bažant, Z., Adley, M., Carol, I., Jirásek, M., Akers, S., Rohani, B., Cargile, J., and Caner, F. (2000). Large-strain generalization of microplane model for concrete and application. *Journal of Engineering Mechanics*, 126(9):971–980.

Bažant, Z. and Ožbolt, J. (1990). Nonlocal microplane model for fracture, damage, and size effect in structures. *Journal of Engineering Mechanics*, 116(119):2485–2505.

Bažant, Z. and Prat, P. (1988). Microplane model for brittle-plastic material: I. theory. *Journal of Engineering Mechanics*, 114(10):1672–1688.

Bažant, Z. P. and Oh, B. (1983). Crack band theory for fracture of concrete. *Matériaux et Construction*, 16(3):155–177.

Bathe, K. J. (1996). *Finite elements procedures.* Prentice Hall, New Jersey.

Bazant, Z. P., Caner, F. C., Carol, I., Adley, M. D., and Akers, S. A. (2000). Microplane model m4 for concrete. i: Formulation with work-conjugate deviatoric stress. *Journal of Engineering Mechanics*, 126(9):944–953.

Bazant, Z. P. and Gambarova, P. G. (1984). Crack shear in concrete: Crack band microplane model. *Journal of Structural Engineering*, 110(9):2015–2035.

Bazant, Z. P., Xiang, Y., Adley, M. D., Prat, P. C., and Akers, S. A. (1996a). Microplane model for concrete: Ii: data delocalization and verification. *Journal of Engineering Mechanics*, 122(3):255–262.

Bazant, Z. P., Xiang, Y., and Prat, P. C. (1996b). Microplane model for concrete. i: stress-strain boundaries and finite strain. *Journal of Engineering Mechanics*, 122(3):245–254.

Belytschko, T., Liu, W. K., Moran, B., and Elkhodary, K. (2013). *Nonlinear Finite Elements for Continua and Structures, 2nd Edition*. Wiley.

Bonet, J. and Wood, R. D. (2008). *Nonlinear Continuum Mechanics for Finite Element Analysis*. Cambridge University Press, 2 edition.

Caner, F. C. and Bazant, Z. P. (2000). Microplane model m4 for concrete. ii: Algorithm and calibration. *Journal of Engineering Mechanics*, 126(9):954–961.

Carol, I. and Bazant, Z. P. (1997). Damage and plasticity in microplane theory. *International Journal of Solids and Structures*, 34(29):3807–3835.

Carpenter, N. J., Taylor, R. L., and Katona, M. G. (1991). Lagrange constraints for transient finite element surface contact. *International Journal for Numerical Methods in Engineering*, 32(1):103–128.

Caušević, M. and Mitrović, S. (2011). Comparison between non-linear dynamic and static seismic analysis of structures according to european and us provisions. *Bulletin of Earthquake Engineering*, 9(2):467–489.

Courant, R., Friedrichs, K., and Lewy, H. (1967). On the partial difference equations of mathematical physics. *IBM J. Res. Dev.*, 11(2):215–234.

Crisfield, M. (1991). *Non-linear finite element analysis of solids and structures. Volume 1. , Essentials*. Wiley, Chichester, New York.

Crisfield, M. A. (1997). *Non-Linear Finite Element Analysis of Solids and Structures: Advanced Topics*. John Wiley & Sons, Inc., New York, NY, USA, 1st edition.

Dolšek, M., Klinc, R., Dolenc, M., Brozovič, M., and Peruš, I. (2009). A toolbox and web application for the seismic performance assessment of buildings. In Schanz, T. and Iankov, R., editors, *Coupled Site and Soil-Structure Interaction Effects with Application to Seismic Risk Mitigation*, NATO Science for Peace and Security Series C: Environmental Security, pages 233–257. Springer Netherlands.

Dowell, M. and Jarratt, P. (1972). The "pegasus" method for computing the root of an equation. *BIT Numerical Mathematics*, 12(4):503–508.

Eurocode 8 (2011). *Design of structures for earthquake resistance, EN 1998-1*. European committee for standardization (CEN), Brussels, Belgium.

Fajfar, P. (2000). A nonlinear analysis method for performance based seismic design. *Earthquake Spectra*, 16(3):573–592.

Fajfar, P. and Gašperšič, P. (1996). The n2 method for the seismic damage analysis of rc buildings. *Earthquake Engineering and Structural Dynamics*, 25(1):31–46.

FEMA-273 (1997). *NEHRP guidelines for seismic rehabilitation of buildings*. Federal Emergency Managment Agency, Washington, DC.

FEMA-356 (2000). *Pre-standard and Commentary for the Seismic Rehabilitation of Buildings*. Federal Emergency Managment Agency, Washington, DC.

FEMA-440 (2005). *Improvement of Nonlinear Static Sismic Analysis Procedures*. Federal Emergency Managment Agency, Washington, DC.

Gajan, S. and Kutter, B. L. (2009). Contact interface model for shallow foundations subjected to combined cyclic loading. *Journal of Geotechnical and Geoenvironmental Engineering*, 135(2):407–419.

Gazetas, G., Anastasopoulos, I., and Apostolou, M. (2007). Shallow and deep foundations under fault rupture or strong seismic shaking. In Pitilakis, K., editor, *Earthquake Geotechnical Engineering*, volume 6 of *Geotechnical, Geological and Earthquake Engineering*, pages 185–215. Springer Netherlands.

Gazetas, G. and Mylonakis, G. (1998). Seismic soil-structure interaction: New evidence and emerging issued. In Dakoulas, P., Yegian, M., and Holtz, R., editors, *Proceedings of a Speciality Conference: Geotechnical Earthquake Engineering and Soil Dynamics III, Geotechnical Special Publications No. 75*.

Gerolymos, N. and Gazetas, G. (2006). Development of winkler model for static and dynamic response of caisson foundations with soil and interface nonlinearities. *Soil Dynamics and Earthquake Engineering*, 26(5):363 – 376.

Harden, C. W. and Hutchinson, T. (2009). Beam-on-nonlinear-winkler-foundation modeling of shallow, rocking-dominated footings. *Earthquake Spectra*, 25(2):277–300.

Harden, C. W., Hutchinson, T., and Moore, M. (2006). Investigation into the effects of foundation uplift on simplified seismic design procedures. *Earthquake Spectra*, 22(3):663–692.

Harden, C. W., Hutchinson, T. C., Kutter, B. L., and Martin, G. (2005). Numerical modelling of the nonlinear cyclic response of shallow foundation.

Harewood, F. and McHugh, P. (2007). Comparison of the implicit and explicit finite element methods using crystal plasticity. *Computational Materials Science*, 39(2):481 – 494.

Hashash, Y. M. and Park, D. (2001). Non-linear one-dimensional seismic ground motion propagation in the mississippi embayment. *Engineering Geology*, 62(1–3):185 – 206. Earthquake hazard evaluation in the Central United States.

Hashash, Y. M. and Park, D. (2002). Viscous damping formulation and high frequency motion propagation in non-linear site response analysis. *Soil Dynamics and Earthquake Engineering*, 22(7):611 – 624.

Heinstein, M., Attaway, S., Swegle, J., and Mello, F. (1993). A general contact detection algorithm for finite element analysis. In BREBBIA, C. and ALIABADI, M., editors, *WIT Transactions on Engineering Sciences vol. 1.*

Héloïse, C., Bard, P.-Y., and Rodriguez-Marek, A. (2012). Site effect assessment using kik-net data: Part 1. a simple correction procedure for surface/downhole spectral ratios. *Bulletin of Earthquake Engineering*, 10(2):421–448.

Hoek, E. and Diederichs, M. (2006). Empirical estimation of rock mass modulus. *International Journal of Rock Mechanics and Mining Sciences*, 43(2):203 – 215.

Houlsby, G. T., Cassidy, M. J., and Einav, I. (2005). A generalised winkler model for the behaviour of shallow foundations. *Geotechnique*, 55(6):449 – 460.

Hutter, M. and Fuhrmann, A. (2007). Optimized continuous collision detection for deformable triangle meshes. *Journal of WSCG*, 15(1-3):25–32.

Jahromi, H. (2009). *Partitioned analysis of nonlinear soil-structure interaction.* dissertation, Imperial College London.

Jeremić, B., Jie, G., Preisig, M., and Tafazzoli, N. (2009). Time domain simulation of soil–foundation–structure interaction in non-uniform soils. *Earthquake Engineering and Structural Dynamics*, 38(5):699–718.

Jeremić, B. and Yang, Z. (2002). Template elastic-plastic computations in geomechanics. *International Journal for Numerical and Analytical Methods in Geomechanics*, 26(14):1407–1427.

Kitware (2012). Paraview: Parallel visualization application.

Kontoe, S., Zdravkovic, L., and Potts, D. M. (2008). An assessment of time integration schemes for dynamic geotechnical problems. *Computers and Geotechnics*, 35(2):253 – 264.

Kramer, S. (2014). *Geotechnical Earthquake Engineering: Pearson New International Edition*. Always learning. Pearson Education, Limited.

Kreslin, M. and Fajfar, P. (2012). The extended n2 method considering higher mode effects in both plan and elevation. *Bulletin of Earthquake Engineering*, 10(2):695–715.

Lehmann, L. (2005). An effective finite element approach for soil-structure analysis in the time-domain. *Structural Engineering and Mechanics*, 21(4):437 – 450.

Ling, W. and Stolarski, H. (1997). On elasto-plastic finite element analysis of some frictional contact problems with large sliding. *Engineering Computations*, 14(5):558–580.

Lopez-Caballero, F., Razavi, Modaressi-Farahmand, A., and Modaressi, H. (2007). Nonlinear numerical method for earthquake site response analysis i — elastoplastic cyclic model and parameter identification strategy. *Bulletin of Earthquake Engineering*, 5(3):303–323.

Lu, L.-Y. and Hsu, C.-C. (2013). Experimental study of variable-frequency rocking bearings for near-fault seismic isolation. *Engineering Structures*, 46(0):116 – 129.

Lysmer, J. and Kuhlemeyer, R. (1969). Finite dynamic model for infinite media. *Journal of the Engineering Mechanics Division*, 95(EM4):859–877.

Mahmoud, S., Austrell, P.-E., and Jankowski, R. (2012). Simulation of the response of base-isolated buildings under earthquake excitations considering soil flexibility. *Earthquake Engineering and Engineering Vibration*, 11(3):359–374.

Mitrović, S. and Čaušević, M. (2009). Nonlinear static seismic analysis of structures. *Građevinar*, 61(6).

Mitrović, S., Ožbolt, J., and Travaš, V. (2014). Three-dimensional finite element formulation for nonlinear dynamic analysis of seismic site and structure response. *European Journal of Environmental and Civil Engineering*.

Montalva, G. A. (2010). *Site Specific Seismic Hazard Analyses*. dissertation, Whasington State University.

NIED (2013). Kiban kyoshin network database. http://www.kik.bosai.go.jp/. Online; accessed 2013.

Ožbolt, J. and Bažant, Z. (1992). Microplane model for cyclic triaxial behavior of concrete. *Journal of Engineering Mechanics*, 118(7):1365–1386.

Ožbolt, J. and Bažant, Z. P. (1996). Numerical smeard fracture analysis: nonlocal microcrack interaction approach. *International Journal for Numerical Methods in Engineering*, 39(4):635–661.

Ožbolt, J., Li, Y., and Kožar, I. (2001). Microplane model for concrete with relaxed kinematic constraint. *International Journal of Solids and Structures*, 38(16):2683 – 2711.

Ožbolt, J., Rah, K., and Meštrović, D. (2006). Influence of loading rate on concrete cone failure. *International Journal of Fracture*, 139(2):239–252.

Ožbolt, J., Sharma, A., and Reinhardt, H.-W. (2011). Dynamic fracture of concrete – compact tension specimen. *International Journal of Solids and Structures*, 48(10):1534 – 1543.

Ožbolt, J., Sharma, A., İrhan, B., and Sola, E. (2014). Tensile behavior of concrete under high loading rates. *International Journal of Impact Engineering*, 69:55–68.

Panagiotidou, A. I., Gazetas, G., and Gerolymos, N. (2012). Pushover and seismic response of foundations on stiff clay: Analysis with p-delta effects. *Earthquake Spectra*, 28(4):1589–1618.

Park, D. and Hashash, Y. (2004). Soil damping formulation in nonlinear time domain site response analysis. *Journal of Earthquake Engineering*, 08(02):249–274.

Pergalani, F., de Franco, R., Compagnoni, M., and Caielli, G. (2006). Evaluation of site effects using numerical and experimental analyses in città di castello (italy). *Soil Dynamics and Earthquake Engineering*, 26(10):941 – 951.

PGI (2010). Pgi visual fortran user's guide.

Phillips, C. and Hashash, Y. M. (2009). Damping formulation for nonlinear 1d site response analyses. *Soil Dynamics and Earthquake Engineering*, 29(7):1143 – 1158.

Provot, X. (1997). Collision and self-collision handling in cloth model dedicated to design garments. In Thalmann, D. and van de Panne, M., editors, *Computer Animation and Simulation '97*, Eurographics, pages 177–189. Springer Vienna.

Rocscience (2002). Roclab vesrion 1.0 - rock mass strength analysis using the generalized hoek-brown failure criterion.

Rozman, M. and Fajfar, P. (2009). Seismic response of a rc frame building designed according to old and modern practices. *Bulletin of Earthquake Engineering*, 7(3):779–799.

Semblat, J., Duval, A. M., and Dangla, P. (2000). Numerical analysis of seismic wave amplification in nice (france) and comparisons with experiments. *Soil Dynamics and Earthquake Engineering*, 19(5):347 – 362.

Sextos, A. G. and Taskari, O. (2009). Single and multi-platform simulation of linear and non-linear bridge-soil systems. In Schanz, T. and Iankov, R., editors, *Coupled Site and Soil-Structure Interaction Effects with Application to Seismic Risk Mitigation*, NATO Science for Peace and Security Series C: Environmental Security, pages 225–239. Springer Netherlands.

Sheng, D., Sloan, S. W., and Yu, H. S. (2000). Aspects of finite element implementation of critical state models. *Computational Mechanics*, 26(2):185–196.

Siemens (2009). Femap user's guide.

Singupalli, S. K. (2008). *Evaluation of non-linear site effects using Kik-Net Japanese database*. dissertation, University of Joseph Fourier, Grenoble.

Sloan, S. W., Abbo, A. J., and Sheng, D. (2001). Refined explicit integration of elastoplastic models with automatic error control. *Engineering Computations*, 18(1/2):121–194.

Smerzini, C., Paolucci, R., and Stupazzini, M. (2011). Comparison of 3d, 2d and 1d numerical approaches to predict long period earthquake ground motion in the gubbio plain, central italy. *Bulletin of Earthquake Engineering*, 9(6):2007–2029.

Spiliopoulos, K. V. and Lykidis, G. C. (2006). An efficient three-dimensional solid finite element dynamic analysis of reinforced concrete structures. *Earthquake Engineering and Structural Dynamics*, 35(2):137–157.

Travaš, V. (2009.). Three-dimensional finite formulation for concrete failure at high-energy impact loadings.

Travaš, V., Ožbolt, J., and Kožar, I. (2009). Failure of plain concrete beam at impact load: 3d finite element analysis. *International Journal of Fracture*, 160(1):31–41.

Weihe, S., Kröplin, B., and De Borst, R. (1998). Classification of smeared crack models based on material and structural properties. *International journal of solids and structures*, 35(12):1289–1308.

Wilson, E. L. (1995). *Three Dimensional Static and Dynamic Analysis of Structures*. Computers and Structures Inc., Berkley, California, USA.

Wriggers, P. (2002). *Computational Contact Mechanics*. John Wiley & Sons Ltd., 2st edition.

Yim, C.-S. and Chopra, A. K. (1984). Earthquake response of structures with partial uplift on winkler foundation. *Earthquake Engineering and Structural Dynamics*, 12(2):263–281.

Zhao, J., Sheng, D., Rouainia, M., and Sloan, S. W. (2005). Explicit stress integration of complex soil models. *International Journal for Numerical and Analytical Methods in Geomechanics*, 29(12):1209–1229.

Zienkiewicz, O. C. and Taylor, R. L. (2000). *Solid mechanics*. Butterworth-Heinemann, 5 edition.

Zienkiewicz, O. C. and Taylor, R. L. (2005). *The Finite Element Method for Solid and Structural Mechanics, Sixth Edition*. Butterworth-Heinemann, 6 edition.